博士学位論文

Theory on inelastic photon and neutron scattering in two-dimensional quasiperiodic Heisenberg antiferromagnets

(2 次元準周期 Heisenberg 反強磁性体における
光子及び中性子の非弾性散乱理論)

井上 天

北海道大学大学院理学院 物性物理学専攻

2023 年 3 月

Contents

Abstract

We calculate magnetic Raman scattering for the antiferromagnetic Heisenberg model on a 5-fold Penrose lattice and an 8-fold Ammann-Beenker lattice. We derive effective magnetic Raman operators in quasiperiodic lattices from second- and fourth-order perturbations and analyze them using spin-wave theory. Quasicrystals have crystallographically forbidden point group symmetry. Based on group theory, we decompose the Raman spectra into irreducible representations to reveal the origin of each irreducible mode spectrum and its polarization dependence. We incorporate magnon-magnon interactions by means of Green's function and configuration-interaction schemes and show that the configuration-interaction scheme has great advantages for the quantitative evaluation of multimagnon fluctuations. We also calculate the dynamic structure factor for the Heisenberg antiferromagnets on the Penrose lattice and reveal the magnetic excitation structure. We define a site-resolved dynamic structure factor and map it to the perpendicular space which is characteristic of quasiperiodic systems to investigate the spatial structure of magnetic excitations in detail.

Chapter 1

Introduction

Since the discovery of quasicrystal [1], quasiperiodic systems have been of much interest. Quasicrystals are characterized by quasiperiodicity, i.e., the coexistence of long-range order without translational symmetry and crystallographically forbidden rotational symmetry [2, 3, 4]. Quasiperiodic systems are expected to exhibit novel physical phenomena that are different from both periodic and amorphous systems, and thermodynamically degenerate and strictly localized confined states in tight-binding models [5, 6, 7], quantum critical phenomena [8], and quasiperiodic superconductivity [9, 10, 11, 12] have been investigated.

A variety of magnetic quasicrystals and their approximants [13, 14, 15, 16, 17, 18, 19] have attracted much attention to explore novel magnetism of geometric origin. From the theoretical point of view, the Penrose and Ammann-Beenker lattices in two dimensions attract much interst. Their Ising [20, 21] and classical three-dimensional spin [22, 23] models were simulated by the Monte Carlo method, whereas their Hubbard models [24, 25] were investigated within a mean-field approximation. Quasiperiodic quantum spin systems are of particular interest, and their Heisenberg model were calculated by linear spin wave [26, 27] and quantum Monte Carlo methods [27, 28, 29]. In the context of inelastic-neutron-scattering experiments, spin-wave findings for the dynamic spin structure factor of the Ammann-Beenker Heisenberg antiferromagnet reveal intriguing excitation features possibly due to the quasiperiodicity [26]; the coexistence of linear soft modes near the magnetic Bragg peaks at low frequencies, self-similar structures at intermediate frequencies, and flat bands at high frequencies.

We may take further interest in inelastic light scatterings in quasiperiodic magnets, which strongly reflect their lattice symmetry and potentially bring brandnew information by virtue of the light polarization degrees of freedom. The standard framework for inelastic photon scattering by magnetic excitation was given by Fleury and Loudon [30] as scattering by pair exchange interaction $\boldsymbol{S}_i \cdot \boldsymbol{S}_j$. Magnetic Raman spectroscopy has been used as a powerful probe to provide information on magnetic excitation in many magnetic materials such as cubic [31], square [32, 33, 34, 35, 36], triangle [37], and kagome [38] lattices. A microscopic description of magnetic Raman scattering was given by Shastry and Shraiman [39, 40]. In this formulation, the Loudon-Fleury mechanism is obtained from second-order perturbation theory. Novel magnetic excitations such as scalar-chirality terms $\boldsymbol{S}_i \cdot (\boldsymbol{S}_j \times \boldsymbol{S}_k)$ and ring-exchange terms $(\boldsymbol{S}_i \cdot \boldsymbol{S}_j)(\boldsymbol{S}_k \cdot \boldsymbol{S}_l)$ [41, 42, 43] are possible from higher-order perturbation beyond the Loudon-Fleury mechanism.

Recent technical progress of manipulating optical lattices [44, 45, 46] also deserves special mention. Two-dimensional quasiperiodic potentials with five- [47] or eight-fold [48, 49] rotational symmetry were theoretically designed in terms of standing-wave lasers and indeed observed via Bragg diffraction [45, 47]. By trapping ultracold bosonic or fermionic atoms

in optically tunable potentials, we can change the on-site interaction and tunneling energy to obtain various effective spin models [50]. There may be an extended-to-localized phase transition [46, 51] of a Bose-Einstein condensate, for instance.

Thus motivated, we study magnetic Raman response of spin-$\frac{1}{2}$ Heisenberg antiferromagnets on the $\mathbf{C}_{5\mathrm{v}}$ Penrose and $\mathbf{C}_{8\mathrm{v}}$ Ammann-Beenker lattices. Furthermore, we calculate the dynamic spin structure factor in the Penrose lattice.

1.1 Quasicrystal

Quasicrystals are defined as the structure having a long-range-order without translational symmetry and a crystallographically-forbidden rotational symmetry [2, 3, 4]. We define the scattering intensity as

$$I(\boldsymbol{q}) = \left| \int \rho(\boldsymbol{r}) e^{i\boldsymbol{q}\cdot\boldsymbol{r}} d\boldsymbol{r} \right|^2 , \tag{1.1}$$

where $\rho(\boldsymbol{r})$ is the density function in real space. In this context, the quasicrystals consist of a set of delta-function peaks whose $I(\boldsymbol{q})$ in reciprocal lattice space has a noncrystallographic rotational symmetry ($N = 5$ or $N \geq 7$ -fold symmetry). As an example, $I(\boldsymbol{q})$ of a square lattice is shown in Fig. 1.1(a), of a Penrose lattice in Fig. 1.1(b), and of an amorphous in Fig. 1.1(c). The minimum number of wavevectors that can span the whole diffraction patterns by their integral linear combinations is called the rank or indexing dimension r [52]. For the physical dimension d, conventional periodic crystals have $r = d$, while quasicrystals have $r > d$.

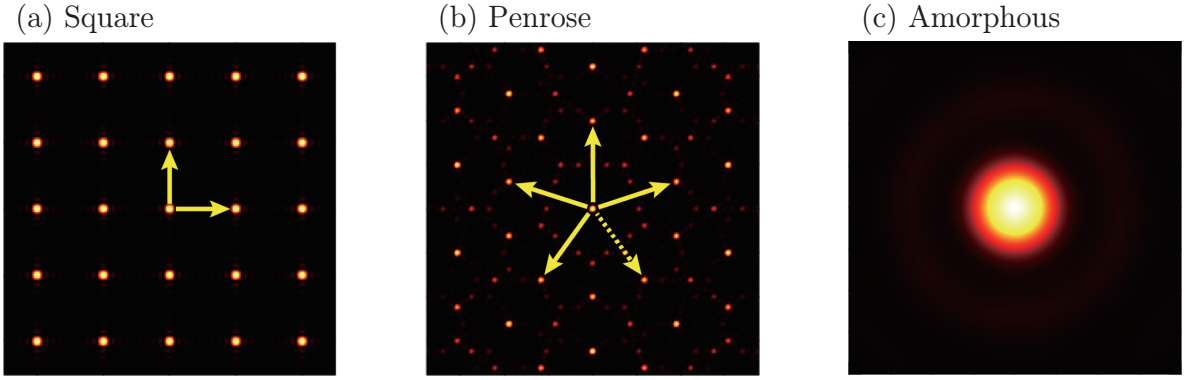

Figure 1.1: Scattering intensity $I(\boldsymbol{q})$ and reciprocal basis vectors in square (a) and Penrose (b) lattices. The vector represented by the dotted line in (b) is a linear combination of the other four vectors. Scattering intensity $I(\boldsymbol{q})$ in amorphous (c) has no reciprocal lattice.

Quasiperiodic lattices are generated by the "cut-and-project" method [53], which projects a higher dimensional periodic crystal to a lower dimension. A d-dimensional quasiperiodic lattice is generated by the cut-and-project method by the following procedure: (i) prepare a $D(> d)$-dimensional periodic lattice, (ii) divide the D-dimensional space into the d-dimensional physical space $\mathrm{E}_{\parallel}$, which has an irrational gradient with respect to the periodic lattice, and the $(D-d)$-dimensional perpendicular space $\mathrm{E}_{\perp}$, which is perpendicular to the physical space, (iii) project the unit cell of the D-dimensional periodic lattice into the perpendicular space $\mathrm{E}_{\perp}$ and set the selection window W, and (iv) project the lattice points contained

in the selection window W into the d-dimensional physical space $\mathrm{E}_{\parallel}$. As the simplest example, Fig. 1.2 shows a schematic illustration of constructing a one-dimensional quasiperiodic Fibonacci lattice from a two-dimensional periodic square lattice. The projection matrix is given by

$$\begin{bmatrix} x \\ \bar{x} \end{bmatrix} = \begin{bmatrix} \cos\theta & \sin\theta \\ -\sin\theta & \cos\theta \end{bmatrix} \begin{bmatrix} m_1 \\ m_2 \end{bmatrix} \quad \left(\tan\theta = \frac{\sqrt{5}-1}{2} \right), \tag{1.2}$$

where m_1 and m_2 are integers representing the lattice points of the two-dimensional square lattice, and x and $\bar{x}$ are the corrdinates of the lattice points in one-dimensional physical and perpendicular space, respectively.

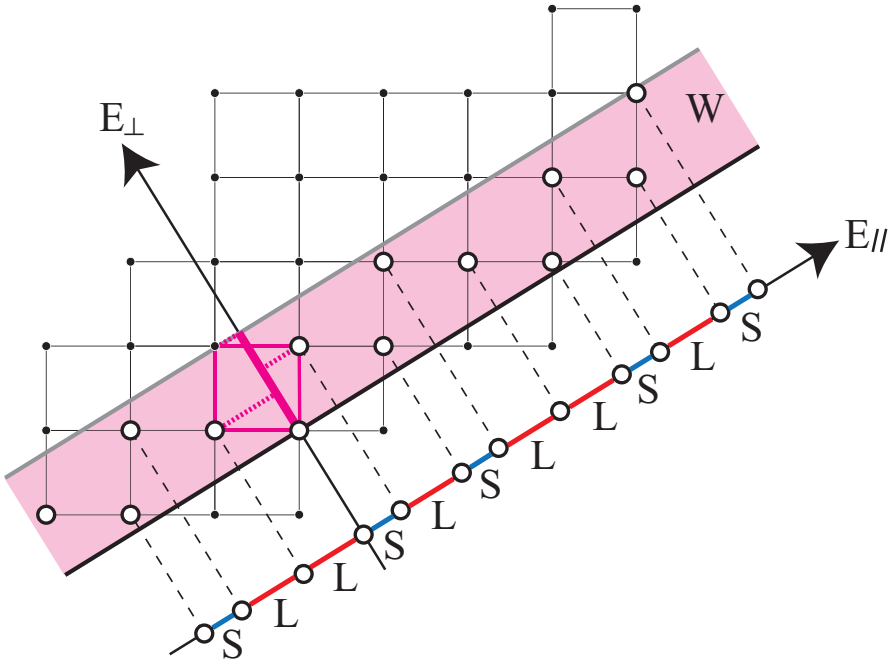

Figure 1.2: Schematic illustration of the cut-and-project method for constructing a one-dimensional quasiperiodic Fibonacci lattice from a two-dimensional periodic square lattice.

The Penrose lattice is obtained by projection from a five-dimensional hypercubic lattice into two-dimensional space. The projection matrix is given by

$$\begin{bmatrix} x \\ y \\ \bar{x} \\ \bar{y} \\ \bar{z}' \end{bmatrix} = \sqrt{\frac{2}{5}} \begin{bmatrix} \cos\theta_0 & \cos\theta_1 & \cos\theta_2 & \cos\theta_3 & \cos\theta_4 \\ \sin\theta_0 & \sin\theta_1 & \sin\theta_2 & \sin\theta_3 & \sin\theta_4 \\ \cos\theta_0 & \cos\theta_2 & \cos\theta_4 & \cos\theta_6 & \cos\theta_8 \\ \sin\theta_0 & \sin\theta_2 & \sin\theta_4 & \sin\theta_6 & \sin\theta_8 \\ \frac{1}{\sqrt{2}} & \frac{1}{\sqrt{2}} & \frac{1}{\sqrt{2}} & \frac{1}{\sqrt{2}} & \frac{1}{\sqrt{2}} \end{bmatrix} \begin{bmatrix} m_1 \\ m_2 \\ m_3 \\ m_4 \\ m_5 \end{bmatrix} \quad \left(\theta_n \equiv \frac{2\pi}{5} n + \frac{\pi}{10} \right), \tag{1.3}$$

where $m_1, \cdots, m_5$ are integers, and x, y and $\bar{x}$, $\bar{y}$, $\bar{z}'$ are coordinates of the two-dimensional physical and three-dimensional perpendicular space, respectively. Note that $\bar{z} \equiv \sqrt{5}\bar{z}'$ can only be an integer. The Ammann-Beenker lattice is obtained by projection from a four-dimensional hypercubic lattice into two-dimensional space. The projection matrix is given

by

$$\begin{bmatrix} x \\ y \\ \bar{x} \\ \bar{y} \end{bmatrix} = \frac{1}{2} \begin{bmatrix} \sqrt{2} & 1 & 0 & -1 \\ 0 & 1 & \sqrt{2} & 1 \\ \sqrt{2} & -1 & 0 & 1 \\ 0 & 1 & -\sqrt{2} & 1 \end{bmatrix} \begin{bmatrix} m_1 \\ m_2 \\ m_3 \\ m_4 \end{bmatrix}, \tag{1.4}$$

where $m_1, \cdots, m_4$ are integers, and x, y and $\bar{x}$, $\bar{y}$ are coordinates of the two-dimensional physical and perpendicular space, respectively.

Figure 1.3 shows an example of the $\mathbf{C}_{5v}$ Penrose and $\mathbf{C}_{8v}$ Ammann-Beenker lattices. Both lattices consist of two types of rhombuses, i.e., a thin (acute angle $\pi/5$) and a thick (acute angle $2\pi/5$) rhombus for the Penrose lattice, and a square and a rhombus (acute angle $\pi/4$) for the Ammann-Beenker lattice, and both lattices are bipartite.

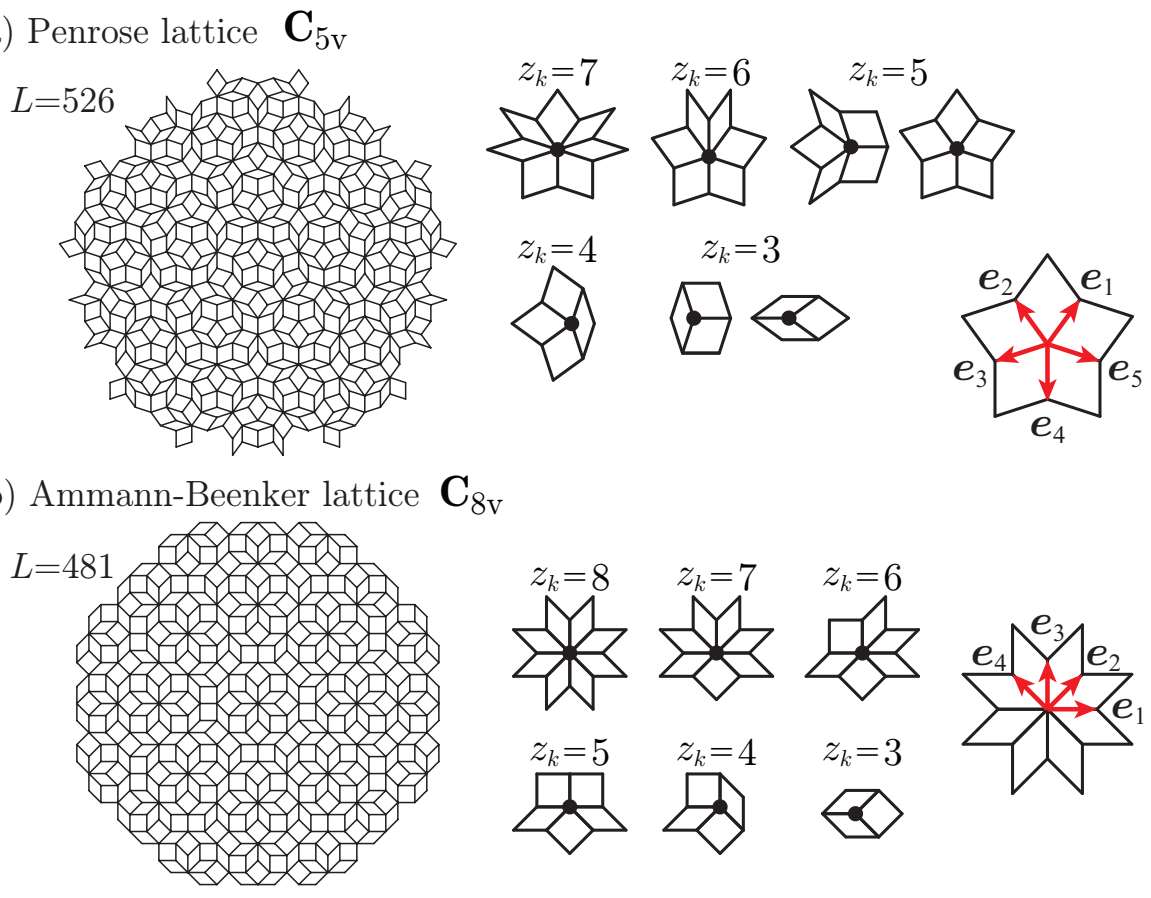

Figure 1.3: (a) Penrose lattice and seven types of local vertices. Primitive lattice vectors $\boldsymbol{e}_1, \cdots, \boldsymbol{e}_5$ are projection of the five-dimensional canonical basis vectors, and they satisfy $\boldsymbol{e}_1 + \boldsymbol{e}_2 + \boldsymbol{e}_3 + \boldsymbol{e}_4 + \boldsymbol{e}_5 = \boldsymbol{0}$. (b) Ammann-Beenker lattice and six types of local vertices. Primitive lattice vectors $\boldsymbol{e}_1, \cdots, \boldsymbol{e}_4$ are projection of the four-dimensional canonical basis vectors.

Figures 1.4 and 1.5 show perpendicular space maps colored by the coordination numbers z_k of the Penrose and Ammann-Beenker lattices, respectively.

Another way to make the quasiperiodic lattice is the self-similar method [7, 54, 55, 56]. As examples, the deflation rule for the Penrose lattice is shown in Fig. 1.6, and for the

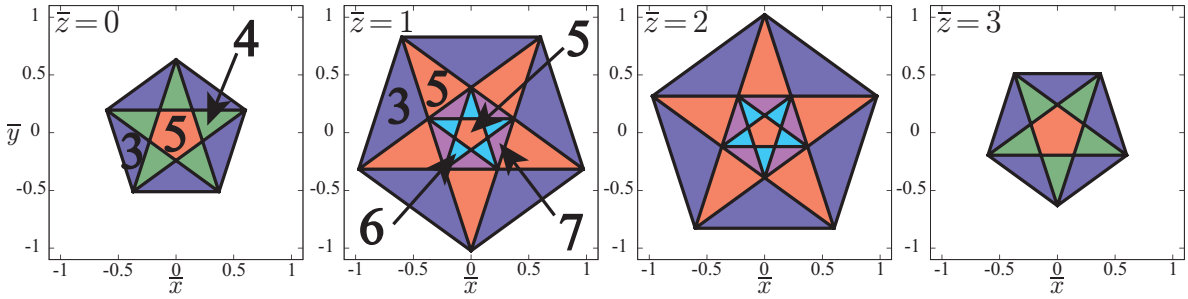

Figure 1.4: Color map in the perpendicular space of the Penrose lattice. The numbers in the figure represent the coordination number of each site. Displaying only the plane in the three-dimensional perpendicular space where the lattice points are projected.

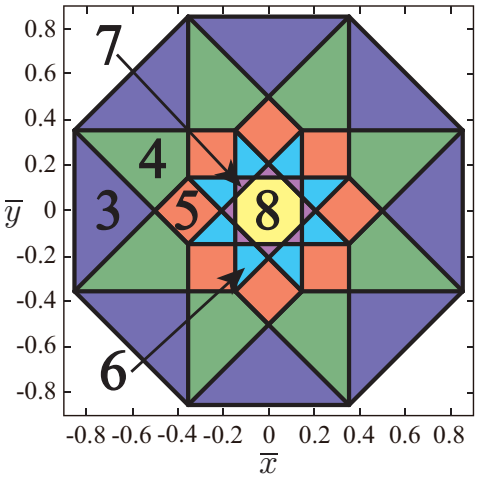

Figure 1.5: Color map in the perpendicular space of the Ammann-Beenker lattice. The numbers in the figure represent the coordination number of each site.

Ammann-Beenker lattice in Fig. 1.7.

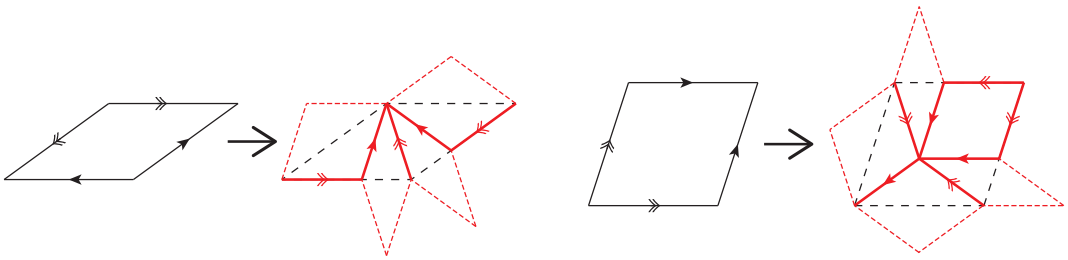

Figure 1.6: Deflation rules for the Penrose lattice. Converting single and double arrowheads to overlap with the same type in order to satisfy the matching rule.

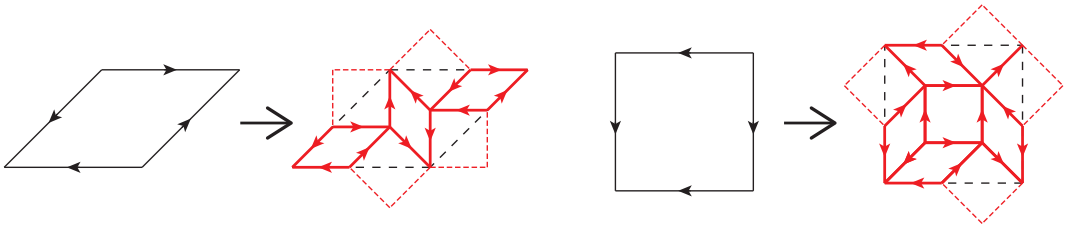

Figure 1.7: Deflation rules for the Ammann-Beenker lattice. Converting arrowheads to overlap in order to satisfy the matching rule.

Chapter 2

Magnetic Raman Operator

Following the Shastry-Shraiman perturbation theory [39, 40, 41], we derive spin-$\frac{1}{2}$ magnetic Raman operators from the half-filled single-band nearest-neighbor Hubbard model

$$\begin{aligned}\mathscr{H} &= U\sum_i c^\dagger_{i\uparrow}c_{i\uparrow}c^\dagger_{i\downarrow}c_{i\downarrow} - t\sum_{\langle i,j\rangle}\sum_{\sigma=\uparrow,\downarrow}(c^\dagger_{i\sigma}c_{j\sigma}+\text{H.c.}),\\ &\equiv \mathscr{H}_U + \mathscr{H}_t,\end{aligned} \tag{2.1}$$

where $c^\dagger_{i\sigma}$ creates an electron with spin σ at site i. We assume that the strongly correlated limit $0 < t \ll U$. We replace all the hopping terms $c^\dagger_{i\sigma}c_{j\sigma}$ in $\mathscr{H}_t$ with $c^\dagger_{i\sigma}c_{j\sigma}\exp\left[\frac{ie}{\hbar c}\int_{\boldsymbol{r}_j}^{\boldsymbol{r}_i}\boldsymbol{A}(\boldsymbol{r})\cdot d\boldsymbol{r}\right]$, where e and c are the elementary electric charge and the light velocity, respectively, and then the applied electric field $\boldsymbol{E}(t)$ reads as $-\partial\boldsymbol{A}(t)/c\partial t$. Suppose $\gamma^\dagger_{\boldsymbol{q},p}$ creates a photon of momentum $\boldsymbol{q}$, energy $\hbar\omega_{\boldsymbol{q}}$, and polarization p, then the second-quantized vector potential is written as

$$\boldsymbol{A}(\boldsymbol{r}) = \sum_{\boldsymbol{q},p}\sqrt{\frac{hc^2}{V\omega_{\boldsymbol{q}}}}\left(\boldsymbol{e}_{\boldsymbol{q},p}\gamma_{\boldsymbol{q},p}e^{i\boldsymbol{q}\cdot\boldsymbol{r}} + \boldsymbol{e}^*_{\boldsymbol{q},p}\gamma^\dagger_{\boldsymbol{q},p}e^{-i\boldsymbol{q}\cdot\boldsymbol{r}}\right) \tag{2.2}$$

with V being the appropriate volume of the sample. For visible light, we may put $e^{i\boldsymbol{q}\cdot\boldsymbol{r}} \simeq 1$ and therefore denote $\boldsymbol{A}(\boldsymbol{r})$ simply by $\boldsymbol{A}$ hereafter. Then the electron-photon-coupled Hamiltonian reads

$$\begin{aligned}\mathscr{H}_{\text{el-ph}} &= \mathscr{H} + \Omega + \sum_{m=1}^{\infty}{}^{[m]}\mathscr{J};\ \Omega \equiv \sum_{\boldsymbol{q},p}\hbar\omega_{\boldsymbol{q}}\gamma^\dagger_{\boldsymbol{q},p}\gamma_{\boldsymbol{q},p},\\ {}^{[m]}\mathscr{J} &\equiv -t\sum_{\langle i,j\rangle}\sum_{\sigma=\uparrow,\downarrow}\frac{1}{m!}\left[c^\dagger_{i\sigma}c_{j\sigma}\left(\frac{-ie}{\hbar c}\boldsymbol{A}\cdot\boldsymbol{d}_{i,j}\right)^m + \text{H.c.}\right]\\ &= -t\sum_{i,j=1}^{L}l_{i,j}\sum_{\sigma=\uparrow,\downarrow}\frac{1}{m!}c^\dagger_{i\sigma}c_{j\sigma}\left(\frac{-ie}{\hbar c}\boldsymbol{A}\cdot\boldsymbol{d}_{i,j}\right)^m\end{aligned} \tag{2.3}$$

with $l_{i,j}$ being 1 for connected vertices i and j, otherwise 0, and $\boldsymbol{d}_{i,j} \equiv \boldsymbol{r}_j - \boldsymbol{r}_i$.

We treat the photoinduced current operators ${}^{[m]}\mathscr{J}$ as the perturbations to $\mathscr{H}+\Omega$. The transition rate between arbitrary states, $|i\rangle$ of energy ε_i and $|f\rangle$ of energy ε_f, each being a product of electronic and photonic states, are given as

$$W_{i,f} = \frac{2\pi}{\hbar}\left|\langle f|\mathscr{T}|i\rangle\right|^2\delta(\varepsilon_f-\varepsilon_i). \tag{2.4}$$

Any Raman scattering contains two photons, starting with an incident photon and ending in a scattered photon, where (2.2) is explicitly written as

$$\boldsymbol{A} = \sqrt{\frac{hc^2}{V\omega_{\rm in}}}\boldsymbol{e}_{\rm in}\gamma_{\boldsymbol{q}_{\rm in},\boldsymbol{e}_{\rm in}} + \sqrt{\frac{hc^2}{V\omega_{\rm sc}}}\boldsymbol{e}^*_{\rm sc}\gamma^\dagger_{\boldsymbol{q}_{\rm sc},\boldsymbol{e}_{\rm sc}} \tag{2.5}$$

with $\omega_{\rm in}$ ($\omega_{\rm sc}$), $\boldsymbol{q}_{\rm in}$ ($\boldsymbol{q}_{\rm sc}$), and $\boldsymbol{e}_{\rm in}$ ($\boldsymbol{e}_{\rm sc}$) being the frequency, momentum, and polarization of the incident (scattered) photon, respectively. The Raman transition matrix $\mathscr{T}$ in proportion to $\boldsymbol{A}^2$ reads

$$\mathscr{T} = {}^{[2]}\mathscr{J} + {}^{[1]}\mathscr{J}\frac{1}{\varepsilon_i - \Omega - \mathscr{H}_U - \mathscr{H}_t}{}^{[1]}\mathscr{J}. \tag{2.6}$$

Every magnetic Raman scattering demands that the electronic state should belong in the singly-occupied ground-state manifold at the beginning and end, where ${}^{[m]}\mathscr{J}$, inducing a single electron transfer, singly has no contribution to the transition rate, $\langle f|{}^{[m]}\mathscr{J}|i\rangle = 0$. Relevant intermediate states obtained by operating ${}^{[1]}\mathscr{J}$ on the initial state each have one doublon-holon pair together with no photon or two photons. The photonic state is also singly occupied at the beginning and end. Considering that $t \ll U$, we regard both ${}^{[m]}\mathscr{J}$ and $\mathscr{H}_t$ as perturbations to $\mathscr{H}_U$ and therefore express the effective Raman operator as

$$\begin{aligned}\mathcal{R} =& \mathcal{P}\,{}^{[1]}\mathscr{J}\frac{1}{\varepsilon_i - \Omega - \mathscr{H}_U - \mathscr{H}_t}{}^{[1]}\mathscr{J}\mathcal{P} \\ =& \mathcal{P}\,{}^{[1]}\mathscr{J}\frac{1}{\varepsilon_i - \Omega - \mathscr{H}_U}\sum_{n=0}^{\infty}\left(\mathscr{H}_t\frac{1}{\varepsilon_i - \Omega - \mathscr{H}_U}\right)^n {}^{[1]}\mathscr{J}\mathcal{P},\end{aligned} \tag{2.7}$$

where $\mathcal{P}$ is the projection operator to the singly-occupied ground-state manifold.

No-photon and two-photon intermediate states are higher in energy than the ground state by $U-\hbar\omega_{\rm in}$ and $U+\hbar\omega_{\rm sc}$, respectively. Assuming that the incident photon energy is comparable to the electronic correlation energy, $t \lesssim |U-\hbar\omega_{\rm in}| \ll U$, we may replace $(\varepsilon_i - \Omega - \mathscr{H}_U)^{-1}$ by $(\hbar\omega_{\rm in} - U)^{-1}$. With the single occupancy at every site in mind, we express the electron operators in terms of the spin operators,

$$\mathcal{P}c^\dagger_{i\sigma_1}c_{i\sigma_2}\mathcal{P} = \frac{1}{2}\delta_{\sigma_1,\sigma_2} + \sum_{\mu=x,y,z} S^\mu_i\left[\boldsymbol{\sigma}^\mu\right]_{\sigma_2\sigma_1}, \tag{2.8}$$

where $\boldsymbol{\sigma}^\mu$'s are the Pauli matrices.

The lowest-order $n=0$ term in (2.7), which is of second order in t, reads

$$\begin{aligned}{}^{[2]}\mathcal{R} =& \frac{-1}{U-\hbar\omega_{\rm in}}\mathcal{P}\,{}^{[1]}\mathscr{J}\,{}^{[1]}\mathscr{J}\mathcal{P} \\ =& \frac{2\pi e^2}{\hbar V\sqrt{\omega_{\rm in}\omega_{\rm sc}}}\frac{t^2}{U-\hbar\omega_{\rm in}}\sum_{i_1,j_1=1}^{L} l_{i_1,j_1}\sum_{i_2,j_2=1}^{L} l_{i_2,j_2}\sum_{\sigma_1,\sigma_2}(\boldsymbol{e}^*_{\rm sc}\cdot\boldsymbol{d}_{i_2,j_2})(\boldsymbol{e}_{\rm in}\cdot\boldsymbol{d}_{i_1,j_1}) \\ & \times \mathcal{P}c^\dagger_{i_2\sigma_2}c_{j_2\sigma_2}c^\dagger_{i_1\sigma_1}c_{j_1\sigma_1}\mathcal{P} \\ =& \frac{2\pi e^2}{\hbar V\sqrt{\omega_{\rm in}\omega_{\rm sc}}}\frac{t^2}{U-\hbar\omega_{\rm in}}\sum_{i_1,j_1=1}^{L} l_{i_1,j_1}\sum_{\sigma_1,\sigma_2}(\boldsymbol{e}^*_{\rm sc}\cdot\boldsymbol{d}_{j_1,i_1})(\boldsymbol{e}_{\rm in}\cdot\boldsymbol{d}_{i_1,j_1})\mathcal{P}c^\dagger_{j_1\sigma_2}c_{i_1\sigma_2}c^\dagger_{i_1\sigma_1}c_{j_1\sigma_1}\mathcal{P}.\end{aligned} \tag{2.9}$$

Converting the electron operators into spin operators with the use of the anticommutation relation and the projection (2.8) and discarding Rayleigh (elastic scattering) terms, we obtain the well-known Loudon-Fleury Raman vertex [30]

$$ {}^{[2]}\mathcal{R} = \frac{2\pi e^2}{\hbar V\sqrt{\omega_{\rm in}\omega_{\rm sc}}}\frac{4t^2}{U-\hbar\omega_{\rm in}}\sum_{\langle i,j\rangle}(\boldsymbol{e}_{\rm in}\cdot\boldsymbol{d}_{i,j})(\boldsymbol{e}^*_{\rm sc}\cdot\boldsymbol{d}_{i,j})\boldsymbol{S}_i\cdot\boldsymbol{S}_j. \tag{2.10} $$

The Loudon-Fleury second-order mechanism predominates in the Raman response when the incident photon energy $\hbar\omega_{\rm in}$ is in the far-resonant regime, $t \ll |U-\hbar\omega_{\rm in}|$.

The $n=1$ term in (2.7), which is of third order in t, and the odd-integral-n ones in general, vanish by virtue of the electron-hole symmetry. Note that even though n is an odd integer, the electronic state can come back again into the singly-occupied ground-state manifold at the end in a triangular lattice, for instance. With the electron band being half filled, creation and annihilation of an electron can be described in terms of a hole as

$$ d^\dagger_{i\sigma} = (-1)^{\delta_{\sigma,\uparrow}}c_{i\bar\sigma},\ c^\dagger_{i\sigma} = (-1)^{\delta_{\sigma,\downarrow}}d_{i\bar\sigma}\ (\bar\sigma\equiv-\sigma). \tag{2.11} $$

With this in mind, the $n=1$ Raman vertex reads

$$ \begin{aligned} {}^{[3]}\mathcal{R} &= \frac{1}{(U-\hbar\omega_{\rm in})^2}\mathcal{P}\,{}^{[1]}\mathscr{J}\,\mathscr{H}_t\,{}^{[1]}\mathscr{J}\,\mathcal{P} \\ &= \frac{2\pi e^2}{\hbar V\sqrt{\omega_{\rm in}\omega_{\rm sc}}}\frac{t^3}{(U-\hbar\omega_{\rm in})^2}\sum_{i_1,j_1=1}^{L}l_{i_1,j_1}\sum_{i_2,j_2=1}^{L}l_{i_2,j_2}\sum_{i_3,j_3=1}^{L}l_{i_3,j_3} \\ &\quad\times\sum_{\sigma_1,\sigma_2,\sigma_3}(\boldsymbol{e}^*_{\rm sc}\cdot\boldsymbol{d}_{i_3,j_3})(\boldsymbol{e}_{\rm in}\cdot\boldsymbol{d}_{i_1,j_1})\mathcal{P}c^\dagger_{i_3\sigma_3}c_{j_3\sigma_3}c^\dagger_{i_2\sigma_2}c_{j_2\sigma_2}c^\dagger_{i_1\sigma_1}c_{j_1\sigma_1}\mathcal{P} \\ &= \frac{2\pi e^2}{\hbar V\sqrt{\omega_{\rm in}\omega_{\rm sc}}}\frac{t^3}{(U-\hbar\omega_{\rm in})^2}\sum_{i_1,j_1=1}^{L}l_{i_1,j_1}\sum_{i_2,j_2=1}^{L}l_{i_2,j_2}\sum_{i_3,j_3=1}^{L}l_{i_3,j_3} \\ &\quad\times\sum_{\sigma_1,\sigma_2,\sigma_3}(\boldsymbol{e}^*_{\rm sc}\cdot\boldsymbol{d}_{i_3,j_3})(\boldsymbol{e}_{\rm in}\cdot\boldsymbol{d}_{i_1,j_1}) \\ &\quad\times\frac{1}{2}\mathcal{P}\left[c^\dagger_{i_3\sigma_3}c_{j_3\sigma_3}c^\dagger_{i_2\sigma_2}c_{j_2\sigma_2}c^\dagger_{i_1\sigma_1}c_{j_1\sigma_1}+(-1)^3d^\dagger_{i_3\sigma_3}d_{j_3\sigma_3}d^\dagger_{i_2\sigma_2}d_{j_2\sigma_2}d^\dagger_{i_1\sigma_1}d_{j_1\sigma_1}\right]\mathcal{P}. \end{aligned} \tag{2.12} $$

Substituting (2.11) into (2.8) with the single-occupancy constraint $\sum_{\sigma=\uparrow,\downarrow}d^\dagger_{i\sigma}d_{i\sigma}=1$ in mind yeilds

$$ \begin{aligned} \mathcal{P}c^\dagger_{i\sigma_1}c_{i\sigma_2}\mathcal{P} &= \mathcal{P}(-1)^{\delta_{\sigma_1,\downarrow}+\delta_{\sigma_2,\downarrow}}\left(\delta_{\bar\sigma_1,\bar\sigma_2}-d^\dagger_{i\bar\sigma_2}d_{i\bar\sigma_1}\right)\mathcal{P} \\ &= \mathcal{P}\left[\delta_{\sigma_1,\sigma_2}+(-1)^{\delta_{\sigma_1,\sigma_2}}d^\dagger_{i\bar\sigma_2}d_{i\bar\sigma_1}\right]\mathcal{P} = \mathcal{P}d^\dagger_{i\sigma_1}d_{i\sigma_2}\mathcal{P}, \end{aligned} \tag{2.13} $$

showing that the electron and hole at each site have the same spin projection, and therefore, (2.12) vanishes. Likewise, all the odd-integral-n vertices contribute nothing to the Raman intensity of our system (2.3).

The next leading $n=2$ term in (2.7), which is of fourth order in t, reads

$$ \begin{aligned} {}^{[4]}\mathcal{R} =& \frac{-1}{(U-\hbar\omega_{\rm in})^3}\mathcal{P}\,{}^{[1]}\mathscr{J}\,\mathscr{H}_t\mathscr{H}_t\,{}^{[1]}\mathscr{J}\,\mathcal{P} \\ =& \frac{2\pi e^2}{\hbar V\sqrt{\omega_{\rm in}\omega_{\rm sc}}}\frac{t^4}{(U-\hbar\omega_{\rm in})^3}\sum_{i_1,j_1=1}^{L}l_{i_1,j_1}\sum_{i_2,j_2=1}^{L}l_{i_2,j_2}\sum_{i_3,j_3=1}^{L}l_{i_3,j_3}\sum_{i_4,j_4=1}^{L}l_{i_4,j_4} \end{aligned} $$

$$\times \sum_{\sigma_1,\sigma_2,\sigma_3,\sigma_4} (\boldsymbol{e}_{\rm sc}^* \cdot \boldsymbol{d}_{i_4,j_4})(\boldsymbol{e}_{\rm in} \cdot \boldsymbol{d}_{i_1,j_1}) \mathcal{P} c^\dagger_{i_4\sigma_4} c_{j_4\sigma_4} c^\dagger_{i_3\sigma_3} c_{j_3\sigma_3} c^\dagger_{i_2\sigma_2} c_{j_2\sigma_2} c^\dagger_{i_1\sigma_1} c_{j_1\sigma_1} \mathcal{P}. \quad (2.14)$$

Figure 2.1 shows in what order how many electrons move in a variety of fourth-order hopping paths. The site indices determine by the restrictions of the initial, intermediate, and final states, respectively. After some algebra, the fourth-order Raman vertex is obtained as

$$\begin{aligned}
{}^{[4]}\mathcal{R} = {} & \frac{2\pi e^2}{\hbar V\sqrt{\omega_{\rm in}\omega_{\rm sc}}} \frac{t^4}{(U-\hbar\omega_{\rm in})^3} \sum_{\langle i_1,i_2,i_3,i_4\rangle} \\
& \times \Bigg\{ -4\mathcal{Q}\Big[(\boldsymbol{S}_{i_1}\cdot\boldsymbol{S}_{i_2})(\boldsymbol{S}_{i_3}\cdot\boldsymbol{S}_{i_4}) + (\boldsymbol{S}_{i_1}\cdot\boldsymbol{S}_{i_4})(\boldsymbol{S}_{i_3}\cdot\boldsymbol{S}_{i_2}) - (\boldsymbol{S}_{i_1}\cdot\boldsymbol{S}_{i_3})(\boldsymbol{S}_{i_2}\cdot\boldsymbol{S}_{i_4})\Big] \\
& \quad + 2i\sum_{n=1}^{4} \mathcal{T}_n \boldsymbol{S}_{i_{n+2}} \cdot (\boldsymbol{S}_{i_{n+1}} \times \boldsymbol{S}_{i_n}) + \sum_{n=1}^{4} \mathcal{D}_n^+ \boldsymbol{S}_{i_n}\cdot\boldsymbol{S}_{i_{n+1}} + \sum_{n=1}^{2} \mathcal{D}_n^\times \boldsymbol{S}_{i_n}\cdot\boldsymbol{S}_{i_{n+2}} \Bigg\} \\
& + \frac{2\pi e^2}{\hbar V\sqrt{\omega_{\rm in}\omega_{\rm sc}}} \frac{t^4}{(U-\hbar\omega_{\rm in})^3} \sum_{\langle i_1,i_2,i_3\rangle} \\
& \times \left\{ 4i\widetilde{\mathcal{T}}\boldsymbol{S}_{i_3}\cdot(\boldsymbol{S}_{i_2}\times\boldsymbol{S}_{i_1}) + 2\sum_{n=1}^{2} \widetilde{\mathcal{D}}_n^+ \boldsymbol{S}_{i_n}\cdot\boldsymbol{S}_{i_{n+1}} - 2\widetilde{\mathcal{D}}^\times \boldsymbol{S}_{i_1}\cdot\boldsymbol{S}_{i_3} \right\}; \quad (2.15)
\end{aligned}$$

$$\mathcal{Q} \equiv \sum_{n=1}^{4} (\boldsymbol{e}_{\rm in}\cdot\boldsymbol{d}_{n,n+1}) \left[\boldsymbol{e}_{\rm sc}^*\cdot(\boldsymbol{d}_{n+1,n+2} + 2\boldsymbol{d}_{n+2,n+3} + \boldsymbol{d}_{n+3,n})\right], \quad (2.15a)$$

$$\begin{aligned}
\mathcal{T}_n \equiv {} & (\boldsymbol{e}_{\rm in}\cdot\boldsymbol{d}_{n,n+1}) \left[\boldsymbol{e}_{\rm sc}^*\cdot(-\boldsymbol{d}_{n+1,n+2} - 2\boldsymbol{d}_{n+2,n+3} + \boldsymbol{d}_{n+3,n})\right] \\
& + (\boldsymbol{e}_{\rm in}\cdot\boldsymbol{d}_{n+1,n+2}) \left[\boldsymbol{e}_{\rm sc}^*\cdot(-\boldsymbol{d}_{n+2,n+3} + 2\boldsymbol{d}_{n+3,n} + \boldsymbol{d}_{n,n+1})\right] \\
& + (\boldsymbol{e}_{\rm in}\cdot\boldsymbol{d}_{n+2,n+3}) \left[\boldsymbol{e}_{\rm sc}^*\cdot(\boldsymbol{d}_{n+3,n} + 2\boldsymbol{d}_{n,n+1} + \boldsymbol{d}_{n+1,n+2})\right] \\
& + (\boldsymbol{e}_{\rm in}\cdot\boldsymbol{d}_{n+3,n}) \left[\boldsymbol{e}_{\rm sc}^*\cdot(-\boldsymbol{d}_{n,n+1} - 2\boldsymbol{d}_{n+1,n+2} - \boldsymbol{d}_{n+2,n+3})\right], \quad (2.15b)
\end{aligned}$$

$$\begin{aligned}
\mathcal{D}_n^+ \equiv {} & (\boldsymbol{e}_{\rm in}\cdot\boldsymbol{d}_{n,n+1}) \left[\boldsymbol{e}_{\rm sc}^*\cdot(-\boldsymbol{d}_{n+1,n+2} + 2\boldsymbol{d}_{n+2,n+3} - \boldsymbol{d}_{n+3,n})\right] \\
& + (\boldsymbol{e}_{\rm in}\cdot\boldsymbol{d}_{n+1,n+2}) \left[\boldsymbol{e}_{\rm sc}^*\cdot(\boldsymbol{d}_{n+2,n+3} - 2\boldsymbol{d}_{n+3,n} - \boldsymbol{d}_{n,n+1})\right] \\
& + (\boldsymbol{e}_{\rm in}\cdot\boldsymbol{d}_{n+2,n+3}) \left[\boldsymbol{e}_{\rm sc}^*\cdot(\boldsymbol{d}_{n+3,n} + 2\boldsymbol{d}_{n,n+1} + \boldsymbol{d}_{n+1,n+2})\right] \\
& + (\boldsymbol{e}_{\rm in}\cdot\boldsymbol{d}_{n+3,n}) \left[\boldsymbol{e}_{\rm sc}^*\cdot(-\boldsymbol{d}_{n,n+1} - 2\boldsymbol{d}_{n+1,n+2} + \boldsymbol{d}_{n+2,n+3})\right], \quad (2.15c)
\end{aligned}$$

$$\begin{aligned}
\mathcal{D}_n^\times \equiv {} & (\boldsymbol{e}_{\rm in}\cdot\boldsymbol{d}_{n,n+1}) \left[\boldsymbol{e}_{\rm sc}^*\cdot(\boldsymbol{d}_{n+1,n+2} + 2\boldsymbol{d}_{n+2,n+3} - \boldsymbol{d}_{n+3,n})\right] \\
& + (\boldsymbol{e}_{\rm in}\cdot\boldsymbol{d}_{n+1,n+2}) \left[\boldsymbol{e}_{\rm sc}^*\cdot(-\boldsymbol{d}_{n+2,n+3} + 2\boldsymbol{d}_{n+3,n} + \boldsymbol{d}_{n,n+1})\right] \\
& + (\boldsymbol{e}_{\rm in}\cdot\boldsymbol{d}_{n+2,n+3}) \left[\boldsymbol{e}_{\rm sc}^*\cdot(\boldsymbol{d}_{n+3,n} + 2\boldsymbol{d}_{n,n+1} - \boldsymbol{d}_{n+1,n+2})\right] \\
& + (\boldsymbol{e}_{\rm in}\cdot\boldsymbol{d}_{n+3,n}) \left[\boldsymbol{e}_{\rm sc}^*\cdot(-\boldsymbol{d}_{n,n+1} + 2\boldsymbol{d}_{n+1,n+2} + \boldsymbol{d}_{n+2,n+3})\right], \quad (2.15d)
\end{aligned}$$

$$\widetilde{\mathcal{T}} \equiv (\boldsymbol{e}_{\rm in}\cdot\boldsymbol{d}_{1,2})(\boldsymbol{e}_{\rm sc}^*\cdot\boldsymbol{d}_{2,3}) - (\boldsymbol{e}_{\rm in}\cdot\boldsymbol{d}_{2,3})(\boldsymbol{e}_{\rm sc}^*\cdot\boldsymbol{d}_{1,2}), \quad (2.15e)$$

$$\widetilde{\mathcal{D}}_n^+ \equiv (\boldsymbol{e}_{\rm in}\cdot\boldsymbol{d}_{n,n+1}) \left[\boldsymbol{e}_{\rm sc}^*\cdot(\boldsymbol{d}_{1,2} + \boldsymbol{d}_{2,3})\right] + \left[\boldsymbol{e}_{\rm in}\cdot(\boldsymbol{d}_{1,2} + \boldsymbol{d}_{2,3})\right](\boldsymbol{e}_{\rm sc}^*\cdot\boldsymbol{d}_{n,n+1}), \quad (2.15f)$$

$$\widetilde{\mathcal{D}}^\times \equiv (\boldsymbol{e}_{\rm in}\cdot\boldsymbol{d}_{1,2})(\boldsymbol{e}_{\rm sc}^*\cdot\boldsymbol{d}_{2,3}) + (\boldsymbol{e}_{\rm in}\cdot\boldsymbol{d}_{2,3})(\boldsymbol{e}_{\rm sc}^*\cdot\boldsymbol{d}_{1,2}), \quad (2.15g)$$

where $\sum_{\langle i_1,i_2,i_3,i_4\rangle}$ and $\sum_{\langle i_1,i_2,i_3\rangle}$ run over four-site-cyclic and three-site-round paths, respectively, and we abbreviate $\boldsymbol{d}_{i_n,i_{n'}} \equiv \boldsymbol{r}_{i_{n'}} - \boldsymbol{r}_{i_n}$ as $\boldsymbol{d}_{n,n'}$ with $1 \le n, n' \pmod 4 \le 4$. The Shastry-Shraiman fourth-order mechanism is of major importance in the Raman response when the incident photon energy $\hbar\omega_{\rm in}$ is in the near-resonant regime, $t \simeq |U - \hbar\omega_{\rm in}|$.

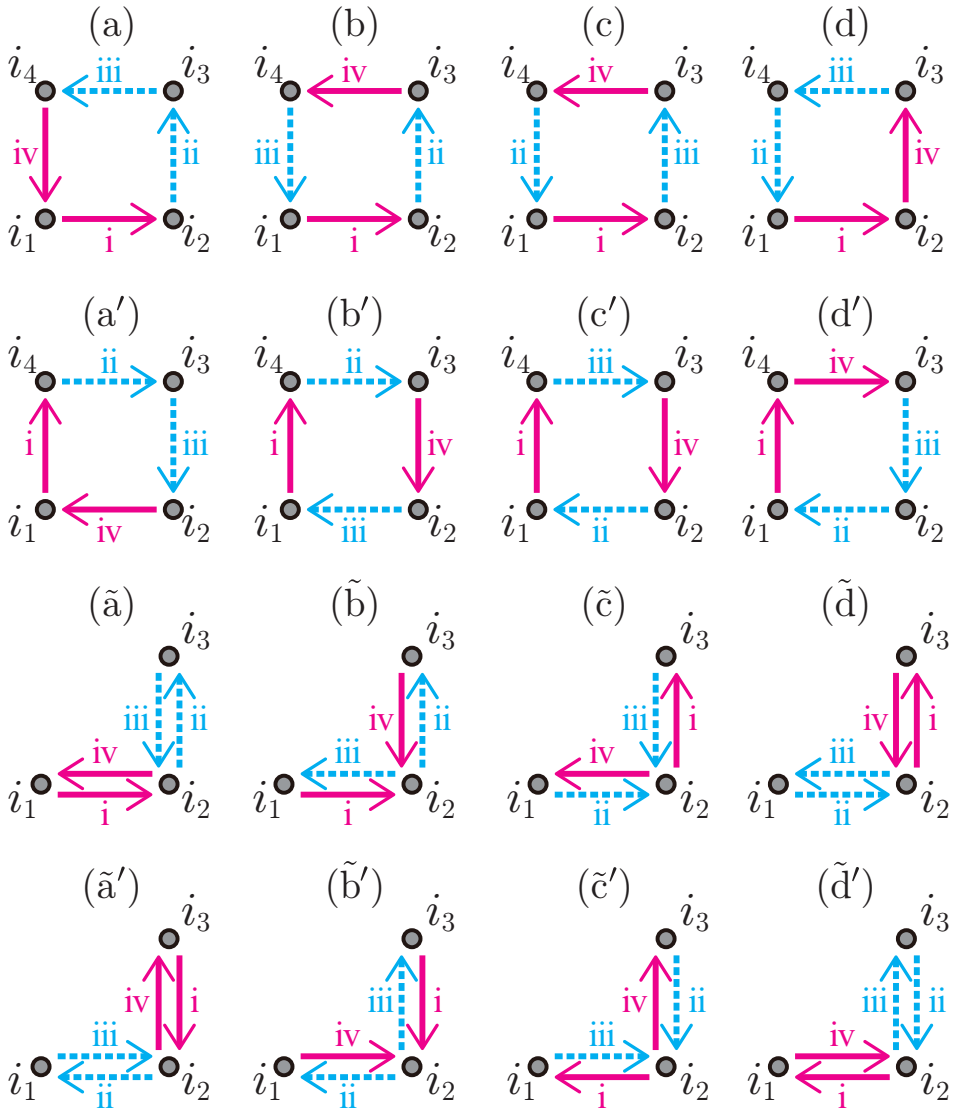

Figure 2.1: Fourth-order electron hopping paths. (a)-(d) and (a′)-(d′) are cyclic paths, while (ã)-(d̃) and (ã′)-(d̃′) are round paths. Solid arrows create or annihilate a doublon-holon pair arising from $^{[1]}\mathscr{J}$, whereas broken arrows correspond to electron transfer arising from $\mathscr{H}_t$.

Chapter 3

Spin-Wave Theory

3.1 Diagonalization

We discuss antiferromagnetic Heisenberg models on the two-dimensional Penrose [54, 55] and Ammann-Beenker [56, 57] lattices of point symmetry $\mathbf{C}_{5\mathrm{v}}$ and $\mathbf{C}_{8\mathrm{v}}$, respectively, both of which are described by the Hamiltonian

$$\mathcal{H} = J \sum_{\langle i,j \rangle} \boldsymbol{S}_i \cdot \boldsymbol{S}_j \ (J > 0), \tag{3.1}$$

where $\boldsymbol{S}_i$ is the vector spin-$\frac{1}{2}$ operator at site i and $\sum_{\langle i,j \rangle}$ runs over all pairs of connected vertices. Since the Penrose and Ammann-Beenker lattices are both bipartite, we divide them each into two sublattices, A with L_{A} sites and B with $L_{\mathrm{B}}\,(\equiv L - L_{\mathrm{A}})$ sites, respectively. We introduce the bosonic spin deviation operators [58]

$$\begin{aligned} S_i^+ &= \left(2S - a_i^\dagger a_i\right)^{\frac{1}{2}} a_i, \ S_i^- = a_i^\dagger \left(2S - a_i^\dagger a_i\right)^{\frac{1}{2}}, \ S_i^z = S - a_i^\dagger a_i; \\ S_j^+ &= b_j^\dagger \left(2S - b_j^\dagger b_j\right)^{\frac{1}{2}}, \ S_j^- = \left(2S - b_j^\dagger b_j\right)^{\frac{1}{2}} b_j, \ S_j^z = b_j^\dagger b_j - S, \end{aligned} \tag{3.2}$$

where the site indices are understood as $i \in \mathrm{A}$ and $j \in \mathrm{B}$. We expand the Hamiltonian (3.1) in powers of the inverse spin magnitude $1/S$,

$$\mathcal{H} = \mathcal{H}^{(2)} + \mathcal{H}^{(1)} + \mathcal{H}^{(0)} + O(S^{-1}), \tag{3.3}$$

where $\mathcal{H}^{(m)}$, on the order of S^m, reads

$$\begin{aligned} \mathcal{H}^{(2)} &= -JS^2 \sum_{i \in \mathrm{A}} \sum_{j \in \mathrm{B}} l_{i,j}, \\ \mathcal{H}^{(1)} &= JS \sum_{i \in \mathrm{A}} \sum_{j \in \mathrm{B}} l_{i,j} \left(a_i^\dagger a_i + b_j^\dagger b_j + a_i b_j + a_i^\dagger b_j^\dagger\right), \\ \mathcal{H}^{(0)} &= -J \sum_{i \in \mathrm{A}} \sum_{j \in \mathrm{B}} l_{i,j} \left[a_i^\dagger a_i b_j^\dagger b_j + \frac{1}{4}\left(a_i^\dagger a_i a_i b_j + a_i^\dagger b_j^\dagger b_j^\dagger b_j + \mathrm{H.c.}\right)\right]. \end{aligned} \tag{3.4}$$

We decompose the $O(S^0)$ quartic Hamiltonian $\mathcal{H}^{(0)}$ into quadratic terms $\mathcal{H}^{(0)}_{\mathrm{BL}}$ and normal-ordered quartic terms $:\mathcal{H}^{(0)}:$ through Wick's theorem [59, 60],

$$a_i^\dagger a_i b_j^\dagger b_j = :a_i^\dagger a_i b_j^\dagger b_j :$$

$$
\begin{aligned}
&+ {}_{\rm BL}\langle 0|a_i^\dagger a_i|0\rangle_{\rm BL} b_j^\dagger b_j + {}_{\rm BL}\langle 0|b_j^\dagger b_j|0\rangle_{\rm BL} a_i^\dagger a_i \\
&+ {}_{\rm BL}\langle 0|a_i^\dagger b_j^\dagger|0\rangle_{\rm BL} a_i b_j + {}_{\rm BL}\langle 0|a_i b_j|0\rangle_{\rm BL} a_i^\dagger b_j^\dagger \\
&- {}_{\rm BL}\langle 0|a_i^\dagger a_i|0\rangle_{\rm BL}\,{}_{\rm BL}\langle 0|b_j^\dagger b_j|0\rangle_{\rm BL} - {}_{\rm BL}\langle 0|a_i^\dagger b_j^\dagger|0\rangle_{\rm BL}\,{}_{\rm BL}\langle 0|a_i b_j|0\rangle_{\rm BL}, \\
a_i^\dagger a_i a_i b_j =& : a_i^\dagger a_i a_i b_j : \\
&+ 2\left({}_{\rm BL}\langle 0|a_i^\dagger a_i|0\rangle_{\rm BL} a_i b_j + {}_{\rm BL}\langle 0|a_i b_j|0\rangle_{\rm BL} a_i^\dagger a_i\right) \\
&- 2{}_{\rm BL}\langle 0|a_i^\dagger a_i|0\rangle_{\rm BL}\,{}_{\rm BL}\langle 0|a_i b_j|0\rangle_{\rm BL}, \\
a_i^\dagger b_j^\dagger b_j^\dagger b_j =& : a_i^\dagger b_j^\dagger b_j^\dagger b_j : \\
&+ 2\left({}_{\rm BL}\langle 0|a_i^\dagger b_j^\dagger|0\rangle_{\rm BL} b_j^\dagger b_j + {}_{\rm BL}\langle 0|b_j^\dagger b_j|0\rangle_{\rm BL} a_i^\dagger b_j^\dagger\right) \\
&- 2{}_{\rm BL}\langle 0|a_i^\dagger b_j^\dagger|0\rangle_{\rm BL}\,{}_{\rm BL}\langle 0|b_j^\dagger b_j|0\rangle_{\rm BL},
\end{aligned}
\tag{3.5}
$$

where $|0\rangle_{\rm BL}$ denotes the quasiparticle magnon vacuum. The up-to-$O(S^0)$ bosonic Hamiltonian reads

$$
\mathcal{H} = \mathcal{H}^{(2)} + \mathcal{H}^{(1)} + \mathcal{H}^{(0)}_{\rm BL} + : \mathcal{H}^{(0)} :\equiv \mathcal{H}_{\rm BL} + : \mathcal{H}^{(0)} : . \tag{3.6}
$$

Let us express the bilinear Hamiltonian $\mathcal{H}_{\rm BL}$ as

$$
\mathcal{H}_{\rm BL} = \boldsymbol{c}^\dagger \mathcal{M} \boldsymbol{c} + \sum_{m=0}^{2} \tilde{E}^{(m)};\ \mathcal{M} \equiv \left[\begin{array}{c|c} \mathbf{A} & \mathbf{C} \\ \hline \mathbf{C}^\dagger & \mathbf{B} \end{array}\right], \tag{3.7}
$$

where we define the row vectors $\boldsymbol{a}^\dagger$ and $\boldsymbol{b}^\dagger$ of dimension $L_{\rm A}$ and $L_{\rm B}$, respectively,

$$
\boldsymbol{c}^\dagger = \left[a_1^\dagger, \cdots, a_{L_{\rm A}}^\dagger, b_1, \cdots, b_{L_{\rm B}}\right] \equiv \left[\boldsymbol{a}^\dagger, {}^t\boldsymbol{b}\right], \tag{3.8}
$$

the matrices $\mathbf{A}$, $\mathbf{B}$, and $\mathbf{C}$ of dimension $L_{\rm A} \times L_{\rm A}$, $L_{\rm B} \times L_{\rm B}$, and $L_{\rm A} \times L_{\rm B}$, respectively,

$$
\begin{aligned}
[\mathbf{A}]_{i,i'} =& J\delta_{i,i'} \sum_{j\in{\rm B}} l_{i,j} \left[S - {}_{\rm BL}\langle 0|b_j^\dagger b_j|0\rangle_{\rm BL} - \frac{1}{2}\left({}_{\rm BL}\langle 0|a_i b_j|0\rangle_{\rm BL} + {}_{\rm BL}\langle 0|a_i^\dagger b_j^\dagger|0\rangle_{\rm BL}\right)\right], \\
[\mathbf{B}]_{j,j'} =& J\delta_{j,j'} \sum_{i\in{\rm A}} l_{i,j} \left[S - {}_{\rm BL}\langle 0|a_i^\dagger a_i|0\rangle_{\rm BL} - \frac{1}{2}\left({}_{\rm BL}\langle 0|a_i b_j|0\rangle_{\rm BL} + {}_{\rm BL}\langle 0|a_i^\dagger b_j^\dagger|0\rangle_{\rm BL}\right)\right], \\
[\mathbf{C}]_{i,j} =& J l_{i,j} \left[S - {}_{\rm BL}\langle 0|a_i b_j|0\rangle_{\rm BL} - \frac{1}{2}\left({}_{\rm BL}\langle 0|a_i^\dagger a_i|0\rangle_{\rm BL} + {}_{\rm BL}\langle 0|b_j^\dagger b_j|0\rangle_{\rm BL}\right)\right],
\end{aligned}
\tag{3.9}
$$

and the constants

$$
\begin{aligned}
\tilde{E}^{(2)} &= \mathcal{H}^{(2)} \equiv E^{(2)}, \\
\tilde{E}^{(1)} &= -JS \sum_{i\in{\rm A}} \sum_{j\in{\rm B}} l_{i,j}, \\
\tilde{E}^{(0)} &= J \sum_{i\in{\rm A}} \sum_{j\in{\rm B}} l_{i,j} \Bigg[{}_{\rm BL}\langle 0|a_i^\dagger a_i|0\rangle_{\rm BL} + \frac{1}{2}\left({}_{\rm BL}\langle 0|a_i b_j|0\rangle_{\rm BL} + {}_{\rm BL}\langle 0|a_i^\dagger b_j^\dagger|0\rangle_{\rm BL}\right) \\
&\quad + {}_{\rm BL}\langle 0|a_i^\dagger a_i|0\rangle_{\rm BL}\,{}_{\rm BL}\langle 0|b_j^\dagger b_j|0\rangle_{\rm BL} + {}_{\rm BL}\langle 0|a_i^\dagger b_j^\dagger|0\rangle_{\rm BL}\,{}_{\rm BL}\langle 0|a_i b_j|0\rangle_{\rm BL} \\
&\quad + \frac{1}{2}\left({}_{\rm BL}\langle 0|a_i^\dagger a_i|0\rangle_{\rm BL} + {}_{\rm BL}\langle 0|b_j^\dagger b_j|0\rangle_{\rm BL}\right)\left({}_{\rm BL}\langle 0|a_i^\dagger b_j^\dagger|0\rangle_{\rm BL} + {}_{\rm BL}\langle 0|a_i b_j|0\rangle_{\rm BL}\right)\Bigg].
\end{aligned}
\tag{3.10}
$$

We carry out the Bogoliubov transformation

$$\boldsymbol{c} = \mathbf{X}\boldsymbol{\alpha};\ \mathbf{X} \equiv \left[\begin{array}{c|c} \mathbf{S} & \mathbf{U} \\ \hline \mathbf{V} & \mathbf{T} \end{array}\right], \tag{3.11}$$

where we define the matrices $\mathbf{S}$, $\mathbf{T}$, $\mathbf{U}$, and $\mathbf{V}$ of dimension $L_{\rm A} \times L_-$, $L_{\rm B} \times L_+$, $L_{\rm A} \times L_+$, and $L_{\rm B} \times L_-$, respectively, to obtain the ferromagnetic ($\alpha_{l_-}^{-\dagger}$) and antiferromagnetic ($\alpha_{l_+}^{+\dagger}$) magnon operators [62, 63]

$$\left[\alpha_1^{-\dagger}, \cdots, \alpha_{L_-}^{-\dagger}, \alpha_1^{+}, \cdots, \alpha_{L_+}^{+}\right] \equiv \boldsymbol{\alpha}^\dagger. \tag{3.12}$$

By virtue of the bosonic commutation relations, the Bogoliubov transformation matrix $\mathbf{X}$ satisfies [26, 61]

$$\begin{aligned} &\mathbf{X}\boldsymbol{\Gamma}'\mathbf{X}^\dagger = \boldsymbol{\Gamma},\ \mathbf{X}^\dagger\boldsymbol{\Gamma}\mathbf{X} = \boldsymbol{\Gamma}'; \\ &\boldsymbol{\Gamma} \equiv \left[\begin{array}{cc} -\mathbf{I}(L_{\rm A}) & 0 \\ 0 & \mathbf{I}(L_{\rm B}) \end{array}\right],\ \boldsymbol{\Gamma}' \equiv \left[\begin{array}{cc} -\mathbf{I}(L_-) & 0 \\ 0 & \mathbf{I}(L_+) \end{array}\right], \end{aligned} \tag{3.13}$$

where $\mathbf{I}(L)$ denotes the $L \times L$ identity matrix. Demanding that $\mathbf{X}$ should diagonalize $\mathcal{M}$, we obtain

$$\mathbf{X}^\dagger\mathcal{M}\mathbf{X} = {\rm diag}\left[\varepsilon_1^-, \cdots, \varepsilon_{L_-}^-, \varepsilon_1^+, \cdots, \varepsilon_{L_+}^+\right] \equiv \mathbf{E}, \tag{3.14}$$

where the eigenvalues $\varepsilon_{l_-}^-$ and $\varepsilon_{l_+}^+$ are non-negative. Multiplying (3.14) by $\mathbf{X}\boldsymbol{\Gamma}'$ from the left yields

$$\boldsymbol{\Gamma}\mathcal{M}\mathbf{X} = \mathbf{X}\boldsymbol{\Gamma}'\mathbf{E}. \tag{3.15}$$

The column vectors of $\mathbf{X}$ and the diagonal elements of $\boldsymbol{\Gamma}'\mathbf{E}$ are the right eigenvectors and their eigenvalues for $\boldsymbol{\Gamma}\mathcal{M}$, respectively.

The eigenvalues of $\boldsymbol{\Gamma}\mathcal{M}$ comprise L_- negative and L_+ positive eigenvalues [26],

$$\boldsymbol{\Gamma}'\mathbf{E} = \mathbf{E}' \equiv {\rm diag}\left[\varepsilon_1'^-, \cdots, \varepsilon_{L_-}'^-, \varepsilon_1'^+, \cdots, \varepsilon_{L_+}'^+\right]. \tag{3.16}$$

Having in mind that $(\boldsymbol{\Gamma}')^2 = \mathbf{I}(L)$, we find $\mathbf{E} = \boldsymbol{\Gamma}'\mathbf{E}'$. Then the non-negative eigenvalues $\varepsilon_{l_-}^-$ and $\varepsilon_{l_+}^+$ read

$$\varepsilon_{l_-}^- = -\varepsilon_{l_-}'^-,\ \varepsilon_{l_+}^+ = \varepsilon_{l_+}'^+ \tag{3.17}$$

to yield the diagonal one-body Hamiltonian

$$\mathcal{H}_{\rm BL} = \sum_{m=0}^{2} \tilde{E}^{(m)} + \sum_{l_-=1}^{L_-} \varepsilon_{l_-}^- \alpha_{l_-}^{-\dagger}\alpha_{l_-}^- + \sum_{l_+=1}^{L_+} \varepsilon_{l_+}^+ \alpha_{l_+}^+ \alpha_{l_+}^{+\dagger}. \tag{3.18}$$

Denoting the $O(S^m)$ component of $\varepsilon_{l_\sigma}^\sigma$ by $\varepsilon_{l_\sigma}^{\sigma(m)}$, we express the $O(S^0)$ quantum corrections to the classical ground-state energy $E^{(2)}$ as

$$E^{(m)} = \tilde{E}^{(m)} + \sum_{l_+=1}^{L_+} \varepsilon_{l_+}^{+(m)}\ (m = 1, 0), \tag{3.19}$$

and rewrite the Hamiltonian as

$$\mathcal{H}_{\rm BL} = \sum_{m=0}^{2} E^{(m)} + \sum_{\sigma=\pm} \sum_{l_\sigma=1}^{L_\sigma} \varepsilon_{l_\sigma}^{\sigma} \alpha_{l_\sigma}^{\sigma\dagger} \alpha_{l_\sigma}^{\sigma}. \tag{3.20}$$

Note that any finite cluster lie in the magnon vacuum at absolute zero, it is not necessarily the case with infinite lattices. In the thermodynamic limit of Heisenberg antiferromagnets on the Penrose and Ammann-Beenker lattices, Goldstone magnons may appear even at absolute zero. In such a case, every conventional spin-wave theory should be modified[59, 60]. The magnon eigenvalues $\varepsilon_{l_\sigma}^{\sigma}$ of the bosonic Hamiltonian (3.20) and quantum Monte Carlo specific heat C of the Heisenberg Hamiltonian (3.1) for various two-dimensional Penrose and Ammann-Beenker lattices are shown in Fig. 3.1. The major portion of the eigenvalues continuously distributes in almost the same energy region with almost the same pattern at each system size. The rest are isolated from them and strongly localized to sites with relatively high coordination numbers [26, 27]. Since there is not much of a difference in the temperature profile of the specific heat between various clusters, sites of the highest and/or second highest coordination numbers, which are possibly absent from small clusters, do not seriously affect the thermodynamic properties.

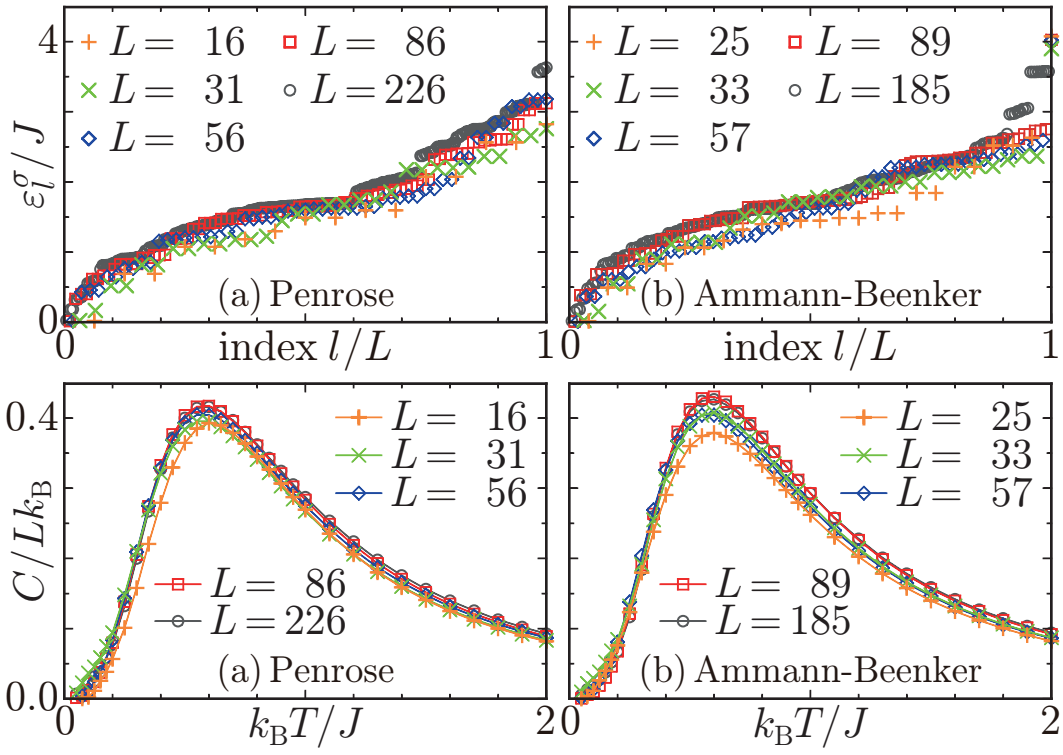

Figure 3.1: The eigenvalues $\varepsilon_l^\sigma (\sigma = \pm, 1 \le l \le L)$ of the bosonic Hamiltonian (3.20) and quantum Monte Carlo calculations of the specific heat C as a function of temperature T of the antiferromagnetic Heisenberg Hamiltonian (3.1) for various two-dimensional Penrose (a) and Ammann-Beenker (b) clusters of point symmetry $\mathbf{C}_{5\rm v}$ and $\mathbf{C}_{8\rm v}$, respectively.

The quartic normal-ordered interaction $:\mathcal{H}^{(0)}:$ is given by

$$
\begin{aligned}
:\mathcal{H}^{(0)}: := -J \sum_{i\in \mathrm{A}} \sum_{j\in \mathrm{B}} l_{i,j} \Bigg\{ & \sum_{l_-,l'_-,l''_-,l'''_-} V^{(1)}_{ij;l_-l'_-l''_-l'''_-} \alpha^{-\dagger}_{l_-} \alpha^{-\dagger}_{l'_-} \alpha^{-}_{l''_-} \alpha^{-}_{l'''_-} \\
& + \sum_{l_-,l'_+,l''_-,l'''_-} V^{(2)}_{ij;l_-l'_+l''_-l'''_-} \alpha^{-\dagger}_{l_-} \alpha^{+}_{l'_+} \alpha^{-}_{l''_-} \alpha^{-}_{l'''_-} + \sum_{l_+,l'_-,l''_-,l'''_-} V^{(3)}_{ij;l_+l'_-l''_-l'''_-} \alpha^{+\dagger}_{l_+} \alpha^{-\dagger}_{l'_-} \alpha^{-\dagger}_{l''_-} \alpha^{-}_{l'''_-} \\
& + \sum_{l_+,l'_+,l''_-,l'''_-} V^{(4)}_{ij;l_-l'_-l''_+l'''_+} \alpha^{+\dagger}_{l_+} \alpha^{+}_{l'_+} \alpha^{-\dagger}_{l''_-} \alpha^{-}_{l'''_-} + \sum_{l_+,l'_+,l''_+,l'''_-} V^{(5)}_{ij;l_+l'_+l''_+l'''_-} \alpha^{+\dagger}_{l_+} \alpha^{+}_{l'_+} \alpha^{+}_{l''_+} \alpha^{-}_{l'''_-} \\
& + \sum_{l_+,l'_+,l''_-,l'''_+} V^{(6)}_{ij;l_+l'_+l''_-l'''_+} \alpha^{+\dagger}_{l_+} \alpha^{+\dagger}_{l'_+} \alpha^{-\dagger}_{l''_-} \alpha^{+}_{l'''_+} + \sum_{l_+,l'_+,l''_-,l'''_-} V^{(7)}_{ij;l_+l'_+l''_-l'''_-} \alpha^{+\dagger}_{l_+} \alpha^{+\dagger}_{l'_+} \alpha^{-\dagger}_{l''_-} \alpha^{-\dagger}_{l'''_-} \\
& + \sum_{l_+,l'_+,l''_-,l'''_-} V^{(8)}_{ij;l_+l'_+l''_-l'''_-} \alpha^{+}_{l_+} \alpha^{+}_{l'_+} \alpha^{-}_{l''_-} \alpha^{-}_{l'''_-} + \sum_{l_+,l'_+,l''_+,l'''_+} V^{(9)}_{ij;l_+l'_+l''_+l'''_+} \alpha^{+\dagger}_{l_+} \alpha^{+\dagger}_{l'_+} \alpha^{+}_{l''_+} \alpha^{+}_{l'''_+} \Bigg\}
\end{aligned}
\tag{3.21}
$$

with $V^{(2)}_{ij;l_-l'_+l''_-l'''_-} = V^{(3)*}_{ij;l'_+l''_-l'''_-l_-}$, $V^{(5)}_{ij;l_+l'_+l''_+l'''_-} = V^{(6)*}_{ij;l''_+l'_+l_+l'''_-}$, and $V^{(7)}_{ij;l_+l'_+l''_-l'''_-} = V^{(8)*}_{ij;l_+l'_+l''_-l'''_-}$. Figure 3.2 shows the magnon-magnon interactions $V^{(m)}_{ij;l_\sigma l'_{\sigma'} l''_{\sigma''} l'''_{\sigma'''}}$ diagrammatically. We give the magnon-number-conserving interactions explicitly in particular,

$$
\begin{aligned}
& V^{(1)}_{ij;l_-l'_-l''_-l'''_-} \\
& \quad = \frac{1}{4} \left(s^*_{i,l_-} s_{i,l'''_-} v_{j,l''_-} v^*_{j,l'_-} + s^*_{i,l'_-} s_{i,l'''_-} v_{j,l''_-} v^*_{j,l_-} + s^*_{i,l_-} s_{i,l''_-} v_{j,l'''_-} v^*_{j,l'_-} + s^*_{i,l'_-} s_{i,l''_-} v_{j,l'''_-} v^*_{j,l_-} \right) \\
& \quad + \frac{1}{8} \Big(s^*_{i,l_-} s_{i,l'''_-} s_{i,l''_-} v^*_{j,l'_-} + s^*_{i,l_-} v_{j,l'''_-} v_{j,l''_-} v^*_{j,l'_-} + s_{i,l''_-} v_{j,l'''_-} v^*_{j,l_-} v^*_{j,l'_-} + s^*_{i,l_-} s^*_{i,l'_-} s_{i,l''_-} v_{j,l'''_-} \\
& \qquad + s^*_{i,l'_-} s_{i,l'''_-} s_{i,l''_-} v^*_{j,l_-} + s^*_{i,l'_-} v_{j,l'''_-} v_{j,l''_-} v^*_{j,l_-} + s_{i,l'''_-} v_{j,l''_-} v^*_{j,l_-} v^*_{j,l'_-} + s^*_{i,l_-} s^*_{i,l'_-} s_{i,l'''_-} v_{j,l''_-} \Big), \\
& V^{(4)}_{ij;l_+l'_+l''_-l'''_-} \\
& \quad = s^*_{i,l''_-} s_{i,l'''_-} t_{i,l_+} t^*_{i,l'_+} + s^*_{i,l''_-} u_{i,l_+} v_{i,l'''_-} t^*_{i,l'_+} + u^*_{i,l'_+} s_{i,l'''_-} t_{i,l_+} v^*_{i,l''_-} + u^*_{i,l'_+} u_{i,l_+} v_{i,l'''_-} v^*_{i,l''_-} \\
& \quad + \frac{1}{4} \Big(s^*_{i,l''_-} s_{i,l'''_-} u_{i,l_+} t^*_{i,l'_+} + s^*_{i,l''_-} u_{i,l_+} s_{i,l'''_-} t^*_{i,l'_+} + u^*_{i,l'_+} s_{i,l'''_-} u_{i,l_+} v^*_{i,l''_-} + u^*_{i,l'_+} u_{i,l_+} s_{i,l'''_-} v^*_{i,l''_-} \\
& \qquad + s^*_{i,l''_-} v_{i,l'''_-} t_{i,l_+} t^*_{i,l'_+} + s^*_{i,l''_-} t_{i,l_+} v_{i,l'''_-} t^*_{i,l'_+} + u^*_{i,l'_+} v_{i,l'''_-} t_{i,l_+} v^*_{i,l''_-} + u^*_{i,l'_+} t_{i,l_+} v_{i,l'''_-} v^*_{i,l''_-} \Big) \\
& \quad + \frac{1}{2} \left(s_{i,l'''_-} t_{i,l_+} v^*_{i,l''_-} t^*_{i,l'_+} + u_{i,l_+} v_{i,l'''_-} v^*_{i,l''_-} t^*_{i,l'_+} + s^*_{i,l''_-} u^*_{i,l'_+} s_{i,l'''_-} t_{i,l_+} + s^*_{i,l''_-} u^*_{i,l'_+} u_{i,l_+} v_{i,l'''_-} \right), \\
& V^{(9)}_{ij;l_+l'_+l''_+l'''_+} \\
& \quad = \frac{1}{4} \left(u^*_{i,l''_+} u_{i,l'_+} t_{j,l_+} t^*_{j,l'''_+} + u^*_{i,l''_+} u_{i,l_+} t_{j,l'_+} t^*_{j,l'''_+} + u^*_{i,l'''_+} u_{i,l'_+} t_{j,l_+} t^*_{j,l''_+} + u^*_{i,l'''_+} u_{i,l_+} t_{j,l'_+} t^*_{j,l''_+} \right) \\
& \quad + \frac{1}{8} \Big(u^*_{i,l''_+} u_{i,l'_+} u_{i,l_+} t^*_{j,l'''_+} + u^*_{i,l''_+} t_{j,l'_+} t_{j,l_+} t^*_{j,l'''_+} + u_{i,l_+} t_{j,l'_+} t^*_{j,l''_+} t^*_{j,l'''_+} + u^*_{i,l''_+} u^*_{i,l'''_+} u_{i,l_+} t_{j,l'_+} \\
& \qquad + u^*_{i,l'''_+} u_{i,l'_+} u_{i,l_+} t^*_{j,l''_+} + u^*_{i,l'''_+} t_{j,l'_+} t_{j,l_+} t^*_{j,l''_+} + u_{i,l'_+} t_{j,l_+} t^*_{j,l''_+} t^*_{j,l'''_+} + u^*_{i,l''_+} u^*_{i,l'''_+} u_{i,l'_+} t_{j,l_+} \Big),
\end{aligned}
\tag{3.22}
$$

in terms of the matrix elements $s_{i,l_-} \equiv [\mathbf{S}]_{i,l_-}$, $t_{j,l_+} \equiv [\mathbf{T}]_{j,l_+}$, $u_{i,l_+} \equiv [\mathbf{U}]_{i,l_+}$, and $v_{j,l_-} \equiv [\mathbf{V}]_{j,l_-}$ defined in (3.11).

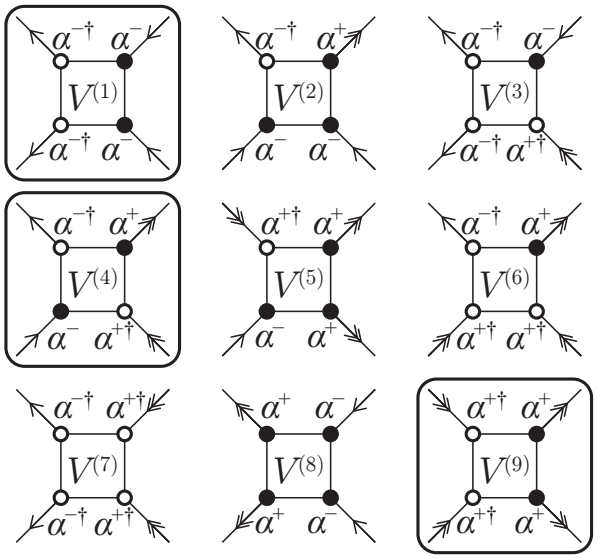

Figure 3.2: Diagrammatic representation of the magnon-magnon interactions $V^{(m)}_{ij;l_\sigma l'_{\sigma'} l''_{\sigma''} l'''_{\sigma'''}}$ emergent in (3.21). The open and closed circles each signify creating and annihilating a magnon, whether it is antiferromagnetic or ferromagnetic. The single and double arrowheads are to form antiferromagnetic and ferromagnetic magnon propagators, respectively, both of which enhance and reduce the magnetization when they are incoming and outgoing, respectively. The enclosed diagrams keep the number of magnons constant.

3.2 Bosonic Raman Operator

The Loudon-Fleury second-order Raman vertex ${}^{[2]}\mathcal{R}$ (2.10) consist of two-spin pair-exchange interactions $\boldsymbol{S}_i \cdot \boldsymbol{S}_j$, whereas the fourth-order vertices ${}^{[4]}\mathcal{R}$ (2.15) contain three-spin scalar-chirality terms $\boldsymbol{S}_i \cdot (\boldsymbol{S}_j \times \boldsymbol{S}_k)$ and four-spin ring-exchange terms $(\boldsymbol{S}_i \cdot \boldsymbol{S}_j)(\boldsymbol{S}_k \cdot \boldsymbol{S}_l)$ as well as the pair-exchange terms. The Raman operators are further classified by the number of the constituent spin operators, which we shall denote by τ,

$$\mathcal{R} \equiv \sum_{n=1}^{1\text{ or }2} {}^{[2n]}\mathcal{R} = \sum_{n=1}^{1\text{ or }2} \sum_{\tau=2}^{2n} {}^{[2n]}_{\tau}\mathcal{R};\ {}^{[2]}\mathcal{R} = {}^{[2]}_{2}\mathcal{R},\ {}^{[4]}\mathcal{R} = {}^{[4]}_{2}\mathcal{R} + {}^{[4]}_{3}\mathcal{R} + {}^{[4]}_{4}\mathcal{R}. \tag{3.23}$$

${}^{[2n]}_{2}\mathcal{R}$, ${}^{[2n]}_{3}\mathcal{R}$, ${}^{[2n]}_{4}\mathcal{R}$ consist of the pair-exchange, scalar-chirality, ring-exchange terms, respectively.

In terms of the bosonic language, the τ-spin Raman vertices are also expanded in $1/S$,

$${}^{[2n]}_{\tau}\mathcal{R} = \sum_{m=0}^{\infty} {}^{[2n]}_{\tau}\mathcal{R}^{(\tau-m)} = \sum_{m=0}^{\infty} \sum_{l=0}^{m} {}^{[2n]}_{\tau}\mathcal{R}^{(\tau-m)}_{2l\mathrm{M}}, \tag{3.24}$$

where ${}^{[2n]}_{\tau}\mathcal{R}^{(\tau-m)}$ is of order $S^{\tau-m}$ and can contain $2l\,(0 \le l \le m)$-magnon vertices. Via the Bogoliubov transformation, the up-to-$O(S^{\tau-2})$ vertices become

$$\mathcal{R} \equiv \sum_{l=1}^{2} \mathcal{R}_{2l\mathrm{M}} \equiv \sum_{l=1}^{2} \sum_{n=1}^{1\text{ or }2} {}^{[2n]}\mathcal{R}_{2l\mathrm{M}} \equiv \sum_{l=1}^{2} \sum_{n=1}^{1\text{ or }2} \sum_{\tau=2}^{2n} \sum_{m=l}^{2} {}^{[2n]}_{\tau}\mathcal{R}^{(\tau-m)}_{2l\mathrm{M}}, \tag{3.25}$$

where the four-magnon Raman vertices ${}^{[2n]}_{\tau}\mathcal{R}^{(\tau-2)}_{4\mathrm{M}}$ is normal-ordered by virtue of Wick's theorem with respect to the quasiparticle magnon operators. ${}^{[2n]}\mathcal{R}_{0\mathrm{M}}$ merely contributes to elastic (Rayleigh) scatterings and is thus omitted.

With a tacit understanding of the site indices being used as $i,k\in\mathrm{A}$ and $j,l\in\mathrm{B}$, various spin interactions are written in terms of Holstein-Primakoff bosons as

$$\begin{aligned}\boldsymbol{S}_i\cdot\boldsymbol{S}_j&=-S^2+S\left(a_i^\dagger a_i+b_j^\dagger b_j+a_ib_j+a_i^\dagger b_j^\dagger\right)\\&\quad-\left[a_i^\dagger a_ib_j^\dagger b_j+\frac{1}{4}\left(a_i^\dagger a_ia_ib_j+a_i^\dagger b_j^\dagger b_j^\dagger b_j+\mathrm{H.c.}\right)\right]+O(S^{-1}),\end{aligned}\tag{3.26}$$

$$\begin{aligned}\boldsymbol{S}_i\cdot\boldsymbol{S}_k&=S^2+S\left(-a_i^\dagger a_i-a_k^\dagger a_k+a_ia_k^\dagger+a_i^\dagger a_k\right)\\&\quad+\left[a_i^\dagger a_ia_k^\dagger a_k-\frac{1}{4}\left(a_i^\dagger a_ia_ia_k^\dagger+a_i^\dagger a_k^\dagger a_ka_k+\mathrm{H.c.}\right)\right]+O(S^{-1}),\end{aligned}\tag{3.27}$$

$$\begin{aligned}\boldsymbol{S}_j\cdot\boldsymbol{S}_l&=S^2+S\left(-b_j^\dagger b_j-b_l^\dagger b_l+b_jb_l^\dagger+b_j^\dagger b_l\right)\\&\quad+\left[b_j^\dagger b_jb_l^\dagger b_l-\frac{1}{4}\left(b_j^\dagger b_jb_jb_l^\dagger+b_j^\dagger b_l^\dagger b_lb_l+\mathrm{H.c.}\right)\right]+O(S^{-1}),\end{aligned}\tag{3.28}$$

$$\begin{aligned}i\boldsymbol{S}_i\cdot(\boldsymbol{S}_j\times\boldsymbol{S}_k)&=S^2\left(a_i^\dagger b_j^\dagger+a_i^\dagger a_k+a_kb_j-\mathrm{H.c.}\right)+S\Big[a_ib_ja_k^\dagger a_k+a_ia_k^\dagger b_j^\dagger b_j+a_i^\dagger a_ia_k^\dagger b_j^\dagger\\&\quad+\frac{1}{4}\left(a_i^\dagger a_ia_ib_j+a_ib_j^\dagger b_jb_j+a_ia_k^\dagger a_k^\dagger a_k+a_i^\dagger a_ia_ia_k^\dagger+a_k^\dagger a_k^\dagger a_kb_j^\dagger+a_k^\dagger b_j^\dagger b_j^\dagger b_j\right)-\mathrm{H.c.}\Big]+O(S^0),\end{aligned}\tag{3.29}$$

$$\begin{aligned}i\boldsymbol{S}_j\cdot(\boldsymbol{S}_k\times\boldsymbol{S}_l)&=S^2\left(a_k^\dagger b_j^\dagger+b_j^\dagger b_l+a_kb_l-\mathrm{H.c.}\right)+S\Big[a_kb_jb_l^\dagger b_l+a_k^\dagger a_kb_jb_l^\dagger+b_j^\dagger b_ja_k^\dagger b_l\\&\quad+\frac{1}{4}\left(a_k^\dagger a_ka_kb_j+a_kb_j^\dagger b_jb_j+b_jb_l^\dagger b_l^\dagger b_l+b_j^\dagger b_jb_jb_l^\dagger+a_k^\dagger a_k^\dagger a_kb_l^\dagger+a_k^\dagger b_l^\dagger b_l^\dagger b_l\right)-\mathrm{H.c.}\Big]+O(S^0),\end{aligned}\tag{3.30}$$

$$\begin{aligned}(\boldsymbol{S}_i\cdot\boldsymbol{S}_j)(\boldsymbol{S}_k\cdot\boldsymbol{S}_l)&=S^4-S^3\left(a_i^\dagger a_i+b_j^\dagger b_j+a_ib_j+a_i^\dagger b_j^\dagger+a_k^\dagger a_k+b_l^\dagger b_l+a_kb_l+a_k^\dagger b_l^\dagger\right)\\&\quad+S^2\Big[a_i^\dagger a_ia_k^\dagger a_k+a_i^\dagger a_ib_l^\dagger b_l+a_i^\dagger a_ia_kb_l+a_i^\dagger a_ia_k^\dagger b_l^\dagger+b_j^\dagger b_ja_k^\dagger a_k+b_j^\dagger b_jb_l^\dagger b_l+b_j^\dagger b_ja_kb_l+b_j^\dagger b_ja_k^\dagger b_l^\dagger\\&\quad+a_ib_ja_k^\dagger a_k+a_ib_jb_l^\dagger b_l+a_ib_ja_kb_l+a_ib_ja_k^\dagger b_l^\dagger+a_i^\dagger b_j^\dagger a_k^\dagger a_k+a_i^\dagger b_j^\dagger b_l^\dagger b_l+a_i^\dagger b_j^\dagger a_kb_l+a_i^\dagger b_j^\dagger a_k^\dagger b_l^\dagger\\&\quad+a_i^\dagger a_ib_j^\dagger b_j+\frac{1}{4}\left(a_i^\dagger a_ia_ib_j+a_i^\dagger b_j^\dagger b_j^\dagger b_j+\mathrm{H.c.}\right)+a_k^\dagger a_kb_l^\dagger b_l+\frac{1}{4}\left(a_k^\dagger a_ka_kb_l+a_k^\dagger b_l^\dagger b_l^\dagger b_l+\mathrm{H.c.}\right)\Big]\\&\quad+O(S^1),\end{aligned}\tag{3.31}$$

$$\begin{aligned}(\boldsymbol{S}_i\cdot\boldsymbol{S}_k)(\boldsymbol{S}_j\cdot\boldsymbol{S}_l)&=S^4+S^3\left(-a_i^\dagger a_i-a_k^\dagger a_k+a_ia_k^\dagger+a_i^\dagger a_k-b_j^\dagger b_j-b_l^\dagger b_l+b_jb_l^\dagger+b_j^\dagger b_l\right)\\&\quad+S^2\Big[a_i^\dagger a_ib_j^\dagger b_j+a_i^\dagger a_ib_l^\dagger b_l-a_i^\dagger a_ib_j^\dagger b_l-a_i^\dagger a_ib_jb_l^\dagger+a_k^\dagger a_kb_j^\dagger b_j+a_k^\dagger a_kb_l^\dagger b_l-a_k^\dagger a_kb_j^\dagger b_l-a_k^\dagger a_kb_jb_l^\dagger\\&\quad-a_ia_k^\dagger b_j^\dagger b_j-a_ia_k^\dagger b_l^\dagger b_l+a_ia_k^\dagger b_j^\dagger b_l+a_ia_k^\dagger b_jb_l^\dagger-a_i^\dagger a_kb_j^\dagger b_j-a_i^\dagger a_kb_l^\dagger b_l+a_i^\dagger a_kb_j^\dagger b_l+a_i^\dagger a_kb_jb_l^\dagger\\&\quad+a_i^\dagger a_ia_k^\dagger a_k-\frac{1}{4}\left(a_i^\dagger a_ia_ia_k^\dagger+a_i^\dagger a_k^\dagger a_ka_k+\mathrm{H.c.}\right)+b_j^\dagger b_jb_l^\dagger b_l-\frac{1}{4}\left(b_j^\dagger b_j^\dagger b_jb_l+b_jb_l^\dagger b_l^\dagger b_l+\mathrm{H.c.}\right)\Big]\\&\quad+O(S^1).\end{aligned}\tag{3.32}$$

Via Bogoliubov transformation (3.11), the two-magnon- and four-magnon-mediated Ra-

man scattering operators read

$$\sum_{n=1}^{p/2} {}^{[2n]}\mathcal{R}_{2\mathrm{M}} = \sum_{l_-,l'_-} {}^{[p]}W^{(1)}_{l_-l'_-}\,\alpha^{-\dagger}_{l_-}\alpha^{-}_{l'_-} + \sum_{l_+,l'_-} {}^{[p]}W^{(2)}_{l_+l'_-}\,\alpha^{+\dagger}_{l_+}\alpha^{-\dagger}_{l'_-} + \sum_{l_-,l'_+} {}^{[p]}W^{(3)}_{l_-l'_+}\,\alpha^{-}_{l_-}\alpha^{+}_{l'_+} + \sum_{l_+,l'_+} {}^{[p]}W^{(4)}_{l_+l'_+}\,\alpha^{+\dagger}_{l_+}\alpha^{+}_{l'_+} \tag{3.33}$$

with ${}^{[p]}W^{(2)}_{l_+l'_-} = {}^{[p]}W^{(3)\,*}_{l'_-l_+}$ and

$$\begin{aligned}\sum_{n=1}^{p/2} {}^{[2n]}\mathcal{R}_{4\mathrm{M}} = &\sum_{l_-,l'_-,l''_-,l'''_-} {}^{[p]}X^{(1)}_{l_-l'_-l''_-l'''_-}\alpha^{-\dagger}_{l_-}\alpha^{-\dagger}_{l'_-}\alpha^{-}_{l''_-}\alpha^{-}_{l'''_-} + \sum_{l_-,l'_+,l''_-,l'''_-} {}^{[p]}X^{(2)}_{l_-l'_+l''_-l'''_-}\alpha^{-\dagger}_{l_-}\alpha^{+}_{l'_+}\alpha^{-}_{l''_-}\alpha^{-}_{l'''_-}\\ &+ \sum_{l_+,l'_-,l''_-,l'''_-} {}^{[p]}X^{(3)}_{l_+l'_-l''_-l'''_-}\alpha^{+\dagger}_{l_+}\alpha^{-\dagger}_{l'_-}\alpha^{-\dagger}_{l''_-}\alpha^{-}_{l'''_-} + \sum_{l_+,l'_+,l''_-,l'''_-} {}^{[p]}X^{(4)}_{l_+l'_+l''_-l'''_-}\alpha^{+\dagger}_{l_+}\alpha^{+}_{l'_+}\alpha^{-\dagger}_{l''_-}\alpha^{-}_{l'''_-}\\ &+ \sum_{l_+,l'_+,l''_+,l'''_-} {}^{[p]}X^{(5)}_{l_+l'_+l''_+l'''_-}\alpha^{+\dagger}_{l_+}\alpha^{+}_{l'_+}\alpha^{+}_{l''_+}\alpha^{-}_{l'''_-} + \sum_{l_+,l'_+,l''_-,l'''_+} {}^{[p]}X^{(6)}_{l_+l'_+l''_-l'''_+}\alpha^{+\dagger}_{l_+}\alpha^{+\dagger}_{l'_+}\alpha^{-\dagger}_{l''_-}\alpha^{+}_{l'''_+}\\ &+ \sum_{l_+,l'_+,l''_-,l'''_-} {}^{[p]}X^{(7)}_{l_+l'_+l''_-l'''_-}\alpha^{+\dagger}_{l_+}\alpha^{+\dagger}_{l'_+}\alpha^{-\dagger}_{l''_-}\alpha^{-\dagger}_{l'''_-} + \sum_{l_+,l'_+,l''_-,l'''_-} {}^{[p]}X^{(8)}_{l_+l'_+l''_-l'''_-}\alpha^{+}_{l_+}\alpha^{+}_{l'_+}\alpha^{-}_{l''_-}\alpha^{-}_{l'''_-}\\ &+ \sum_{l_+,l'_+,l''_+,l'''_+} {}^{[p]}X^{(9)}_{l_+l'_+l''_+l'''_+}\alpha^{+\dagger}_{l_+}\alpha^{+\dagger}_{l'_+}\alpha^{+}_{l''_+}\alpha^{+}_{l'''_+}\end{aligned} \tag{3.34}$$

with ${}^{[p]}X^{(2)}_{l_-l'_+l''_-l'''_-} = {}^{[p]}X^{(3)\,*}_{l'_+l'''_-l''_-l_-}$, ${}^{[p]}X^{(5)}_{l_+l'_+l''_+l'''_-} = {}^{[p]}X^{(6)\,*}_{l''_+l'_+l'''_-l_+}$, and ${}^{[p]}X^{(7)}_{l_+l'_+l''_-l'''_-} = {}^{[p]}X^{(8)\,*}_{l_+l'_+l''_-l'''_-}$. The coefficients ${}^{[p]}W^{(m)}_{l_\sigma l'_{\sigma'}}$ and ${}^{[p]}X^{(m)}_{l_\sigma l'_{\sigma'}l''_{\sigma''}l'''_{\sigma'''}}$ are numerically obtained.

Chapter 4

Inelastic Photon Scattering

4.1 Magnetic Raman Scattering Intensity

The magnetic Raman scattering intensity at absolute zero is calulated by the Fourier trams-form of the correlation function of the the Loudon-Fleury ($p = 2$) and Shastry-Shraiman ($p = 4$) Raman operators as

$$ {}^{[p]}I(\omega) = \int_{-\infty}^{\infty} \frac{dt\, e^{i\omega t}}{2\pi\hbar L} \sum_{n,n'=1}^{p/2} \langle 0|{}^{[2n]}\mathcal{R}^{\dagger}(t)\, {}^{[2n']}\mathcal{R}|0\rangle, \tag{4.1} $$

where ${}^{[2n]}\mathcal{R}(t) \equiv e^{i\mathcal{H}t/\hbar}\, {}^{[2n]}\mathcal{R} e^{-i\mathcal{H}t/\hbar}$ is the time-dependent Raman operator of the Heisenberg picture and $|0\rangle$ denotes the ground state.

Once we find the exact ground state of the Heisenberg Hamiltonian, $\mathcal{H}|0\rangle = E_0|0\rangle$, the Loudon-Fleury ($p = 2$) and Shastry-Shraiman ($p = 4$) Raman scattering intensities can be exactly evaluated as [36, 64, 65, 66]

$$ {}^{[p]}I(\omega) = \frac{-1}{\pi L} \sum_{n,n'=1}^{p/2} \mathrm{Im}\langle 0|{}^{[2n]}\mathcal{R}^{\dagger} \frac{1}{\hbar\omega + E_0 + i\eta - \mathcal{H}} {}^{[2n']}\mathcal{R}|0\rangle, \tag{4.2} $$

where η is understood to be infinitesimal. (4.2) reads as a continued fraction [67] and can be calculated by a recursion method based on the Lanczos diagonalization algorithm [68, 69].

In terms of the bosonic language, the Raman operator is expressed by the magnons as (3.25). We define the $2l$-magnon-mediated Raman intensities at absolute zero as

$$ {}^{[p]}I_{2l\mathrm{M}}(\omega) = \int_{-\infty}^{\infty} \frac{dt\, e^{i\omega t}}{2\pi\hbar L} \sum_{n,n'=1}^{p/2} \langle 0|{}^{[2n]}\mathcal{R}^{\dagger}_{2l\mathrm{M}}(t)\, {}^{[2n']}\mathcal{R}_{2l\mathrm{M}}|0\rangle. \tag{4.3} $$

Since in this calculation, we take the magnon-number-conserving interactions to be the relevant terms, $\langle 0|{}^{[2n]}\mathcal{R}^{\dagger}_{2l\mathrm{M}}(t)\, {}^{[2n']}\mathcal{R}_{2l'\mathrm{M}}|0\rangle = 0$ unless $l = l'$ not only for the unperturbed ground state $|0\rangle = |0\rangle_{\mathrm{BL}}$ but also for any ground state $|0\rangle$ corrected by the quartic normal-ordered interaction $:\mathcal{H}^{(0)}:$ perturbatively or variationally. Then the total scattering intensity may be approximated by

$$ {}^{[p]}I(\omega) = \sum_{l=1}^{2} {}^{[p]}I_{2l\mathrm{M}}(\omega). \tag{4.4} $$

4.2 Irreducible Decomposition

The two-dimensional Raman operator is written as a rank-2 tensor dotted with the polarization vectors of the incident ($\boldsymbol{e}_{\rm in}$) and scattered ($\boldsymbol{e}_{\rm sc}$) photons [37, 70],

$$ {}^{[p]}\mathcal{R} = \sum_{\mu,\nu=x,y} e_{\rm in}^{\mu}\, {}^{[p]}\mathcal{R}^{\mu\nu} e_{\rm sc}^{\nu\,*}, \tag{4.5} $$

where $\boldsymbol{e}_{\rm in} \equiv (e_{\rm in}^x, e_{\rm in}^y, 0)$ and $\boldsymbol{e}_{\rm sc} \equiv (e_{\rm sc}^x, e_{\rm sc}^y, 0)$ are the unit vectors indicating the polarizations of incident and scattered photons, respectively, while ${}^{[p]}\mathcal{R}^{\mu\nu}$ is the (μ,ν)-element of ${}^{[p]}\mathcal{R}$ in Cartesian coordinates. We introduce four matrices

$$ \boldsymbol{\Xi}_0 \equiv \begin{bmatrix} 1 & 0 \\ 0 & 1 \end{bmatrix},\ \boldsymbol{\Xi}_1 \equiv \begin{bmatrix} 0 & 1 \\ 1 & 0 \end{bmatrix},\ \boldsymbol{\Xi}_2 \equiv \begin{bmatrix} 0 & 1 \\ -1 & 0 \end{bmatrix},\ \boldsymbol{\Xi}_3 \equiv \begin{bmatrix} 1 & 0 \\ 0 & -1 \end{bmatrix}, \tag{4.6} $$

with their Hilbert-Schmidt inner products satisfying

$$ {\rm Tr}\left[{}^{\rm t}\boldsymbol{\Xi}_i \boldsymbol{\Xi}_j\right] = \sum_{\mu,\nu=x,y} \Xi_i^{\mu\nu}\Xi_j^{\mu\nu} = 2\delta_{i,j} \tag{4.7} $$

to decompose a 2×2 matrix. We rewrite the Raman operator (4.5) into

$$ {}^{[p]}\mathcal{R} = \sum_{i=0}^{3} E_{\boldsymbol{\Xi}_i}\, {}^{[p]}\mathcal{R}_{\boldsymbol{\Xi}_i},\ E_{\boldsymbol{\Xi}_i} \equiv \sum_{\mu,\nu=x,y} e_{\rm in}^{\mu}\Xi_i^{\mu\nu} e_{\rm sc}^{\nu\,*}; \tag{4.8} $$

$$ \begin{aligned} &E_{\boldsymbol{\Xi}_0} = e_{\rm in}^x e_{\rm sc}^{x\,*} + e_{\rm in}^y e_{\rm sc}^{y\,*},\ E_{\boldsymbol{\Xi}_1} = e_{\rm in}^x e_{\rm sc}^{y\,*} + e_{\rm in}^y e_{\rm sc}^{x\,*}, \\ &E_{\boldsymbol{\Xi}_2} = e_{\rm in}^x e_{\rm sc}^{y\,*} - e_{\rm in}^y e_{\rm sc}^{x\,*},\ E_{\boldsymbol{\Xi}_3} = e_{\rm in}^x e_{\rm sc}^{x\,*} - e_{\rm in}^y e_{\rm sc}^{y\,*}, \end{aligned} \tag{4.8a} $$

$$ \begin{aligned} &{}^{[p]}\mathcal{R}_{\boldsymbol{\Xi}_0} = \frac{{}^{[p]}\mathcal{R}^{xx} + {}^{[p]}\mathcal{R}^{yy}}{2},\ {}^{[p]}\mathcal{R}_{\boldsymbol{\Xi}_1} = \frac{{}^{[p]}\mathcal{R}^{xy} + {}^{[p]}\mathcal{R}^{yx}}{2}, \\ &{}^{[p]}\mathcal{R}_{\boldsymbol{\Xi}_2} = \frac{{}^{[p]}\mathcal{R}^{xy} - {}^{[p]}\mathcal{R}^{yx}}{2},\ {}^{[p]}\mathcal{R}_{\boldsymbol{\Xi}_3} = \frac{{}^{[p]}\mathcal{R}^{xx} - {}^{[p]}\mathcal{R}^{yy}}{2}. \end{aligned} \tag{4.8b} $$

Now we consider two-dimensional lattices of $\mathbf{C}_{n\rm v}$ point symmetry in general and recall the irreducible decomposition of the Raman operator for an arbitrary point symmetry group $\mathbf{P}$,

$$ {}^{[p]}\mathcal{R} = {\sum_{i}}' \sum_{\mu=1}^{d^{\mathbf{P}}_{\Xi_i}} E^{\mathbf{P}}_{\Xi_i:\mu}\, {}^{[p]}\mathcal{R}^{\mathbf{P}}_{\Xi_i:\mu}, \tag{4.9} $$

where $\sum_i'$ runs over the Raman-active irreducible representations Ξ_i of $\mathbf{P}$, each with dimensionality $d^{\mathbf{P}}_{\Xi_i}$, and $E^{\mathbf{P}}_{\Xi_i:\mu}$ and $\mathcal{R}^{\mathbf{P}}_{\Xi_i:\mu}$ are the μth polarization-vector basis function and Raman vertex for Ξ_i, respectively. For instance, putting $\mathbf{P} = \mathbf{C}_{5\rm v}$ or $\mathbf{P} = \mathbf{C}_{8\rm v}$, the irreducible decomposition of the Raman operator (4.9) contains two one-dimensional irreducible representations $\rm A_1$ and $\rm A_2$, and one two-dimensional irreducible representation $\rm E_2$. The polarization-vector basis functions and symmetry-definite Raman vertices are given by

$$ \begin{aligned} E^{\mathbf{C}_{5\rm v}}_{\rm A_1:1} &= E^{\mathbf{C}_{8\rm v}}_{\rm A_1:1} = e_{\rm in}^x e_{\rm sc}^{x\,*} + e_{\rm in}^y e_{\rm sc}^{y\,*}, \\ E^{\mathbf{C}_{5\rm v}}_{\rm E_2:1} &= E^{\mathbf{C}_{8\rm v}}_{\rm E_2:1} = e_{\rm in}^x e_{\rm sc}^{y\,*} + e_{\rm in}^y e_{\rm sc}^{x\,*}, \\ E^{\mathbf{C}_{5\rm v}}_{\rm A_2:1} &= E^{\mathbf{C}_{8\rm v}}_{\rm A_2:1} = e_{\rm in}^x e_{\rm sc}^{y\,*} - e_{\rm in}^y e_{\rm sc}^{x\,*}, \\ E^{\mathbf{C}_{5\rm v}}_{\rm E_2:2} &= E^{\mathbf{C}_{8\rm v}}_{\rm E_2:2} = e_{\rm in}^x e_{\rm sc}^{x\,*} - e_{\rm in}^y e_{\rm sc}^{y\,*}, \end{aligned} \tag{4.10a} $$

Table 4.1: Correspondence between irreducible representations of the point symmetry groups $\mathbf{P} = \mathbf{C}_{n\mathrm{v}}$ and the basis matrices $\mathbf{\Xi}_i$. The irreducible representations which are doubly underlined when they are Raman-active symmetry species within the Loudon-Fleury second-order perturbation scheme, while they are singly underlined when it is not until we employ the Shastry-Shraiman fourth-order perturbation scheme that they become Raman-active symmetry species, where we specify a particular lattice to the point symmetry groups each, because it depends on the lattice shape which symmetry species is Raman active. In the case of $\mathbf{P} = \mathbf{C}_{2\mathrm{v}}$, not only $\mathbf{\Xi}_0$ but also $\mathbf{\Xi}_3$ may belong to the A_1 symmetry species and the coefficients of their linear combination depend on further details of the lattice structure.

$\mathbf{P}$	$\mathbf{\Xi}_0$	$\mathbf{\Xi}_1$	$\mathbf{\Xi}_2$	$\mathbf{\Xi}_3$
$\mathbf{C}_{2\mathrm{v}}$ (ladder)	$\underline{\underline{\mathrm{A}_1 : 1}}$	$\mathrm{A}_2 : 1$	$\mathrm{A}_2 : 1$	$\underline{\underline{\mathrm{A}_1 : 1}}$
$\mathbf{C}_{3\mathrm{v}}$ (kagome)	$\underline{\mathrm{A}_1 : 1}$	$\underline{\underline{\mathrm{E} : 1}}$	$\underline{\mathrm{A}_2 : 1}$	$\underline{\underline{\mathrm{E} : 2}}$
$\mathbf{C}_{4\mathrm{v}}$ (square)	$\underline{\mathrm{A}_1 : 1}$	$\mathrm{B}_2 : 1$	$\mathrm{A}_2 : 1$	$\underline{\underline{\mathrm{B}_1 : 1}}$
$\mathbf{C}_{6\mathrm{v}}$ (triangular)	$\underline{\mathrm{A}_1 : 1}$	$\underline{\underline{\mathrm{E}_2 : 1}}$	$\mathrm{A}_2 : 1$	$\underline{\underline{\mathrm{E}_2 : 2}}$
$\mathbf{C}_{6\mathrm{v}}$ (honeycomb)	$\underline{\mathrm{A}_1 : 1}$	$\underline{\underline{\mathrm{E}_2 : 1}}$	$\underline{\mathrm{A}_2 : 1}$	$\underline{\underline{\mathrm{E}_2 : 2}}$
$\mathbf{C}_{5\mathrm{v}}$ (Penrose)	$\underline{\mathrm{A}_1 : 1}$	$\underline{\underline{\mathrm{E}_2 : 1}}$	$\underline{\mathrm{A}_2 : 1}$	$\underline{\underline{\mathrm{E}_2 : 2}}$
$\mathbf{C}_{8\mathrm{v}}$ (Ammann-Beenker)	$\underline{\mathrm{A}_1 : 1}$	$\underline{\underline{\mathrm{E}_2 : 1}}$	$\underline{\mathrm{A}_2 : 1}$	$\underline{\underline{\mathrm{E}_2 : 2}}$

$$
\begin{aligned}
{}^{[p]}\mathcal{R}^{\mathbf{C}_{5\mathrm{v}}}_{\mathrm{A}_1:1} &= {}^{[p]}\mathcal{R}^{\mathbf{C}_{8\mathrm{v}}}_{\mathrm{A}_1:1} = \frac{{}^{[p]}\mathcal{R}^{xx} + {}^{[p]}\mathcal{R}^{yy}}{2}, \\
{}^{[p]}\mathcal{R}^{\mathbf{C}_{5\mathrm{v}}}_{\mathrm{E}_2:1} &= {}^{[p]}\mathcal{R}^{\mathbf{C}_{8\mathrm{v}}}_{\mathrm{E}_2:1} = \frac{{}^{[p]}\mathcal{R}^{xy} + {}^{[p]}\mathcal{R}^{yx}}{2}, \\
{}^{[p]}\mathcal{R}^{\mathbf{C}_{5\mathrm{v}}}_{\mathrm{A}_2:1} &= {}^{[p]}\mathcal{R}^{\mathbf{C}_{8\mathrm{v}}}_{\mathrm{A}_2:1} = \frac{{}^{[p]}\mathcal{R}^{xy} - {}^{[p]}\mathcal{R}^{yx}}{2}, \\
{}^{[p]}\mathcal{R}^{\mathbf{C}_{5\mathrm{v}}}_{\mathrm{E}_2:2} &= {}^{[p]}\mathcal{R}^{\mathbf{C}_{8\mathrm{v}}}_{\mathrm{E}_2:2} = \frac{{}^{[p]}\mathcal{R}^{xx} - {}^{[p]}\mathcal{R}^{yy}}{2}.
\end{aligned}
\tag{4.10b}
$$

The polarization-vector basis functions $E^{\mathbf{C}_{n\mathrm{v}}}_{\Xi_i:\mu}$ relevant to Raman scattering have their equivalent in $E_{\mathbf{\Xi}_i}$'s. [cf. (4.8a) and (4.10a)]. We list their correspondence relations in Table 4.1.

Since the ground state $|0\rangle$ is invariant under every symmetry operation of $\mathbf{P}$, any expectation value between Raman vertices of different symmetry species for it goes to zero $\langle 0|{}^{[2n]}\mathcal{R}^{\mathbf{P}\,\dagger}_{\Xi_i:\mu}(t)\,{}^{[2n']}\mathcal{R}^{\mathbf{P}}_{\Xi_{i'}:\mu'}|0\rangle = \delta_{i,i'}\delta_{\mu,\mu'}\langle 0|{}^{[2n]}\mathcal{R}^{\mathbf{P}\,\dagger}_{\Xi_i:\mu}(t)\,{}^{[2n']}\mathcal{R}^{\mathbf{P}}_{\Xi_i:\mu}|0\rangle$ [70, 71, 72, 73]. We can therefore classify the Raman intensities as to symmetry species,

$$
{}^{[p]}I^{\mathbf{P}}_{\Xi_i:\mu}(\omega) = \int_{-\infty}^{\infty} \frac{dt\, e^{i\omega t}}{2\pi\hbar L} \sum_{n,n'=1}^{p/2} \langle 0|{}^{[2n]}\mathcal{R}^{\mathbf{P}\,\dagger}_{\Xi_i:\mu}(t)\,{}^{[2n']}\mathcal{R}^{\mathbf{P}}_{\Xi_i:\mu}|0\rangle. \tag{4.11}
$$

Considering that ${}^{[p]}I^{\mathbf{P}}_{\Xi_i:1}(\omega) = {}^{[p]}I^{\mathbf{P}}_{\Xi_i:\mu}(\omega)$ $(\mu = 2, \cdots, d^{\mathbf{P}}_{\Xi_i})$ for any multidimensional representation Ξ_i [70, 71], we find

$$
{}^{[p]}I(\omega) = {\sum_i}' {}^{[p]}I^{\mathbf{P}}_{\Xi_i:1}(\omega) \sum_{\mu=1}^{d^{\mathbf{P}}_{\Xi_i}} \left|E^{\mathbf{P}}_{\Xi_i:\mu}\right|^2. \tag{4.12}
$$

4.3 Green's Function Formalism

Magnon-magnon interactions significantly modify the Raman spectra [34, 35, 36, 37]. Then we take account of the two-body interactions $:\mathcal{H}^{(0)}:$ in two ways, i.e., Green's function (GF) perturbative and configuration-interaction (CI) variational approaches. First we demonstrate a renormalized perturbation theory. Putting the time-dependent magnon operator in the Heisenberg picture $\alpha(t) \equiv e^{i\mathcal{H}t/\hbar}\alpha e^{-i\mathcal{H}t/\hbar}$, we introduce the one-, two-, three-, and four-magnon GFs for the corrected ground state $|0\rangle$,

$$G^{k_\tau}_{l_\sigma}(t) \equiv -i\langle 0|\mathcal{T}\alpha^{\tau}_{k_\tau}(t)\alpha^{\sigma\dagger}_{l_\sigma}|0\rangle, \tag{4.13a}$$

$$G^{k_\sigma k'_{\sigma'}}_{l_\sigma l'_{\sigma'}}(t) \equiv -i\langle 0|\mathcal{T}\alpha^{\sigma}_{k_\sigma}(t)\alpha^{\sigma'}_{k'_{\sigma'}}(t)\alpha^{\sigma\dagger}_{l_\sigma}\alpha^{\sigma'\dagger}_{l'_{\sigma'}}|0\rangle, \tag{4.13b}$$

$$G^{k_\sigma k'_\sigma k''_{\bar\sigma}}_{l_\sigma l'_\sigma l''_{\bar\sigma}}(t) \equiv -i\langle 0|\mathcal{T}\alpha^{\sigma}_{k_\sigma}(t)\alpha^{\sigma}_{k'_\sigma}(t)\alpha^{\bar\sigma}_{k''_{\bar\sigma}}(t)\alpha^{\sigma\dagger}_{l_\sigma}\alpha^{\sigma\dagger}_{l'_\sigma}\alpha^{\bar\sigma\dagger}_{l''_{\bar\sigma}}|0\rangle, \tag{4.13c}$$

$$G^{k_\sigma k'_\sigma k''_{\bar\sigma} k'''_{\bar\sigma}}_{l_\sigma l'_\sigma l''_{\bar\sigma} l'''_{\bar\sigma}}(t) \equiv -i\langle 0|\mathcal{T}\alpha^{\sigma}_{k_\sigma}(t)\alpha^{\sigma}_{k'_\sigma}(t)\alpha^{\bar\sigma}_{k''_{\bar\sigma}}(t)\alpha^{\bar\sigma}_{k'''_{\bar\sigma}}(t)\alpha^{\sigma\dagger}_{l_\sigma}\alpha^{\sigma\dagger}_{l'_\sigma}\alpha^{\bar\sigma\dagger}_{l''_{\bar\sigma}}\alpha^{\bar\sigma\dagger}_{l'''_{\bar\sigma}}|0\rangle, \tag{4.13d}$$

and define their Fourier transforms as

$$G^{k_\tau}_{l_\sigma}(\omega) \equiv \int_{-\infty}^{\infty} dt\, e^{i\omega t} G^{k_\tau}_{l_\sigma}(t), \tag{4.14a}$$

$$G^{k_\sigma k'_{\sigma'}}_{l_\sigma l'_{\sigma'}}(\omega) \equiv \int_{-\infty}^{\infty} dt\, e^{i\omega t} G^{k_\sigma k'_{\sigma'}}_{l_\sigma l'_{\sigma'}}(t), \tag{4.14b}$$

$$G^{k_\sigma k'_\sigma k''_{\bar\sigma}}_{l_\sigma l'_\sigma l''_{\bar\sigma}}(\omega) \equiv \int_{-\infty}^{\infty} dt\, e^{i\omega t} G^{k_\sigma k'_\sigma k''_{\bar\sigma}}_{l_\sigma l'_\sigma l''_{\bar\sigma}}(t), \tag{4.14c}$$

$$G^{k_\sigma k'_\sigma k''_{\bar\sigma} k'''_{\bar\sigma}}_{l_\sigma l'_\sigma l''_{\bar\sigma} l'''_{\bar\sigma}}(\omega) \equiv \int_{-\infty}^{\infty} dt\, e^{i\omega t} G^{k_\sigma k'_\sigma k''_{\bar\sigma} k'''_{\bar\sigma}}_{l_\sigma l'_\sigma l''_{\bar\sigma} l'''_{\bar\sigma}}(t), \tag{4.14d}$$

where $\sigma(\equiv -\bar\sigma)$, σ', and τ take $\pm$ and $\mathcal{T}$ denotes the time-ordering operator with respect to the unperturbed magnon operators emergent in (3.20). The $2l(l = 1, 2)$-magnon-mediated Raman scattering intensities are calculated as

$$\begin{aligned}
&{}^{[p]}I_{2l\mathrm{M}}(\omega) = -\mathrm{Im}\int_{-\infty}^{\infty}\frac{dt\, e^{i\omega t}}{i\pi\hbar L}\sum_{n,n'=1}^{p/2}\langle 0|\mathcal{T}\,{}^{[2n]}\mathcal{R}^{\dagger}_{2l\mathrm{M}}(t)\,{}^{[2n']}\mathcal{R}_{2l\mathrm{M}}|0\rangle \equiv -\mathrm{Im}\int_{-\infty}^{\infty}\frac{dt\, e^{i\omega t}}{\pi\hbar L}{}^{[p]}\mathcal{G}_{2l\mathrm{M}}(t);\\
&{}^{[p]}\mathcal{G}_{2\mathrm{M}}(t) = \sum_{k_+,k'_-}\sum_{l_+,l'_-}{}^{[p]}W^{(2)*}_{k_+k'_-}\, G^{k_+k'_-}_{l_+l'_-}(t)\,{}^{[p]}W^{(2)}_{l_+l'_-},\\
&{}^{[p]}\mathcal{G}_{4\mathrm{M}}(t) = \sum_{k_+,k'_+,k''_-,k'''_-}\sum_{l_+,l'_+,l''_-,l'''_-}{}^{[p]}X^{(7)*}_{k_+k'_+k''_-k'''_-}\, G^{k_+k'_+k''_-k'''_-}_{l_+l'_+l''_-l'''_-}(t)\,{}^{[p]}X^{(7)}_{l_+l'_+l''_-l'''_-},
\end{aligned} \tag{4.15}$$

where we numerically obtain the coefficients ${}^{[p]}W^{(2)}_{l_+l'_-}$ and ${}^{[p]}X^{(7)}_{l_+l'_+l''_-l'''_-}$ as

Since any perturbative renormalization is hardly tractable for more-than-three-magnon GFs, we decompose them into less-than-four-magnon GFs [74]. The four-magnon GFs can be approximated by the two-magnon GFs on one hand,

$$\begin{aligned}
2iG^{k_+k'_+k''_-k'''_-}_{l_+l'_+l''_-l'''_-}(t) &= 2\langle 0|\mathcal{T}\alpha^{+}_{k_+}(t)\alpha^{+}_{k'_+}(t)\alpha^{-}_{k''_-}(t)\alpha^{-}_{k'''_-}(t)\alpha^{+\dagger}_{l_+}\alpha^{+\dagger}_{l'_+}\alpha^{-\dagger}_{l''_-}\alpha^{-\dagger}_{l'''_-}|0\rangle\\
&\simeq \langle 0|\mathcal{T}\alpha^{+}_{k_+}(t)\alpha^{-}_{k''_-}(t)\alpha^{+\dagger}_{l_+}\alpha^{-\dagger}_{l''_-}|0\rangle\langle 0|\mathcal{T}\alpha^{+}_{k'_+}(t)\alpha^{-}_{k'''_-}(t)\alpha^{+\dagger}_{l'_+}\alpha^{-\dagger}_{l'''_-}|0\rangle\\
&\quad + \langle 0|\mathcal{T}\alpha^{+}_{k_+}(t)\alpha^{-}_{k''_-}(t)\alpha^{+\dagger}_{l_+}\alpha^{-\dagger}_{l'''_-}|0\rangle\langle 0|\mathcal{T}\alpha^{+}_{k'_+}(t)\alpha^{-}_{k'''_-}(t)\alpha^{+\dagger}_{l'_+}\alpha^{-\dagger}_{l''_-}|0\rangle
\end{aligned}$$

$$
\begin{aligned}
&+\langle 0|\mathcal{T}\alpha^{+}_{k_+}(t)\alpha^{-}_{k''_-}(t)\alpha^{+\dagger}_{l'_+}\alpha^{-\dagger}_{l''_-}|0\rangle\langle 0|\mathcal{T}\alpha^{+}_{k'_+}(t)\alpha^{-}_{k'''_-}(t)\alpha^{+\dagger}_{l_+}\alpha^{-\dagger}_{l'''_-}|0\rangle\\
&+\langle 0|\mathcal{T}\alpha^{+}_{k_+}(t)\alpha^{-}_{k''_-}(t)\alpha^{+\dagger}_{l'_+}\alpha^{-\dagger}_{l'''_-}|0\rangle\langle 0|\mathcal{T}\alpha^{+}_{k'_+}(t)\alpha^{-}_{k'''_-}(t)\alpha^{+\dagger}_{l_+}\alpha^{-\dagger}_{l''_-}|0\rangle\\
&+\langle 0|\mathcal{T}\alpha^{+}_{k_+}(t)\alpha^{+}_{k'_+}(t)\alpha^{+\dagger}_{l_+}\alpha^{+\dagger}_{l'_+}|0\rangle\langle 0|\mathcal{T}\alpha^{-}_{k''_-}(t)\alpha^{-}_{k'''_-}(t)\alpha^{-\dagger}_{l''_-}\alpha^{-\dagger}_{l'''_-}|0\rangle, \qquad (4.16)
\end{aligned}
$$

and by the three- and one-magnon GFs on the other hand,

$$
\begin{aligned}
4iG^{k_+k'_+k''_-k'''_-}_{l_+l'_+l''_-l'''_-}(t) &= 4\langle 0|\mathcal{T}\alpha^{+}_{k_+}(t)\alpha^{+}_{k'_+}(t)\alpha^{-}_{k''_-}(t)\alpha^{-}_{k'''_-}(t)\alpha^{+\dagger}_{l_+}\alpha^{+\dagger}_{l'_+}\alpha^{-\dagger}_{l''_-}\alpha^{-\dagger}_{l'''_-}|0\rangle\\
&\simeq \langle 0|\mathcal{T}\alpha^{+}_{k_+}(t)\alpha^{+\dagger}_{l_+}|0\rangle\langle 0|\mathcal{T}\alpha^{+}_{k'_+}(t)\alpha^{-}_{k''_-}(t)\alpha^{-}_{k'''_-}(t)\alpha^{+\dagger}_{l'_+}\alpha^{-\dagger}_{l''_-}\alpha^{-\dagger}_{l'''_-}|0\rangle\\
&\quad+\langle 0|\mathcal{T}\alpha^{+}_{k_+}(t)\alpha^{+\dagger}_{l'_+}|0\rangle\langle 0|\mathcal{T}\alpha^{+}_{k'_+}(t)\alpha^{-}_{k''_-}(t)\alpha^{-}_{k'''_-}(t)\alpha^{+\dagger}_{l_+}\alpha^{-\dagger}_{l''_-}\alpha^{-\dagger}_{l'''_-}|0\rangle\\
&\quad+\langle 0|\mathcal{T}\alpha^{+}_{k'_+}(t)\alpha^{+\dagger}_{l_+}|0\rangle\langle 0|\mathcal{T}\alpha^{+}_{k_+}(t)\alpha^{-}_{k''_-}(t)\alpha^{-}_{k'''_-}(t)\alpha^{+\dagger}_{l'_+}\alpha^{-\dagger}_{l''_-}\alpha^{-\dagger}_{l'''_-}|0\rangle\\
&\quad+\langle 0|\mathcal{T}\alpha^{+}_{k'_+}(t)\alpha^{+\dagger}_{l'_+}|0\rangle\langle 0|\mathcal{T}\alpha^{+}_{k_+}(t)\alpha^{-}_{k''_-}(t)\alpha^{-}_{k'''_-}(t)\alpha^{+\dagger}_{l_+}\alpha^{-\dagger}_{l''_-}\alpha^{-\dagger}_{l'''_-}|0\rangle\\
&\quad+\langle 0|\mathcal{T}\alpha^{-}_{k''_-}(t)\alpha^{-\dagger}_{l''_-}|0\rangle\langle 0|\mathcal{T}\alpha^{+}_{k_+}(t)\alpha^{+}_{k'_+}(t)\alpha^{-}_{k'''_-}(t)\alpha^{+\dagger}_{l_+}\alpha^{+\dagger}_{l'_+}\alpha^{-\dagger}_{l'''_-}|0\rangle\\
&\quad+\langle 0|\mathcal{T}\alpha^{-}_{k''_-}(t)\alpha^{-\dagger}_{l'''_-}|0\rangle\langle 0|\mathcal{T}\alpha^{+}_{k_+}(t)\alpha^{+}_{k'_+}(t)\alpha^{-}_{k'''_-}(t)\alpha^{+\dagger}_{l_+}\alpha^{+\dagger}_{l'_+}\alpha^{-\dagger}_{l''_-}|0\rangle\\
&\quad+\langle 0|\mathcal{T}\alpha^{-}_{k'''_-}(t)\alpha^{-\dagger}_{l''_-}|0\rangle\langle 0|\mathcal{T}\alpha^{+}_{k_+}(t)\alpha^{+}_{k'_+}(t)\alpha^{-}_{k''_-}(t)\alpha^{+\dagger}_{l_+}\alpha^{+\dagger}_{l'_+}\alpha^{-\dagger}_{l'''_-}|0\rangle\\
&\quad+\langle 0|\mathcal{T}\alpha^{-}_{k'''_-}(t)\alpha^{-\dagger}_{l'''_-}|0\rangle\langle 0|\mathcal{T}\alpha^{+}_{k_+}(t)\alpha^{+}_{k'_+}(t)\alpha^{-}_{k''_-}(t)\alpha^{+\dagger}_{l_+}\alpha^{+\dagger}_{l'_+}\alpha^{-\dagger}_{l''_-}|0\rangle. \qquad (4.17)
\end{aligned}
$$

Since the coefficient of the Raman correlation function ${}^{[p]}X^{(7)}_{l_+l'_+l''_-l'''_-}$ is symmetric with respect to the replacements $l_+ \leftrightarrow l'_+$ and $l''_- \leftrightarrow l'''_-$, the four-magnon GFs can be expressed as

$$
\begin{aligned}
G^{k_+k'_+k''_-k'''_-}_{l_+l'_+l''_-l'''_-}(t) &\simeq 2iG^{k_+k''_-}_{l_+l''_-}(t)G^{k'_+k'''_-}_{l'_+l'''_-}(t)+\frac{i}{2}G^{k_+k'_+}_{l_+l'_+}(t)G^{k''_-k'''_-}_{l''_-l'''_-}(t), \qquad (4.18)\\
G^{k_+k'_+k''_-k'''_-}_{l_+l'_+l''_-l'''_-}(t) &\simeq iG^{k_+k'_+k''_-}_{l_+l'_+l''_-}(t)G^{k'''_-}_{l'''_-}(t)+iG^{k''_-k'''_-k_+}_{l''_-l'''_-l_+}(t)G^{k'_+}_{l'_+}(t), \qquad (4.19)
\end{aligned}
$$

and their Fourier transforms are given by

$$
\begin{aligned}
G^{k_+k'_+k''_-k'''_-}_{l_+l'_+l''_-l'''_-}(\omega) &\simeq i\int_{-\infty}^{\infty}dt\,e^{i\omega t}\left[2G^{k_+k''_-}_{l_+l''_-}(t)G^{k'_+k'''_-}_{l'_+l'''_-}(t)+\frac{1}{2}G^{k_+k'_+}_{l_+l'_+}(t)G^{k''_-k'''_-}_{l''_-l'''_-}(t)\right]\\
&= i\int_{-\infty}^{\infty}\frac{ds}{2\pi}\left[2G^{k_+k''_-}_{l_+l''_-}(s)G^{k'_+k'''_-}_{l'_+l'''_-}(\omega-s)+\frac{1}{2}G^{k_+k'_+}_{l_+l'_+}(s)G^{k''_-k'''_-}_{l''_-l'''_-}(\omega-s)\right], \qquad (4.20)\\
G^{k_+k'_+k''_-k'''_-}_{l_+l'_+l''_-l'''_-}(\omega) &\simeq i\int_{-\infty}^{\infty}dt\,e^{i\omega t}\left[G^{k_+k'_+k''_-}_{l_+l'_+l''_-}(t)G^{k'''_-}_{l'''_-}(t)+G^{k''_-k'''_-k_+}_{l''_-l'''_-l_+}(t)G^{k'_+}_{l'_+}(t)\right]\\
&= i\int_{-\infty}^{\infty}\frac{ds}{2\pi}\left[G^{k_+k'_+k''_-}_{l_+l'_+l''_-}(s)G^{k'''_-}_{l'''_-}(\omega-s)+G^{k''_-k'''_-k_+}_{l''_-l'''_-l_+}(s)G^{k'_+}_{l'_+}(\omega-s)\right]. \qquad (4.21)
\end{aligned}
$$

$\mathcal{H}_{\rm BL}$ is nothing but the $O(S^0)$ Hartree-Fock Hamiltonian and the residual $O(S^0)$ interaction : $\mathcal{H}^{(0)}$: has no effect on the one-magnon GFs, i.e., $\langle 0|\mathcal{T}\alpha^{\tau}_{k_\tau}(t)\alpha^{\sigma\dagger}_{l_\sigma}|0\rangle = {}_{\rm BL}\langle 0|\mathcal{T}\alpha^{\tau}_{k_\tau}(t)_{\rm BL}\alpha^{\sigma\dagger}_{l_\sigma}|0\rangle_{\rm BL} \equiv iG^{k_\tau}_{l_\sigma}(t)_{\rm BL}$ with the time-dependent magnon operator of the interaction picture $\alpha(t)_{\rm BL} \equiv e^{i\mathcal{H}_{\rm BL}t/\hbar}\alpha e^{-i\mathcal{H}_{\rm BL}t/\hbar}$. Then the Dyson equation for the one-magnon GFs reduces to

$$
G^{k_\tau}_{l_\sigma}(\omega) = G^{k_\tau}_{l_\sigma}(\omega)_{\rm BL} = \frac{\hbar\delta_{k_\tau,l_\sigma}}{\hbar\omega-\varepsilon^{\sigma}_{l_\sigma}+i\eta}, \qquad (4.22)
$$

Next we consider the ladder-approximation Bethe-Salpeter equations for the two-magnon GFs

$$G^{k_+k'_-}_{l_+l'_-}(\omega) = G^{k_+k'_-}_{l_+l'_-}(\omega)_{\rm BL} - \frac{J}{\hbar}\sum_{p_+,p'_-}\sum_{q_+,q'_-} G^{k_+k'_-}_{p_+p'_-}(\omega)_{\rm BL}\sum_{i\in{\rm A}}\sum_{j\in{\rm B}} l_{i,j}V^{(4)}_{ij;p_+q_+p'_-q'_-}G^{q_+q'_-}_{l_+l'_-}(\omega), \tag{4.23a}$$

$$G^{k_+k'_+}_{l_+l'_+}(\omega) = G^{k_+k'_+}_{l_+l_{+'}}(\omega)_{\rm BL} - \frac{J}{\hbar}\sum_{p_+,p'_+}\sum_{q_+,q'_+} G^{k_+k'_+}_{p_+p'_+}(\omega)_{\rm BL}\sum_{i\in{\rm A}}\sum_{j\in{\rm B}} l_{i,j}V^{(9)}_{ij;p_+p'_+q_+q'_+}G^{q_+q'_+}_{l_+l'_+}(\omega), \tag{4.23b}$$

$$G^{k_-k'_-}_{l_-l'_-}(\omega) = G^{k_-k'_-}_{l_-l'_-}(\omega)_{\rm BL} - \frac{J}{\hbar}\sum_{p_-,p'_-}\sum_{q_-,q'_-} G^{k_-k'_-}_{p_-p'_-}(\omega)_{\rm BL}\sum_{i\in{\rm A}}\sum_{j\in{\rm B}} l_{i,j}V^{(1)}_{ij;p_-p'_-q_-q'_-}G^{q_-q'_-}_{l_-l'_-}(\omega), \tag{4.23c}$$

denoting the unperturbed two-magnon GFs by

$$\begin{aligned} G^{k_\sigma k'_{\sigma'}}_{l_\sigma l'_{\sigma'}}(\omega)_{\rm BL} &\equiv -i\int_{-\infty}^{\infty} dt\, e^{i\omega t}{}_{\rm BL}\langle 0|\mathcal{T}\alpha^{\sigma}_{k_\sigma}(t)_{\rm BL}\alpha^{\sigma'}_{k'_{\sigma'}}(t)_{\rm BL}\alpha^{\sigma\dagger}_{l_\sigma}\alpha^{\sigma'\dagger}_{l'_{\sigma'}}|0\rangle_{\rm BL} \\ &= i\int_{-\infty}^{\infty} dt\, e^{i\omega t}\left[G^{k_\sigma}_{l_\sigma}(t)_{\rm BL}G^{k'_{\sigma'}}_{l'_{\sigma'}}(t)_{\rm BL} + G^{k_\sigma}_{l'_{\sigma'}}(t)_{\rm BL}G^{k'_{\sigma'}}_{l_\sigma}(t)_{\rm BL}\right] \\ &= \frac{\hbar(\delta_{k_\sigma,l_\sigma}\delta_{k'_{\sigma'},l'_{\sigma'}} + \delta_{k_\sigma,l'_{\sigma'}}\delta_{k'_{\sigma'},l_\sigma})}{\hbar\omega - \varepsilon^{\sigma}_{l_\sigma} - \varepsilon^{\sigma'}_{l'_{\sigma'}} + i\eta}. \end{aligned} \tag{4.24}$$

We solve the eigenequations obtained from (4.23a)–(4.23c),

$$\mathcal{V}^{\sigma\sigma'}\boldsymbol{g}^{\sigma\sigma'}_{\lambda} = \hbar\Omega^{\sigma\sigma'}_{\lambda}\boldsymbol{g}^{\sigma\sigma'}_{\lambda}, \tag{4.25}$$

where $\boldsymbol{g}^{\sigma\sigma'}_{\lambda}$ are the column vectors of dimension $L_\sigma L_{\sigma'}$ whose $[(k'_{\sigma'}-1)L_\sigma + k_\sigma]$-elements are given by

$$\left[\boldsymbol{g}^{\sigma\sigma'}_{\lambda}\right]_{(k'_{\sigma'}-1)L_\sigma+k_\sigma} \equiv g^{k_\sigma k'_{\sigma'}}_{\lambda} \equiv \langle 0|\alpha^{\sigma}_{k_\sigma}\alpha^{\sigma'}_{k'_{\sigma'}}|\lambda\rangle, \tag{4.26}$$

whereas $\mathcal{V}^{\sigma\sigma'}$ are the matrices of dimension $L_\sigma L_{\sigma'}\times L_\sigma L_{\sigma'}$ whose $[(k'_{\sigma'}-1)L_\sigma + k_\sigma, (l'_{\sigma'}-1)L_\sigma + l_\sigma]$-elements are given by

$$\begin{aligned} &\left[\mathcal{V}^{+-}\right]_{(k'_--1)L_++k_+,(l'_--1)L_++l_+} \\ &\quad = \delta_{k_+,l_+}\delta_{k'_-,l'_-}\left(\varepsilon^{+}_{l_+} + \varepsilon^{-}_{l'_-}\right) - J\sum_{i\in{\rm A}}\sum_{j\in{\rm B}} l_{i,j}V^{(4)}_{ij;k_+l_+k'_-l'_-}, \end{aligned} \tag{4.27a}$$

$$\begin{aligned} &\left[\mathcal{V}^{++}\right]_{(k'_+-1)L_++k_+,(l'_+-1)L_++l_+} \\ &\quad = \delta_{k_+,l_+}\delta_{k'_+,l'_+}\left(\varepsilon^{+}_{l_+} + \varepsilon^{+}_{l'_+}\right) - 2J\sum_{i\in{\rm A}}\sum_{j\in{\rm B}} l_{i,j}V^{(9)}_{ij;k_+k'_+l_+l'_+}, \end{aligned} \tag{4.27b}$$

$$\begin{aligned} &\left[\mathcal{V}^{--}\right]_{(k'_--1)L_-+k_-,(l'_--1)L_-+l_-} \\ &\quad = \delta_{k_-,l_-}\delta_{k'_-,l'_-}\left(\varepsilon^{-}_{l_-} + \varepsilon^{-}_{l'_-}\right) - 2J\sum_{i\in{\rm A}}\sum_{j\in{\rm B}} l_{i,j}V^{(1)}_{ij;k_-k'_-l_-l'_-}. \end{aligned} \tag{4.27c}$$

The Lehmann representation [75] of the two-magnon GFs reads

$$G^{k_\sigma k'_{\sigma'}}_{l_\sigma l'_{\sigma'}}(\omega) = \sum_{\lambda=0}^{L_\sigma L_{\sigma'}-1} \frac{\hbar g_\lambda^{k_\sigma k'_{\sigma'}} \left(g_\lambda^{l_\sigma l'_{\sigma'}}\right)^*}{\hbar\omega - \hbar\Omega_\lambda^{\sigma\sigma'} + i\eta}. \tag{4.28}$$

Likewise, we consider the three-leg-ladder analogs [76, 77] of the Bethe-Salpeter equations for the three-magnon GFs

$$\begin{aligned} G^{k_+k'_+k''_-}_{l_+l'_+l''_-}(\omega) &= G^{k_+k'_+k''_-}_{l_+l'_+l''_-}(\omega)_{\rm BL} - \frac{J}{\hbar} \sum_{p_+,p'_+,p''_-} \sum_{q_+,q'_+,q''_-} G^{k_+k'_+k''_-}_{p_+p'_+p''_-}(\omega)_{\rm BL} \\ &\times \sum_{i\in{\rm A}} \sum_{j\in{\rm B}} l_{i,j} \left(\delta_{p''_-,q''_-} V^{(9)}_{ij;p_+p'_+q_+q'_+} + \frac{1}{2}\delta_{p_+,q_+} V^{(4)}_{ij;p'_+q'_+p''_-q''_-} + \frac{1}{2}\delta_{p'_+,q'_+} V^{(4)}_{ij;p_+q_+p''_-q''_-} \right) G^{q_+q'_+q''_-}_{l_+l'_+l''_-}(\omega), \end{aligned} \tag{4.29a}$$

$$\begin{aligned} G^{k_-k'_-k''_+}_{l_-l'_-l''_+}(\omega) &= G^{k_-k'_-k''_+}_{l_-l'_-l''_+}(\omega)_{\rm BL} - \frac{J}{\hbar} \sum_{p_-,p'_-,p''_+} \sum_{q_-,q'_-,q''_+} G^{k_-k'_-k''_+}_{p_-p'_-p''_+}(\omega)_{\rm BL} \\ &\times \sum_{i\in{\rm A}} \sum_{j\in{\rm B}} l_{i,j} \left(\delta_{p''_+,q''_+} V^{(1)}_{ij;p_-p'_-q_-q'_-} + \frac{1}{2}\delta_{p_-,q_-} V^{(4)}_{ij;p''_+q''_+p'_-q'_-} + \frac{1}{2}\delta_{p'_-,q'_-} V^{(4)}_{ij;p''_+q''_+p_-q_-} \right) G^{q_-q'_-q''_+}_{l_-l'_-l''_+}(\omega), \end{aligned} \tag{4.29b}$$

denoting the unperturbed three-magnon GFs by

$$\begin{aligned} G^{k_\sigma k'_\sigma k''_{\bar\sigma}}_{l_\sigma l'_\sigma l''_{\bar\sigma}}(\omega)_{\rm BL} &\equiv \int_{-\infty}^{\infty} \frac{dt}{i} e^{i\omega t} {}_{\rm BL}\langle 0|\mathcal{T}\alpha^\sigma_{k_\sigma}(t)_{\rm BL}\alpha^\sigma_{k'_\sigma}(t)_{\rm BL}\alpha^{\bar\sigma}_{k''_{\bar\sigma}}(t)_{\rm BL}\alpha^{\sigma\dagger}_{l_\sigma}\alpha^{\sigma\dagger}_{l'_\sigma}\alpha^{\bar\sigma\dagger}_{l''_{\bar\sigma}}|0\rangle_{\rm BL} \\ &= -\int_{-\infty}^{\infty} dt\, e^{i\omega t} \left[G^{k_\sigma}_{l_\sigma}(t)_{\rm BL} G^{k'_\sigma}_{l'_\sigma}(t)_{\rm BL} + G^{k_\sigma}_{l'_\sigma}(t)_{\rm BL} G^{k'_\sigma}_{l_\sigma}(t)_{\rm BL} \right] G^{k''_{\bar\sigma}}_{l''_{\bar\sigma}}(t)_{\rm BL} \\ &= \frac{\hbar(\delta_{k_\sigma,l_\sigma}\delta_{k'_\sigma,l'_\sigma} + \delta_{k_\sigma,l'_\sigma}\delta_{k'_\sigma,l_\sigma})\delta_{k''_{\bar\sigma},l''_{\bar\sigma}}}{\hbar\omega - \varepsilon^\sigma_{l_\sigma} - \varepsilon^\sigma_{l'_\sigma} - \varepsilon^{\bar\sigma}_{l''_{\bar\sigma}} + i\eta}. \end{aligned} \tag{4.30}$$

We solve the eigenequations obtained from (4.29a) and (4.29b),

$$\mathcal{V}^{\sigma\sigma\bar\sigma}\boldsymbol{g}^{\sigma\sigma\bar\sigma}_\lambda = \hbar\Omega^{\sigma\sigma\bar\sigma}_\lambda \boldsymbol{g}^{\sigma\sigma\bar\sigma}_\lambda, \tag{4.31}$$

where $\boldsymbol{g}^{\sigma\sigma\bar\sigma}_\lambda$ are the column vectors of dimension $L^2_\sigma L_{\bar\sigma}$ whose $[(k''_{\bar\sigma}-1)L^2_\sigma + (k'_\sigma-1)L_\sigma + k_\sigma]$-elements are given by

$$\left[\boldsymbol{g}^{\sigma\sigma\bar\sigma}_\lambda\right]_{(k''_{\bar\sigma}-1)L^2_\sigma+(k'_\sigma-1)L_\sigma+k_\sigma} \equiv g^{k_\sigma k'_\sigma k''_{\bar\sigma}}_\lambda \equiv \langle 0|\alpha^\sigma_{k_\sigma}\alpha^\sigma_{k'_\sigma}\alpha^{\bar\sigma}_{k''_{\bar\sigma}}|\lambda\rangle, \tag{4.32}$$

while $\mathcal{V}^{\sigma\sigma\bar\sigma}$ are the matrices of dimension $L^2_\sigma L_{\bar\sigma} \times L^2_\sigma L_{\bar\sigma}$ whose $[(k''_{\bar\sigma}-1)L^2_\sigma + (k'_\sigma-1)L_\sigma + k_\sigma, (l''_{\bar\sigma}-1)L^2_\sigma + (l'_\sigma-1)L_\sigma + l_\sigma]$-elements are given by

$$\begin{aligned} &\left[\mathcal{V}^{++-}\right]_{(k''_--1)L^2_++(k'_+-1)L_++k_+,(l''_--1)L^2_++(l'_+-1)L_++l_+} \\ &\quad = \delta_{k_+,l_+}\delta_{k'_+,l'_+}\delta_{k''_-,l''_-}\left(\varepsilon^+_{l_+} + \varepsilon^+_{l'_+} + \varepsilon^-_{l''_-}\right) \\ &\qquad - J\sum_{i\in{\rm A}}\sum_{j\in{\rm B}} l_{i,j}\left(2\delta_{k''_-,l''_-}V^{(9)}_{ij;k_+k'_+l_+l'_+} + \delta_{k_+,l_+}V^{(4)}_{ij;k'_+l'_+k''_-l''_-} + \delta_{k'_+,l'_+}V^{(4)}_{ij;k_+l_+k''_-l''_-}\right), \end{aligned} \tag{4.33a}$$

$$\left[\mathcal{V}^{--+}\right]_{(k''_+-1)L^2_-+(k'_--1)L_-+k_-,(l''_+-1)L^2_-+(l'_--1)L_-+l_-}$$

$$= \delta_{k_-,l_-}\delta_{k'_-,l'_-}\delta_{k''_+,l''_+}\left(\varepsilon^-_{l_-}+\varepsilon^-_{l'_-}+\varepsilon^+_{l''_+}\right)$$
$$- J\sum_{i\in\mathrm{A}}\sum_{j\in\mathrm{B}} l_{i,j}\left(2\delta_{k''_+,l''_+}V^{(1)}_{ij;k_-k'_-l_-l'_-}+\delta_{k_-,l_-}V^{(4)}_{ij;k''_+l''_+k'_-l'_-}+\delta_{k'_-,l'_-}V^{(4)}_{ij;k''_+l''_+k_-l_-}\right). \quad (4.33b)$$

The Lehmann representation of the three-magnon GFs reads

$$G^{k_\sigma k'_\sigma k''_{\bar\sigma}}_{l_\sigma l'_\sigma l''_{\bar\sigma}}(\omega) = \sum_{\lambda=0}^{L^2_\sigma L_{\bar\sigma}-1}\frac{\hbar g^{k_\sigma k'_\sigma k''_{\bar\sigma}}_\lambda\left(g^{l_\sigma l'_\sigma l''_{\bar\sigma}}_\lambda\right)^*}{\hbar\omega-\hbar\Omega^{\sigma\sigma\bar\sigma}_\lambda+i\eta}. \quad (4.34)$$

Therefore, the four-magnon GF which is decomposed into two-magnon GFs (4.20) reads

$$\begin{aligned}
G^{k_+k'_+k''_-k'''_-}_{l_+l'_+l''_-l'''_-}(\omega) &\simeq i\int_{-\infty}^{\infty}dt\,e^{i\omega t}\left[2G^{k_+k''_-}_{l_+l''_-}(t)G^{k'_+k'''_-}_{l'_+l'''_-}(t)+\frac{1}{2}G^{k_+k'_+}_{l_+l'_+}(t)G^{k''_-k'''_-}_{l''_-l'''_-}(t)\right]\\
&= i\int_{-\infty}^{\infty}\frac{ds}{2\pi}\left[2G^{k_+k''_-}_{l_+l''_-}(s)G^{k'_+k'''_-}_{l'_+l'''_-}(\omega-s)+\frac{1}{2}G^{k_+k'_+}_{l_+l'_+}(s)G^{k''_-k'''_-}_{l''_-l'''_-}(\omega-s)\right]\\
&= 2\sum_{\lambda,\lambda'=0}^{L_+L_--1}\frac{\hbar g^{k_+k''_-}_\lambda\left(g^{l_+l''_-}_\lambda\right)^* g^{k'_+k'''_-}_{\lambda'}\left(g^{l'_+l'''_-}_{\lambda'}\right)^*}{\hbar\omega-\hbar\Omega^{+-}_\lambda-\hbar\Omega^{+-}_{\lambda'}+i\eta}\\
&\quad+\frac{1}{2}\sum_{\lambda=0}^{L^2_+-1}\sum_{\lambda'=0}^{L^2_--1}\frac{\hbar g^{k_+k'_+}_\lambda\left(g^{l_+l'_+}_\lambda\right)^* g^{k''_-k'''_-}_{\lambda'}\left(g^{l''_-l'''_-}_{\lambda'}\right)^*}{\hbar\omega-\hbar\Omega^{++}_\lambda-\hbar\Omega^{--}_{\lambda'}+i\eta},
\end{aligned} \quad (4.35)$$

and the four-magnon GF which is decomosed into three- and one-magnon GFs (4.21) reads

$$\begin{aligned}
G^{k_+k'_+k''_-k'''_-}_{l_+l'_+l''_-l'''_-}(\omega) &\simeq i\int_{-\infty}^{\infty}dt\,e^{i\omega t}\left[G^{k_+k'_+k''_-}_{l_+l'_+l''_-}(t)G^{k'''_-}_{l'''_-}(t)+G^{k''_-k'''_-k_+}_{l''_-l'''_-l_+}(t)G^{k'_+}_{l'_+}(t)\right]\\
&= i\int_{-\infty}^{\infty}\frac{ds}{2\pi}\left[G^{k_+k'_+k''_-}_{l_+l'_+l''_-}(s)G^{k'''_-}_{l'''_-}(\omega-s)+G^{k''_-k'''_-k_+}_{l''_-l'''_-l_+}(s)G^{k'_+}_{l'_+}(\omega-s)\right]\\
&= \sum_{\lambda=0}^{L^2_+L_--1}\frac{\hbar g^{k_+k'_+k''_-}_\lambda\left(g^{l_+l'_+l''_-}_\lambda\right)^*\delta_{k'''_-,l'''_-}}{\hbar\omega-\hbar\Omega^{++-}_\lambda-\varepsilon^-_{l'''_-}+i\eta}+\sum_{\lambda=0}^{L^2_-L_+-1}\frac{\hbar g^{k''_-k'''_-k_+}_\lambda\left(g^{l''_-l'''_-l_+}_\lambda\right)^*\delta_{k'_+,l'_+}}{\hbar\omega-\hbar\Omega^{--+}_\lambda-\varepsilon^+_{l'_+}+i\eta}.
\end{aligned} \quad (4.36)$$

4.4 Configuration-Interaction Formalism

The configuration-interaction (CI) scheme is typlically used beyond the Hartree-Fock scheme for many-body correlations in electron systems. The CI wavefunction generally consists of a linear combination of Hartree-Fock Slater determinants [78, 79, 80], including a certain set of quasiparticle excited states as well as the ground state. In our two- and four-magnon excitation CI (2M-4M-CI) scheme, the Hilbert space in which the bosonic Hamiltonian (3.1) operates is spanned by the up-to-four-magnon basis states

$$|0\mathrm{M}\rangle\equiv|0\rangle_{\mathrm{BL}},\ |2\mathrm{M}\rangle^{l_+}_{l_-}\equiv\alpha^{+\dagger}_{l_+}\alpha^{-\dagger}_{l_-}|0\rangle_{\mathrm{BL}},\ |4\mathrm{M}\rangle^{l_+l'_+}_{l_-l'_-}\equiv\frac{\alpha^{+\dagger}_{l_+}\alpha^{+\dagger}_{l'_+}\alpha^{-\dagger}_{l_-}\alpha^{-\dagger}_{l'_-}|0\rangle_{\mathrm{BL}}}{\sqrt{1+\delta_{l_+,l'_+}}\sqrt{1+\delta_{l_-,l'_-}}}, \quad (4.37)$$

where the ranges of the magnon operator indices are

$$1\le l_+\le L_+,\ 1\le l_-\le L_- \quad (4.38)$$

for $|2\mathrm{M}\rangle_{l_-}^{l_+}$ and

$$1 \le l_+ \le l'_+ \le L_+,\ 1 \le l_- \le l'_- \le L_- \tag{4.39}$$

for $|4\mathrm{M}\rangle_{l_-l'_-}^{l_+l'_+}$. Since both the Heisenberg Hamiltonian and Raman operator commute with the total magnetization, any other two- and four-magnon excited states are ineffective in the ground state Raman response. The numbers of magnon states are

$$N_{2\mathrm{M}} = L_+L_-,\ N_{4\mathrm{M}} = \frac{1}{4}L_+(L_+ + 1)L_-(L_- + 1), \tag{4.40}$$

and total number of configurations is

$$N_{\mathrm{CI}} = 1 + N_{2\mathrm{M}} + N_{4\mathrm{M}}. \tag{4.41}$$

We denote the magnon states as

$$|m\rangle \equiv \begin{cases} |0\mathrm{M}\rangle & (m = 0) \\ |2\mathrm{M}\rangle_{l_-}^{l_+} & (1 \le m \le N_{2\mathrm{M}}) \\ |4\mathrm{M}\rangle_{l_-l'_-}^{l_+l'_+} & (N_{2\mathrm{M}} + 1 \le m \le N_{\mathrm{CI}} - 1) \end{cases}, \tag{4.42}$$

and they satisfy

$$\sum_{m=0}^{N_{\mathrm{CI}}-1} |m\rangle\langle m| = 1. \tag{4.43}$$

The up-to-$O(S^0)$ 2M-4M-CI Hamiltonian is formally written as $N_{\mathrm{CI}} \times N_{\mathrm{CI}}$ matrix

$$\mathcal{H} = \left[\begin{array}{c|ccc|ccc} \langle 0\mathrm{M}|\mathcal{H}|0\mathrm{M}\rangle & \langle 0\mathrm{M}|\mathcal{H}|2\mathrm{M}\rangle_1^1 & \cdots & \langle 0\mathrm{M}|\mathcal{H}|2\mathrm{M}\rangle_{L_-}^{L_+} & \langle 0\mathrm{M}|\mathcal{H}|4\mathrm{M}\rangle_{11}^{11} & \cdots & \langle 0\mathrm{M}|\mathcal{H}|4\mathrm{M}\rangle_{L_-L_-}^{L_+L_+} \\ \hline {}_1^1\langle 2\mathrm{M}|\mathcal{H}|0\mathrm{M}\rangle & {}_1^1\langle 2\mathrm{M}|\mathcal{H}|2\mathrm{M}\rangle_1^1 & \cdots & {}_1^1\langle 2\mathrm{M}|\mathcal{H}|2\mathrm{M}\rangle_{L_-}^{L_+} & {}_1^1\langle 2\mathrm{M}|\mathcal{H}|4\mathrm{M}\rangle_{11}^{11} & \cdots & {}_1^1\langle 2\mathrm{M}|\mathcal{H}|4\mathrm{M}\rangle_{L_-L_-}^{L_+L_+} \\ \vdots & \vdots & \ddots & \vdots & \vdots & \ddots & \vdots \\ {}_{L_-}^{L_+}\langle 2\mathrm{M}|\mathcal{H}|0\mathrm{M}\rangle & {}_{L_-}^{L_+}\langle 2\mathrm{M}|\mathcal{H}|2\mathrm{M}\rangle_1^1 & \cdots & {}_{L_-}^{L_+}\langle 2\mathrm{M}|\mathcal{H}|2\mathrm{M}\rangle_{L_-}^{L_+} & {}_{L_-}^{L_+}\langle 2\mathrm{M}|\mathcal{H}|4\mathrm{M}\rangle_{11}^{11} & \cdots & {}_{L_-}^{L_+}\langle 2\mathrm{M}|\mathcal{H}|4\mathrm{M}\rangle_{L_-L_-}^{L_+L_+} \\ \hline {}_{11}^{11}\langle 4\mathrm{M}|\mathcal{H}|0\mathrm{M}\rangle & {}_{11}^{11}\langle 4\mathrm{M}|\mathcal{H}|2\mathrm{M}\rangle_1^1 & \cdots & {}_{11}^{11}\langle 4\mathrm{M}|\mathcal{H}|2\mathrm{M}\rangle_{L_-}^{L_+} & {}_{11}^{11}\langle 4\mathrm{M}|\mathcal{H}|4\mathrm{M}\rangle_{11}^{11} & \cdots & {}_{11}^{11}\langle 4\mathrm{M}|\mathcal{H}|4\mathrm{M}\rangle_{L_-L_-}^{L_+L_+} \\ \vdots & \vdots & \ddots & \vdots & \vdots & \ddots & \vdots \\ {}_{L_-L_-}^{L_+L_+}\langle 4\mathrm{M}|\mathcal{H}|0\mathrm{M}\rangle & {}_{L_-L_-}^{L_+L_+}\langle 4\mathrm{M}|\mathcal{H}|2\mathrm{M}\rangle_1^1 & \cdots & {}_{L_-L_-}^{L_+L_+}\langle 4\mathrm{M}|\mathcal{H}|2\mathrm{M}\rangle_{L_-}^{L_+} & {}_{L_-L_-}^{L_+L_+}\langle 4\mathrm{M}|\mathcal{H}|4\mathrm{M}\rangle_{11}^{11} & \cdots & {}_{L_-L_-}^{L_+L_+}\langle 4\mathrm{M}|\mathcal{H}|4\mathrm{M}\rangle_{L_-L_-}^{L_+L_+} \end{array}\right] \tag{4.44}$$

with $\mathcal{H} = \mathcal{H}_{\mathrm{BL}} + :\mathcal{H}^{(0)}:$. With the ladder-approximation Bethe-Salpeter equation formalism [cf. (4.23a), (4.23b), (4.23c), (4.29a) and (4.29b)] in mind, we retain only the magnon-number-conserving interactions $V^{(1)}_{ij;l_-l'_-l''_-l'''_-}$, $V^{(4)}_{ij;l_+l'_+l''_-l'''_-}$, and $V^{(9)}_{ij;l_+l'_+l''_+l'''_+}$ in our CI scheme as well. Then (4.44) reduces to

$$\mathcal{H} - \sum_{m=0}^{2} E^{(m)}$$

$$
= \begin{bmatrix}
\boxed{0} & & \\
 & \boxed{\begin{matrix} {}^{1}_{1}\langle 2\mathrm{M}|\mathcal{H}|2\mathrm{M}\rangle^{1}_{1} & \cdots & {}^{1}_{1}\langle 2\mathrm{M}|\mathcal{H}|2\mathrm{M}\rangle^{L_+}_{L_-} \\ \vdots & \ddots & \vdots \\ {}^{L_+}_{L_-}\langle 2\mathrm{M}|\mathcal{H}|2\mathrm{M}\rangle^{1}_{1} & \cdots & {}^{L_+}_{L_-}\langle 2\mathrm{M}|\mathcal{H}|2\mathrm{M}\rangle^{L_+}_{L_-} \end{matrix}} & \\
 & & \boxed{\begin{matrix} {}^{11}_{11}\langle 4\mathrm{M}|\mathcal{H}|4\mathrm{M}\rangle^{11}_{11} & \cdots & {}^{11}_{11}\langle 4\mathrm{M}|\mathcal{H}|4\mathrm{M}\rangle^{L_+L_+}_{L_-L_-} \\ \vdots & \ddots & \vdots \\ {}^{L_+L_+}_{L_-L_-}\langle 4\mathrm{M}|\mathcal{H}|4\mathrm{M}\rangle^{11}_{11} & \cdots & {}^{L_+L_+}_{L_-L_-}\langle 4\mathrm{M}|\mathcal{H}|4\mathrm{M}\rangle^{L_+L_+}_{L_-L_-} \end{matrix}}
\end{bmatrix}, \tag{4.45}
$$

whose matrix elements are explicitly written as

$$
{}^{k_+}_{k_-}\langle 2\mathrm{M}|\mathcal{H}|2\mathrm{M}\rangle^{l_+}_{l_-} = \delta_{k_+,l_+}\delta_{k_-,l_-}\left(\varepsilon^+_{l_+} + \varepsilon^-_{l_-}\right) - J\sum_{i\in\mathrm{A}}\sum_{j\in\mathrm{B}} l_{i,j} V^{(4)}_{ij;k_-l_-k_+l_+}, \tag{4.46}
$$

$$
\begin{aligned}
{}^{k_+k'_+}_{k_-k'_-}\langle 4\mathrm{M}|\mathcal{H}|4\mathrm{M}\rangle^{l_+l'_+}_{l_-l'_-} &= \delta_{k_+,l_+}\delta_{k'_+,l'_+}\delta_{k_-,l_-}\delta_{k'_-,l'_-}\left(\varepsilon^+_{l_+} + \varepsilon^+_{l'_+} + \varepsilon^-_{l_-} + \varepsilon^-_{l'_-}\right) - J\sum_{i\in\mathrm{A}}\sum_{j\in\mathrm{B}} l_{i,j} \\
&\times \Bigg[\frac{\delta_{k_+,l_+}\delta_{k'_+,l'_+}}{\sqrt{1+\delta_{k_-,k'_-}}\sqrt{1+\delta_{l_-,l'_-}}}\left(V^{(1)}_{ij;k_-l_-l'_-k'_-} + V^{(1)}_{ij;k_-l'_-l_-k'_-} + V^{(1)}_{ij;k'_-l_-l'_-k_-} + V^{(1)}_{ij;k'_-l'_-l_-k_-}\right) \\
&+ \frac{\delta_{k_-,l_-}\delta_{k'_-,l'_-}}{\sqrt{1+\delta_{k_+,k'_+}}\sqrt{1+\delta_{l_+,l'_+}}}\left(V^{(9)}_{ij;l_+k_+k'_+l'_+} + V^{(9)}_{ij;l'_+k_+k'_+l_+} + V^{(9)}_{ij;l_+k'_+k_+l'_+} + V^{(9)}_{ij;l'_+k'_+k_+l_+)}\right) \\
&+ \frac{1}{\sqrt{1+\delta_{k_+,k'_+}}\sqrt{1+\delta_{l_+,l'_+}}\sqrt{1+\delta_{k_-,k'_-}}\sqrt{1+\delta_{l_-,l'_-}}} \\
&\times \Big(V^{(4)}_{ij;k_-l_-k_+l_+}\delta_{k'_+,l'_+}\delta_{k'_-,l'_-} + V^{(4)}_{ij;k_-l'_-k_+l_+}\delta_{k'_+,l'_+}\delta_{k'_-,l_-} \\
&+ V^{(4)}_{ij;k'_-l_-k_+l_+}\delta_{k'_+,l'_+}\delta_{k_-,l'_-} + V^{(4)}_{ij;k'_-l'_-k_+l_+}\delta_{k'_+,l'_+}\delta_{k_-,l_-} \\
&+ V^{(4)}_{ij;k_-l_-k_+l'_+}\delta_{k'_+,l_+}\delta_{k'_-,l'_-} + V^{(4)}_{ij;k_-l'_-k_+l'_+}\delta_{k'_+,l_+}\delta_{k'_-,l_-} \\
&+ V^{(4)}_{ij;k'_-l_-k_+l'_+}\delta_{k'_+,l_+}\delta_{k_-,l'_-} + V^{(4)}_{ij;k'_-l'_-k_+l'_+}\delta_{k'_+,l_+}\delta_{k_-,l_-} \\
&+ V^{(4)}_{ij;k_-l_-k'_+l_+}\delta_{k_+,l'_+}\delta_{k'_-,l'_-} + V^{(4)}_{ij;k_-l'_-k'_+l_+}\delta_{k_+,l'_+}\delta_{k'_-,l_-} \\
&+ V^{(4)}_{ij;k'_-l_-k'_+l_+}\delta_{k_+,l'_+}\delta_{k_-,l'_-} + V^{(4)}_{ij;k'_-l'_-k'_+l_+}\delta_{k_+,l'_+}\delta_{k_-,l_-} \\
&+ V^{(4)}_{ij;k_-l_-k'_+l'_+}\delta_{k_+,l_+}\delta_{k'_-,l'_-} + V^{(4)}_{ij;k_-l'_-k'_+l'_+}\delta_{k_+,l_+}\delta_{k'_-,l_-} \\
&+ V^{(4)}_{ij;k'_-l_-k'_+l'_+}\delta_{k_+,l_+}\delta_{k_-,l'_-} + V^{(4)}_{ij;k'_-l'_-k'_+l'_+}\delta_{k_+,l_+}\delta_{k_-,l_-}\Big)\Bigg].
\end{aligned} \tag{4.47}
$$

We diagonalize the 2M-4M-CI Hamiltonian matrix (4.45) to obtain the variationally corrected eigenstates $|\nu\rangle$ and and eigenvectors $|\nu\rangle$ ($\nu = 0, 1, \cdots, N_{\mathrm{CI}}-1$), the $2l$-magnon-mediated

Raman scattering intensities by the CI scheme are calculated as

$$
\begin{aligned}
{}^{[p]}I_{2l\mathrm{M}}(\omega) =& \frac{1}{L}\sum_{\nu=0}^{N_{\mathrm{CI}}-1}\left|\langle\nu|\sum_{n=1}^{p/2}{}^{[2n]}\mathcal{R}_{2l\mathrm{M}}|0\rangle\right|^2\delta(\hbar\omega-\varepsilon_\nu+\varepsilon_0)\\
=& \frac{1}{L}\sum_{\nu=0}^{N_{\mathrm{CI}}-1}\left|\sum_{m,m'=0}^{N_{\mathrm{CI}}-1}\langle\nu|m\rangle\langle m|\sum_{n=1}^{p/2}{}^{[2n]}\mathcal{R}_{2l\mathrm{M}}|m'\rangle\langle m'|0\rangle\right|^2\delta(\hbar\omega-\varepsilon_\nu+\varepsilon_0). \qquad (4.48)
\end{aligned}
$$

The complete correspondence of the two-magnon sector (4.46) of the CI Hamiltonian with the two-magnon Bethe-Salpeter interaction matrix $\mathcal{V}^{+-}$ (4.27a) means that the two-magnon excitation CI (2M-CI) Hamiltonian, i.e., (4.45) without any four-magnon basis state, and the relevant two-magnon Bethe-Salpeter equation, i.e., (4.23a), lead to exactly the same calculation of the two-magnon-mediated Raman intensity ${}^{[p]}I_{2\mathrm{M}}(\omega)$. (4.23b) and (4.23c) are irrelevant to any calculation of ${}^{[p]}I_{2\mathrm{M}}(\omega)$ but necessary for calculating ${}^{[p]}I_{4\mathrm{M}}(\omega)$, or more precisely, for decomposing the four-magnon GFs as (4.35). When we go beyond the Loudon-Fleury second-order perturbation theory and take a considerable interest in multimagnon-mediated Raman intensities, the 2M-4M-CI scheme is much superior to any tractable self-consistent GF formalism.

We calculate the ground-state energy E_{g} and compare each result in Table 4.2. The spin-wave findings are in good agreement with the exact ones $E_{\mathrm{g}}^{\mathrm{ex}}$. The Hartree-Fock interacting spin-waves, denoted by $\mathcal{H}_{\mathrm{BL}}(=\mathcal{H}^{(2)}+\mathcal{H}^{(1)}+:\mathcal{H}^{(0)}:)$, describe the ground state better than the linear spin-waves, denoted by $\mathcal{H}_{\mathrm{LSW}}(=\mathcal{H}^{(2)}+\mathcal{H}^{(1)})$. In the 2M-4M-CI formulation with the interactions keeping the number of magnons, no magnon-excited states mix with the ground-state vacuum. The correction to the magnon wave function is limited to the excited states and does not change the ground-state energy. When we incorporate the other terms in $:\mathcal{H}^{(0)}:$, there occurs a correction to the ground state as well as the excited states [80]. In the expansion of the Hamiltonian truncated up to $O(S^0)$, the spin-wave ground-state energy is lower than the exact one, and the modification of the ground state by the variational CI approach magnifies the deviation of E_{g} from the exact solution. Therefore, we exclude the magnon-number-non-conserving interactions in our CI calculations to avoid deterioration of the ground state.

Table 4.2: Spin-wave and configuration-interaction calculations of the ground-state energy E_{g} in comparison with the exact numerical calculations $E_{\mathrm{g}}^{\mathrm{ex}}$.

	Penrose				Ammann-Beenker	
	$L=16$		$L=26$		$L=25$	
Scheme	$\frac{E_{\mathrm{g}}}{LJ}$	$\frac{E_{\mathrm{g}}-E_{\mathrm{g}}^{\mathrm{ex}}}{LJ}$	$\frac{E_{\mathrm{g}}}{LJ}$	$\frac{E_{\mathrm{g}}-E_{\mathrm{g}}^{\mathrm{ex}}}{LJ}$	$\frac{E_{\mathrm{g}}}{LJ}$	$\frac{E_{\mathrm{g}}-E_{\mathrm{g}}^{\mathrm{ex}}}{LJ}$
exact	-0.553281	—	-0.547124	—	-0.554261	—
$\mathcal{H}_{\mathrm{LSW}}$	-0.546097	0.007184	-0.536501	0.010623	-0.546356	0.007906
$\mathcal{H}_{\mathrm{BL}}$	-0.554229	-0.000947	-0.550101	-0.002977	-0.555644	-0.001383
2M-4M-CI $(V^{(1)},V^{(4)},V^{(9)})$	-0.554229	-0.000947	-0.550101	-0.002977	-0.555644	-0.001383
2M-4M-CI (full $:\mathcal{H}^{(0)}:$)	-0.624608	-0.071326	-0.601796	-0.054671	-0.592903	-0.038642

4.5 Numerical Results

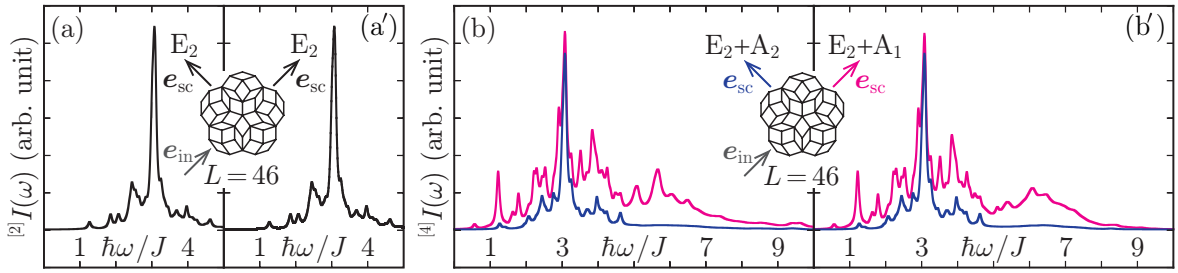

Figure 4.1: Green's function calculations of the Raman intensities ${}^{[p]}I(\omega) \equiv \sum_{l=1}^{2} {}^{[p]}I_{2l\mathrm{M}}(\omega)$ for the $L = 46$ two-dimensional Penrose lattice of $\mathbf{C}_{5\mathrm{v}}$ point symmetry in the Loudon-Fleury second-order ($p = 2$) [(a) and (a′)] and Shastry-Shraiman fourth-order ($p = 4$) [(b) and (b′)] perturbation schemes. ${}^{[p]}I_{2\mathrm{M}}(\omega)$ is obtained from the two-magnon Bethe-Salpeter equation (4.23a), while ${}^{[p]}I_{4\mathrm{M}}(\omega)$ is calculated in two ways, by the use of (4.35) [(a) and (b)] and (4.36) [(a′) and (b′)]. Three combinations of linear incident and scattered polarizations, $\phi_{\mathrm{sc}} - \phi_{\mathrm{in}} = 0, \pi/2$, are simulated. The perturbation parameter of the Raman operator $t/(U - \hbar\omega_{\mathrm{in}})$ is set equal to 1/9 and 9/10 within [(a) and (a′)] and beyond [(b) and (b′)] the Loudon-Fleury scheme, respectively. Every spectral line is Lorentzian-broadened by a width of $0.1J$.

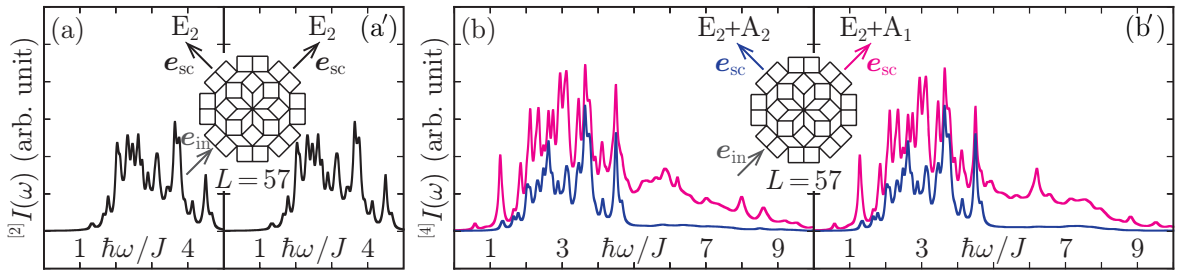

Figure 4.2: Green's function calculations of the Raman intensities ${}^{[p]}I(\omega) \equiv \sum_{l=1}^{2} {}^{[p]}I_{2l\mathrm{M}}(\omega)$ for the $L = 57$ two-dimensional Ammann-Beenker lattice of $\mathbf{C}_{8\mathrm{v}}$ point symmetry in the Loudon-Fleury second-order ($p = 2$) [(a) and (a′)] and Shastry-Shraiman fourth-order ($p = 4$) [(b) and (b′)] perturbation schemes. All other details are the same as Fig. 4.1.

Figures 4.1 and 4.2 show GF calculations of the Raman intensities ${}^{[p]}I(\omega) \equiv {}^{[p]}I_{2\mathrm{M}}(\omega) + {}^{[p]}I_{4\mathrm{M}}(\omega)$ in the $L = 46$ Penrose lattice of $\mathbf{C}_{5\mathrm{v}}$ point symmetry and the $L = 57$ Ammann-Beenker lattice of $\mathbf{C}_{8\mathrm{v}}$ point symmetry, respectively. For the linear polarizations $\boldsymbol{e}_{\mathrm{in}} = (\cos\phi_{\mathrm{in}}, \sin\phi_{\mathrm{in}}, 0)$ and $\boldsymbol{e}_{\mathrm{sc}} = (\cos\phi_{\mathrm{sc}}, \sin\phi_{\mathrm{sc}}, 0)$, the polarization-vector basis functions (4.10a) reads

$$\begin{aligned}
E^{\mathbf{C}_{5\mathrm{v}}}_{\mathrm{A}_1:1} &= E^{\mathbf{C}_{8\mathrm{v}}}_{\mathrm{A}_1:1} = \cos(\phi_{\mathrm{sc}} - \phi_{\mathrm{in}}),\\
E^{\mathbf{C}_{5\mathrm{v}}}_{\mathrm{A}_2:1} &= E^{\mathbf{C}_{8\mathrm{v}}}_{\mathrm{A}_2:1} = \sin(\phi_{\mathrm{sc}} - \phi_{\mathrm{in}}),\\
E^{\mathbf{C}_{5\mathrm{v}}}_{\mathrm{E}_2:1} &= E^{\mathbf{C}_{8\mathrm{v}}}_{\mathrm{E}_2:1} = \sin(\phi_{\mathrm{sc}} + \phi_{\mathrm{in}}),\\
E^{\mathbf{C}_{5\mathrm{v}}}_{\mathrm{E}_2:2} &= E^{\mathbf{C}_{8\mathrm{v}}}_{\mathrm{E}_2:2} = \cos(\phi_{\mathrm{sc}} + \phi_{\mathrm{in}}).
\end{aligned} \tag{4.49}$$

We focus on $\mathbf{P} = \mathbf{C}_{5\mathrm{v}}$ first. Since ${}^{[2]}\mathcal{R}^{\mathbf{C}_{5\mathrm{v}}}_{\mathrm{A}_1}$ commutes with the Heisenberg Hamiltonian, the A_1 species is Raman inactive within the Loudon-Fleury scheme. The A_2 species is also

Loudon-Fleury-Raman inactive. Since the Raman operator is time-reversal-invariant [40], the $(\boldsymbol{e}_{\rm in} \leftrightarrow \boldsymbol{e}_{\rm sc}^*)$-exchange-antisymmetric basis function $E^{\mathbf{C}_{5v}}_{\mathrm{A}_2:1}$ demands that ${}^{[p]}\mathcal{R}^{\mathbf{C}_{5v}}_{\mathrm{A}_2:1}$ be also time-reversal-antisymmetric. However, the second-order pair-exchange Raman vertices are all time-reversal-invariant. ${}^{[2]}\mathcal{R}$ for the two-dimensional Penrose lattice thus consists of one and only Raman-active species E_2 to yield depolarized spectra,

$$\begin{aligned} {}^{[2]}I(\omega) &= \left(\left| E^{\mathbf{C}_{5v}}_{\mathrm{E}_2:1} \right|^2 + \left| E^{\mathbf{C}_{5v}}_{\mathrm{E}_2:2} \right|^2 \right) {}^{[2]}I^{\mathbf{C}_{5v}}_{\mathrm{E}_2:1}(\omega) \\ &= \left[\sin^2(\phi_{\rm sc} + \phi_{\rm in}) + \cos^2(\phi_{\rm sc} + \phi_{\rm in}) \right] {}^{[2]}I^{\mathbf{C}_{5v}}_{\mathrm{E}_2:1}(\omega) = {}^{[2]}I^{\mathbf{C}_{5v}}_{\mathrm{E}_2:1}(\omega), \end{aligned} \tag{4.50}$$

as is shown in Figs. 4.1(a) and 4.1(a′). This is no longer the case with the fourth-order Raman vertices. ${}^{[4]}\mathcal{R}^{\mathbf{C}_{5v}}_{\mathrm{A}_1}$ contains ring-exchange spin fluctuations $(\boldsymbol{S}_i \cdot \boldsymbol{S}_j)(\boldsymbol{S}_k \cdot \boldsymbol{S}_l)$ incommutable with the Heisenberg Hamiltonian, whereas ${}^{[4]}\mathcal{R}^{\mathbf{C}_{5v}}_{\mathrm{A}_2}$ comprises chiral spin fluctuations $\boldsymbol{S}_i \cdot (\boldsymbol{S}_j \times \boldsymbol{S}_k)$ breaking the time-reversal symmetry, both of which drive the fourth-order Raman response to depend on the light polarization,

$${}^{[4]}I(\omega) = {}^{[4]}I^{\mathbf{C}_{5v}}_{\mathrm{E}_2:1}(\omega) + {}^{[4]}I^{\mathbf{C}_{5v}}_{\mathrm{A}_1:1}(\omega) \cos^2(\phi_{\rm sc} - \phi_{\rm in}) + {}^{[4]}I^{\mathbf{C}_{5v}}_{\mathrm{A}_2:1}(\omega) \sin^2(\phi_{\rm sc} - \phi_{\rm in}), \tag{4.51}$$

as is demonstrated in Figs. 4.1(b) and 4.1(b′). Even though we set $\mathbf{P} = \mathbf{C}_{8v}$, the polarization dependence is exactly the same because the polarization-vector basis function is the same as $\mathbf{C}_{5v}$.

Depolarization of ${}^{[2]}I(\omega)$ occurs in a certain class of periodic planar magnets as well, including Heisenberg antiferromagnets on the triangular [37] and kagome [38, 41] lattices and Kitaev spin liquids on the pure [81] and decorated [72] honeycomb lattices. In these lattice geometries, the two polarization-vector basis functions $e^x_{\rm in} e^{y\,*}_{\rm sc} + e^y_{\rm in} e^{x\,*}_{\rm sc}$ and $e^x_{\rm in} e^{x\,*}_{\rm sc} - e^y_{\rm in} e^{y\,*}_{\rm sc}$ span such a two-dimensional irreducible representation as to be one and only Raman-active symmetry species (see Table 4.1). This criterion is met by two-dimensional lattices with certain rotational symmetry, including periodic ones of triangular geometry and all noncrystallographic ones [1, 4]. Keeping in mind the correspondence between the 2×2 basis matrices $\boldsymbol{\Xi}_i$ (4.6) and the polarization-vector basis functions (4.8a), let us consider the $\mathbf{C}_{nv}$ symmetry operations on $\boldsymbol{\Xi}_i$ intending to reveal the possible dimensionality $d^{\mathbf{C}_{nv}}_{\Xi_i}$. We denote the matrix representation for a point symmetry operation $P \in \mathbf{P}$ by $\mathcal{P}$. Setting P to the rotation $C^z_n \in \mathbf{C}_{nv}$,

$$\mathcal{P} = \begin{bmatrix} \cos\dfrac{2\pi}{n} & \sin\dfrac{2\pi}{n} \\ -\sin\dfrac{2\pi}{n} & \cos\dfrac{2\pi}{n} \end{bmatrix}, \tag{4.52}$$

we obtain

$$\begin{aligned} &\mathcal{P}^{-1} \boldsymbol{\Xi}_0 \mathcal{P} = \boldsymbol{\Xi}_0, \\ &\mathcal{P}^{-1} \boldsymbol{\Xi}_1 \mathcal{P} = \boldsymbol{\Xi}_1 \cos\frac{4\pi}{n} - \boldsymbol{\Xi}_3 \sin\frac{4\pi}{n}, \\ &\mathcal{P}^{-1} \boldsymbol{\Xi}_2 \mathcal{P} = \boldsymbol{\Xi}_2, \\ &\mathcal{P}^{-1} \boldsymbol{\Xi}_3 \mathcal{P} = \boldsymbol{\Xi}_3 \cos\frac{4\pi}{n} + \boldsymbol{\Xi}_1 \sin\frac{4\pi}{n}, \end{aligned} \tag{4.53}$$

while setting P to the mirror operation $\sigma^{\rm v}_{\alpha_l} \in \mathbf{C}_{nv}$ with $\alpha_l \equiv l\pi/n$ $(l = 1, 2, \cdots, n)$ being the

angle between the normal vector and x axis,

$$\mathcal{P} = \begin{bmatrix} \cos 2\alpha_l & \sin 2\alpha_l \\ \sin 2\alpha_l & -\cos 2\alpha_l \end{bmatrix} = \begin{bmatrix} \cos\dfrac{2\pi l}{n} & \sin\dfrac{2\pi l}{n} \\ \sin\dfrac{2\pi l}{n} & -\cos\dfrac{2\pi l}{n} \end{bmatrix}, \tag{4.54}$$

we have

$$\begin{aligned} \mathcal{P}^{-1}\boldsymbol{\Xi}_0\mathcal{P} &= \boldsymbol{\Xi}_0, \\ \mathcal{P}^{-1}\boldsymbol{\Xi}_1\mathcal{P} &= -\boldsymbol{\Xi}_1 \cos\frac{4\pi l}{n} + \boldsymbol{\Xi}_3 \sin\frac{4\pi l}{n}, \\ \mathcal{P}^{-1}\boldsymbol{\Xi}_2\mathcal{P} &= -\boldsymbol{\Xi}_2, \\ \mathcal{P}^{-1}\boldsymbol{\Xi}_3\mathcal{P} &= \boldsymbol{\Xi}_3 \cos\frac{4\pi l}{n} + \boldsymbol{\Xi}_1 \sin\frac{4\pi l}{n}. \end{aligned} \tag{4.55}$$

$\boldsymbol{\Xi}_0$ and $\boldsymbol{\Xi}_2$ each correspond to a one-dimensional irreducible representation for any point symmetry group $\mathbf{C}_{n\mathrm{v}}$, whereas $\boldsymbol{\Xi}_1$ and $\boldsymbol{\Xi}_3$ span a two-dimensional irreducible representation unless $n = 2$ or $n = 4$. By definition [2, 3, 4], no quasiperiodic lattice in two dimensions belongs to either of $\mathbf{C}_{2\mathrm{v}}$ and $\mathbf{C}_{4\mathrm{v}}$, and therefore, depolarization of ${}^{[2]}I(\omega)$ is common to all two-dimensional quasiperiodic lattices.

Figures 4.1(a) and 4.1(a′) and Figs. 4.2(a) and 4.2(a′) present observations that are almost independent of the approximation of the four-magnon GFs, respectively, while Figs. 4.1(b) and 4.1(b′) and Figs. 4.2(b) and 4.2(b′) show an artificial difference at $\hbar\omega \gtrsim 5J$. ${}^{[4]}I(\omega)$ and more generally Raman responses beyond the Loudon-Fleury mechanism contain significant multimagnon contributions. The GF approach requires approximations because it is difficult to obtain more-than-three-magnon GFs directly, but the method is not unique. Even though in the calculation of the three-magnon GFs, we can calculate in several different manners with Bethe-Salpeter-like renormalization. We propose the CI variational wavefunction approach to avoid the decomposition of the four-magnon-mediated scattering, which is a source of complexity.

Once we proceed to the fourth-order perturbation scheme, the incident and scattered light polarization degrees of freedom for linearly polarized Raman spectra (4.51) are inadequate to identify all the three Raman-active symmetry species, and therefore, we consider circularly polarized components of them as well [33, 82]. For the incident and scattered fields of circular polarizations, $\boldsymbol{e}_{\mathrm{in}} = (1, \sigma_{\mathrm{in}}i, 0)/\sqrt{2}$ and $\boldsymbol{e}_{\mathrm{sc}} = (1, \sigma_{\mathrm{sc}}i, 0)/\sqrt{2}$, (4.10a) reads

$$\begin{aligned} E^{\mathbf{C}_{5\mathrm{v}}}_{\mathrm{A}_1:1} &= E^{\mathbf{C}_{8\mathrm{v}}}_{\mathrm{A}_1:1} = \frac{1 + \sigma_{\mathrm{in}}\sigma_{\mathrm{sc}}}{2}, \\ E^{\mathbf{C}_{5\mathrm{v}}}_{\mathrm{A}_2:1} &= E^{\mathbf{C}_{8\mathrm{v}}}_{\mathrm{A}_2:1} = -i\frac{\sigma_{\mathrm{in}} + \sigma_{\mathrm{sc}}}{2}, \\ E^{\mathbf{C}_{5\mathrm{v}}}_{\mathrm{E}_2:1} &= E^{\mathbf{C}_{8\mathrm{v}}}_{\mathrm{A}_2:1} = i\frac{\sigma_{\mathrm{in}} - \sigma_{\mathrm{sc}}}{2}, \\ E^{\mathbf{C}_{5\mathrm{v}}}_{\mathrm{E}_2:2} &= E^{\mathbf{C}_{8\mathrm{v}}}_{\mathrm{A}_2:1} = \frac{1 - \sigma_{\mathrm{in}}\sigma_{\mathrm{sc}}}{2} \end{aligned} \tag{4.56}$$

to yield the second- and fourth-order Raman responses

$${}^{[2]}I(\omega) = (1 - \sigma_{\mathrm{in}}\sigma_{\mathrm{sc}})\, {}^{[2]}I^{\mathbf{C}_{5\mathrm{v}}(\mathbf{C}_{8\mathrm{v}})}_{\mathrm{E}_2:1}(\omega), \tag{4.57}$$

$${}^{[4]}I(\omega) = (1 - \sigma_{\mathrm{in}}\sigma_{\mathrm{sc}})\, {}^{[4]}I^{\mathbf{C}_{5\mathrm{v}}(\mathbf{C}_{8\mathrm{v}})}_{\mathrm{E}_2:1}(\omega) + \frac{1 + \sigma_{\mathrm{in}}\sigma_{\mathrm{sc}}}{2}\left[{}^{[4]}I^{\mathbf{C}_{5\mathrm{v}}(\mathbf{C}_{8\mathrm{v}})}_{\mathrm{A}_1:1}(\omega) + {}^{[4]}I^{\mathbf{C}_{5\mathrm{v}}(\mathbf{C}_{8\mathrm{v}})}_{\mathrm{A}_2:1}(\omega)\right]. \tag{4.58}$$

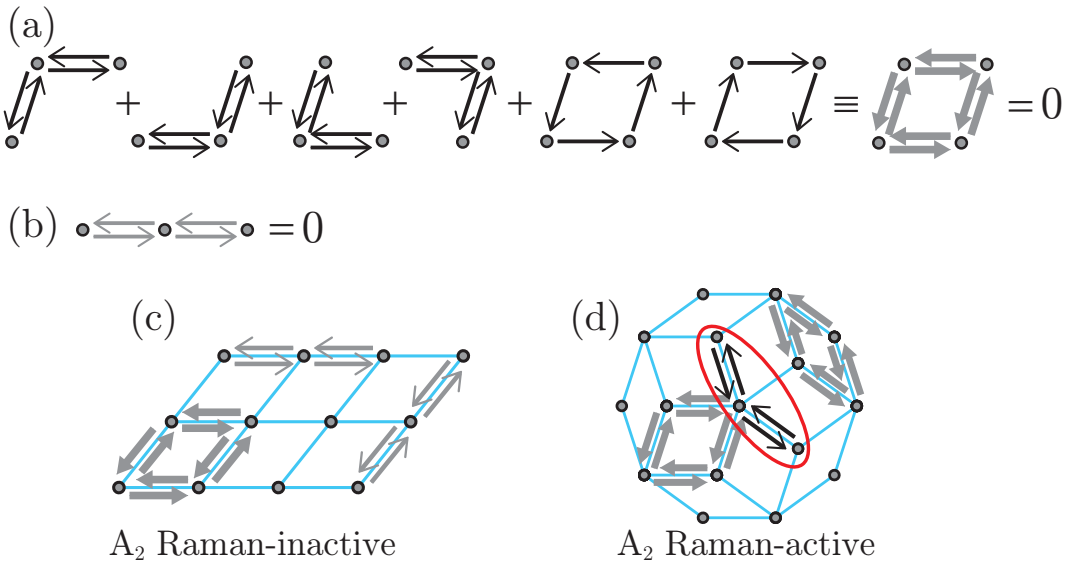

Figure 4.3: Fourth-order Raman operator paths with canceling chiral spin fluctuations. Four-site rhombic-loop path (a) and three-site straight-line path (b). Examples of A_2 Raman-inactive rank-2 periodic lattice (c) and A_2 Raman-active rank-4 quasiperiodic lattice (d).

Substituting (4.58) into (4.51) with $\phi_{\rm sc} - \phi_{\rm in}$ being set to 0 and $\pi/2$ reveals all the symmetry species separately. The spin-chirality-driven A_2 Raman response is emergent in the honeycomb and kagome lattices consisting of nonparallelograms but impossible in the square and triangular lattices comprising rhombuses [41] (Fig. 4.3). The present scattering of A_2 symmetry owes to the quasiperiodic geometry [52] whose rank $r = 4$ is larger than the actual physical dimension $d = 2$ for the Penrose and Ammann-Beenker lattices (Fig. 1.3).

To quantitatively evaluate the Raman spectra of each symmetric species, we calculate the Raman intensities in Hartree-Fock (HF) unperturbed eigenstates, 2M-CI corrected eigenstates, 2M-4M-CI corrected eigenstates, four-magnon GF corrected eigenstates approximated by three- and one-magnon GFs [2M+4($\simeq$3+1)M-GF], and four-magnon GF corrected eigenstates approximated by two-magnon GFs [2M+4($\simeq$2+2)M-GF], respectively. We show the cluster-size and calculational-scheme dependence of the Shastry-Shraiman fourth-order Raman spectra ${}^{[4]}I(\omega)$ for the $\mathbf{C}_{5v}$ Penrose (Figs. 4.4 to 4.8) and $\mathbf{C}_{8v}$ Ammann-Beenker (Figs. 4.9 and 4.10) lattices, intending to demonstrate the superiority of the 2M-4M-CI scheme over the others especially in evaluating 4M-mediated scattering intensities.

For the $L = 16$ Penrose (Fig. 4.4), $L = 26$ Penrose (Fig. 4.5) and $L = 25$ Ammann-Beenker (Fig. 4.9) clusters, all the perturbative and variational calculations are compared with the Lanczos exact solutions. The Hartree-Fock approximation cannot reproduce any of the major-peak positions. The 2M-CI formulation, which is equivalent to the two-magnon ladder-approximation Bethe-Salpeter equation, is good at reproducing the low-energy peaks essentially of two-magnon character but poor in describing higher-energy spectral weight of four-magnon character. The 2M-4M-CI formulation overcomes this drawback owing to its precise evaluation of four-magnon-mediated scattering intensities. This is not the case with any of the GF findings. Both (3+1)M and (2+2)M approximate evaluations of the four-magnon Raman correlation functon ${}^{[p]}\mathcal{G}_{4\rm M}(t)$ lead to a reasonable reduction of the higher-energy excess spectral weight, but neither of them gives such a satisfactory description of the intermediate-energy scattering bands of two- and four-magnon-mixed character as to be

obtained through the 2M-4M-CI formulation.

The 2M-4M-CI findings for the E_2 and A_2 symmetry species are in very good agreement with the exact solutions obtained by a recursion method based on the Lanczos algorithm. While the E_2 scattering is Loudon-Fleury-Raman active and arises chiefly from pair-exchange spin fluctuations, a nonnegligible portion of this scattering intensity is mediated by four-magnon fluctuations, as is revealed by our CI scheme. While the A_2 scattering intensity is small compared to the other symmetries, it is so interesting as to allow for direct observation of the chiral spin fluctuations $\boldsymbol{S}_i \cdot (\boldsymbol{S}_j \times \boldsymbol{S}_k)$ [33]. Comparing ${}^{[4]}I_{4\mathrm{M}}(\omega)$ from CI and GF calculations, the indirect evaluation of the four-magnon GFs in the conventional GF approach does not adequately reproduce the four-magnon-mediated scattering intensities and underestimates them. Fig. 4.9 reveals our CI approach to be much superior to the conventional GF approach. The first and second lowest peaks of the spin-chirality-driven A_2 scattering intensity are completely of two-magnon character, whereas the third peak located at $\hbar\omega = 3.88J$ owes to both two- and four-magnon-mediated scattering, as is revealed by the 2M-4M-CI calculations. However, the inaccurate four-magnon GFs are totally ignorant of the mixed character of this A_2 scattering peak. The tendency to underestimate the two- and four-magnon-mixed character in the intermediate-energy bands of the GF formulations is common to other symmetry species and different lattice sizes.

The 2M-4M-CI findings for the A_1 symmetry seem to overestimate the four-magnon-mediated scattering intensities. This is because the A_1 symmetry species is dominated by the contribution of the ring-exchange terms. In this paper, we consider up to four-magnon comtributions for the ring exchange terms $(\boldsymbol{S}_i \cdot \boldsymbol{S}_j)(\boldsymbol{S}_k \cdot \boldsymbol{S}_l)$ as in (3.31) and (3.32). Of the ring-exchange terms that are expanded as $S_i^+ S_j^- S_k^+ S_l^-$, $S_i^+ S_j^- S_k^z S_l^z$, and $S_i^z S_j^z S_k^z S_l^z$, the latter two are essentially described by six or more Holstein-Primakoff bosons. Therefore, spin-wave calculations are sensitive to the $O(S^{-1})$ Hamiltonian, whether in the GF description (4.15) or through the CI scheme (4.48).

We further consider the $\mathbf{C}_{5\mathrm{v}}$ Penrose lattices of $L = 41$ (Fig. 4.6), $L = 46$ (Fig. 4.7), $L = 56$ (Fig. 4.8) and $\mathbf{C}_{8\mathrm{v}}$ Ammann-Beenker lattice of $L = 57$ (Fig. 4.10). With increasing system size, the spectral shape and/or density change in a complicated manner, but the balance in intensity sharing between two- and four-magnon scatterings remains qualitatively the same. The energy ranges in which two-magnon scattering intensities distribute for the three symmetry species each remain almost unchanged from those of the smallest cluster calculated and this is essentially the case with four-magnon scattering intensities as well. Indeed, neither of the range of the eigenvalue distribution nor the specific heat curve is sensitive to the system size for the $L \gtrsim 31$ Penrose and $L \gtrsim 33$ Ammann-Beenker lattices, as was already shown in Fig. 3.1. Eigenvalues corresponding to the highest or second highest coordination numbers have no serious effect on bulk properties.

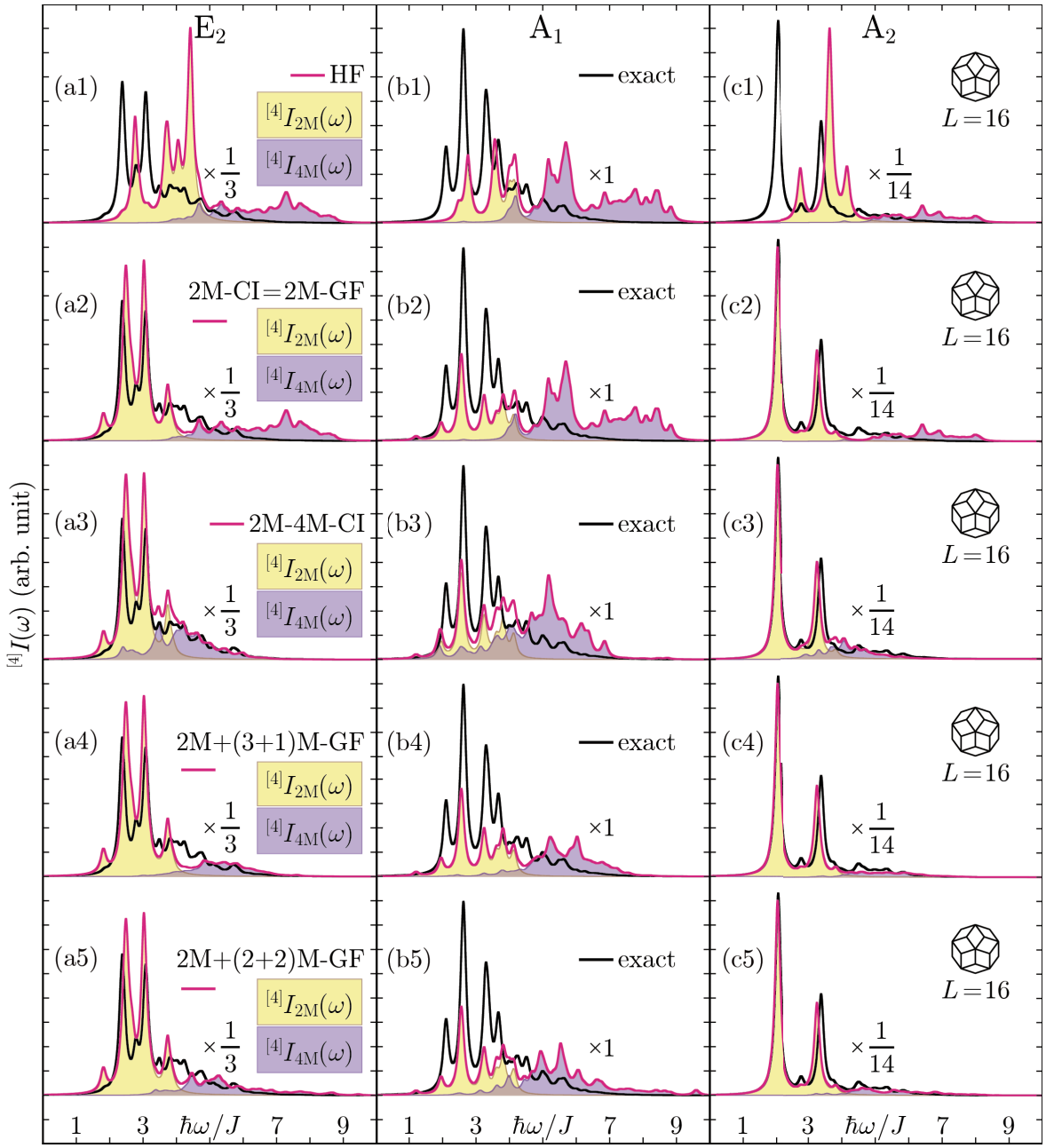

Figure 4.4: CI and GF calculations of the Shastry-Shraiman fourth-order Raman intensities ${}^{[4]}I(\omega) \equiv \sum_{l=1}^{2} {}^{[4]}I_{2l\mathrm{M}}(\omega)$ for the $L = 16$ two-dimensional Penrose lattice of $\mathbf{C}_{5\mathrm{v}}$ point symmetry with the exact solutions, where the perturbation parameter $t/(U - \hbar\omega_{\mathrm{in}})$ is set to 9/10 and every spectral line is Lorentzian-broadened by a width of $0.1J$. From the top to the bottom, the calculated schemes employed are the Hartree-Fock (HF) approximation [(a1) to (c1)], which retains only the magnon vacuum in (4.37) and substitutes the eigenstates and eigenvalues of $\mathcal{H}_{\mathrm{BL}}$ (3.20) for the basis states $|\nu\rangle$ and their energies ε_ν, 2M-CI [(a2) to (c2)], which is equivalent to solving the two-magnon Bethe-Salpeter equation (4.23a), 2M-4M-CI [(a3) to (c3)], 2M+4M [approximated (4.35)]-GF [(a4) to (c4)], and 2M+4M [approximated (4.36)]-GF [(a5) to (c5)]. The pure symmetry components are extracted from three polarization combinations, (4.51) with $\phi_{\mathrm{sc}} - \phi_{\mathrm{in}} = 0, \pi/2$ and (4.58) with $\sigma_{\mathrm{in}}\sigma_{\mathrm{sc}} = -1$. All the spin-wave calculations of ${}^{[4]}I_{2l\mathrm{M}}(\omega)$ each are distinguishably colored.

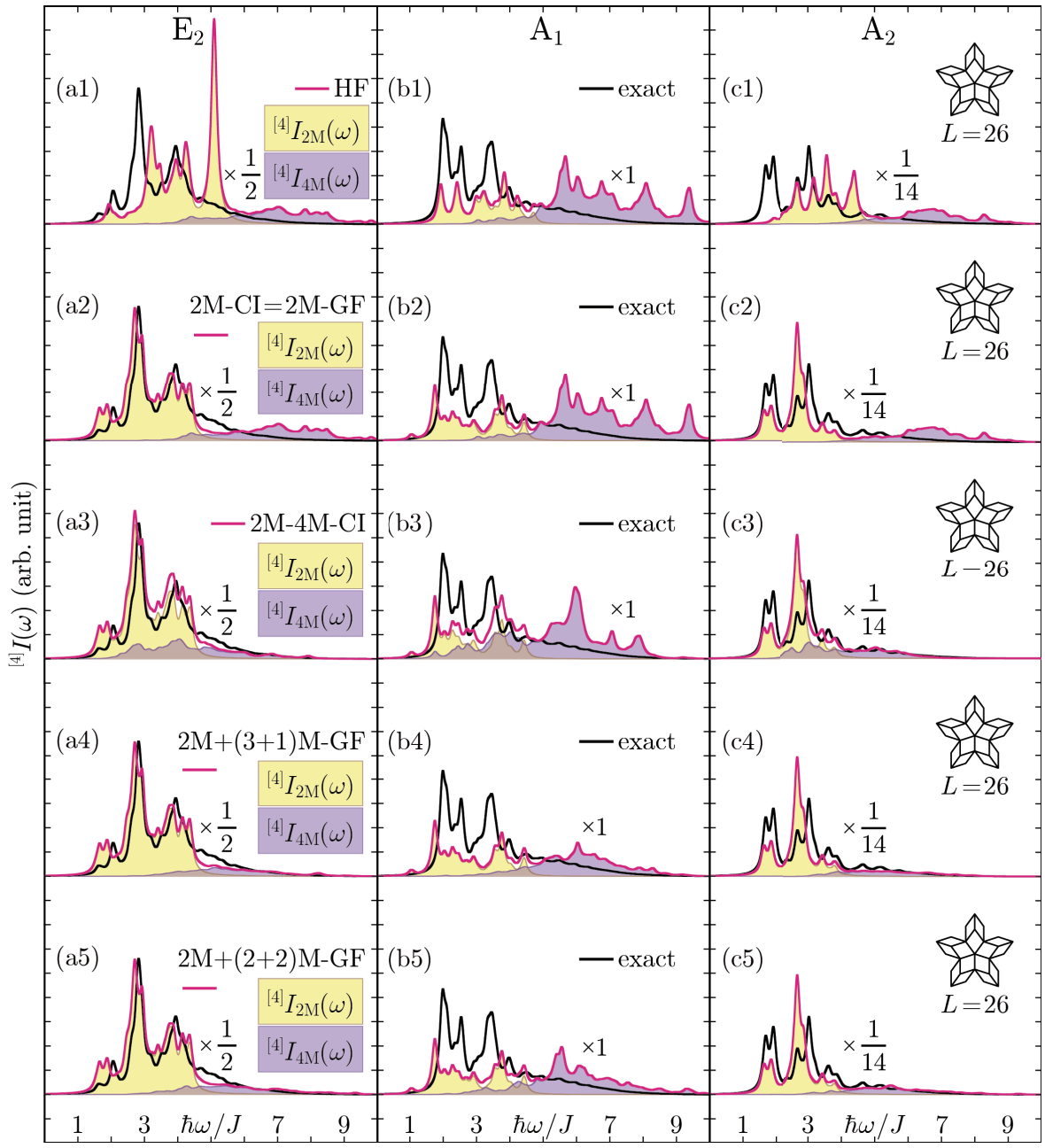

Figure 4.5: The same as Fig. 4.4 for the $L = 26$ two-dimensional Penrose lattice of $\mathbf{C}_{5\mathrm{v}}$ point symmetry.

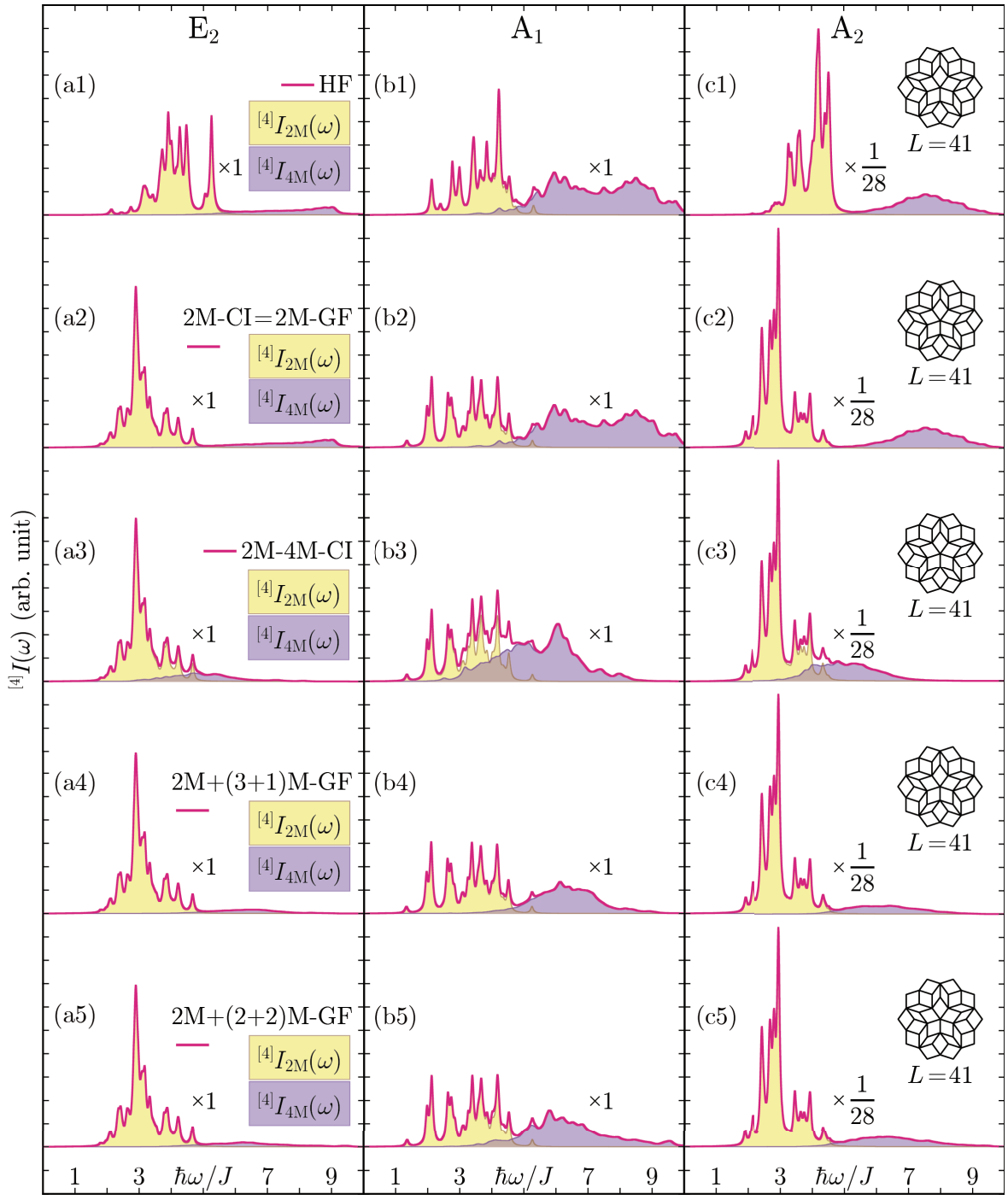

Figure 4.6: The same as Fig. 4.4 for the $L = 41$ two-dimensional Penrose lattice of $\mathbf{C}_{5v}$ point symmetry without any exact solution available.

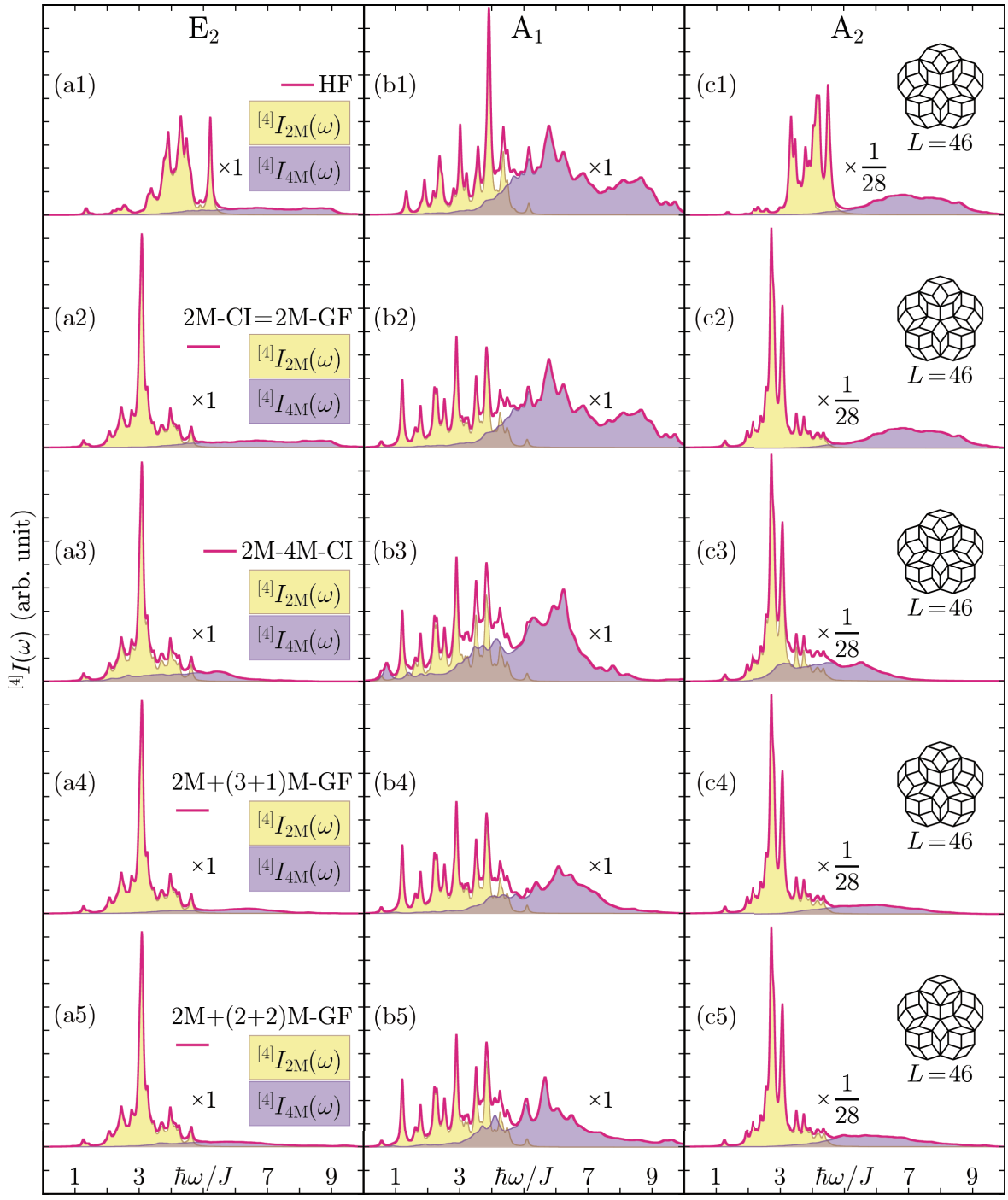

Figure 4.7: The same as Fig. 4.4 for the $L = 46$ two-dimensional Penrose lattice of $\mathbf{C}_{5\mathrm{v}}$ point symmetry without any exact solution available.

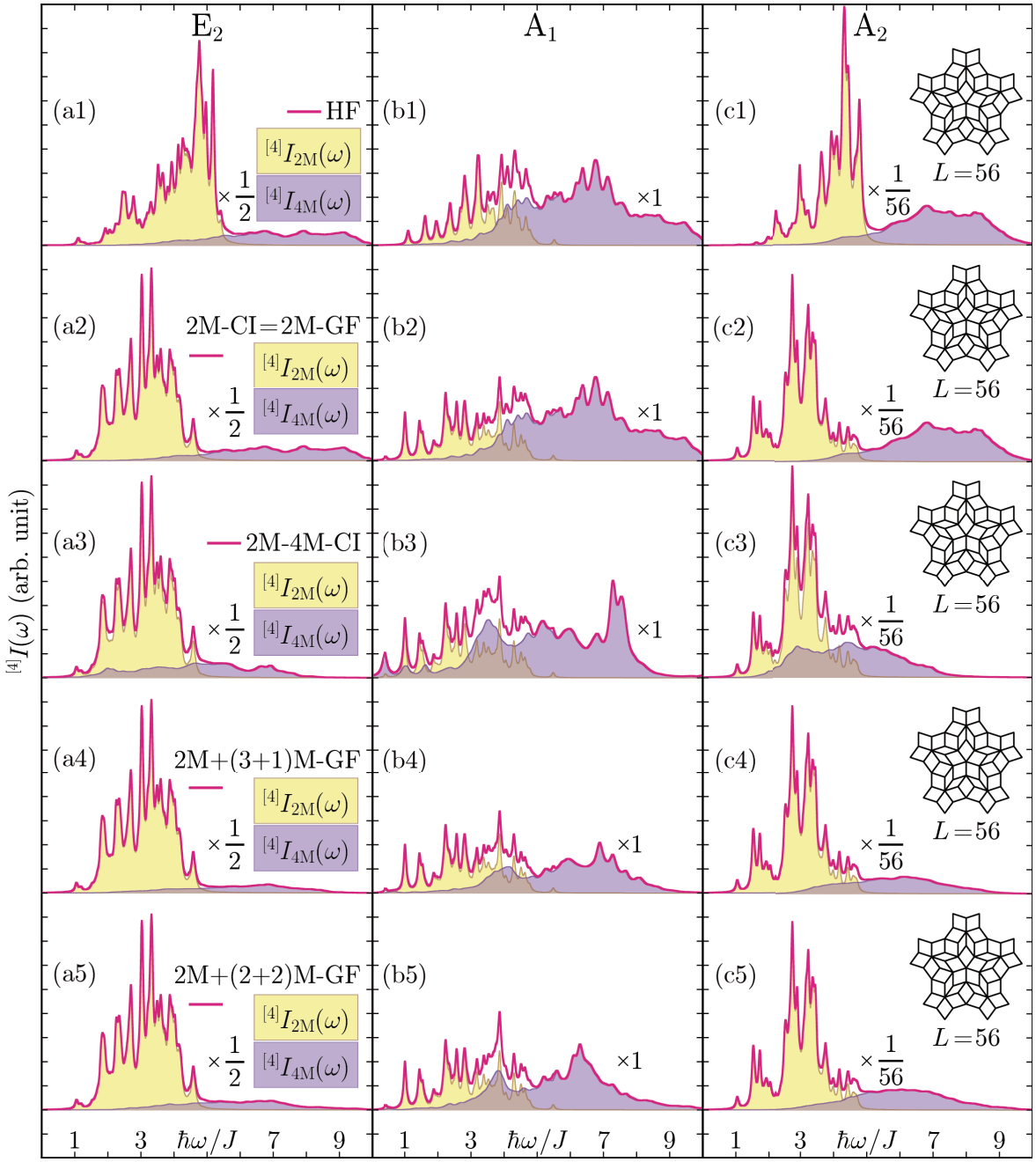

Figure 4.8: The same as Fig. 4.4 for the $L = 56$ two-dimensional Penrose lattice of $\mathbf{C}_{5v}$ point symmetry without any exact solution available.

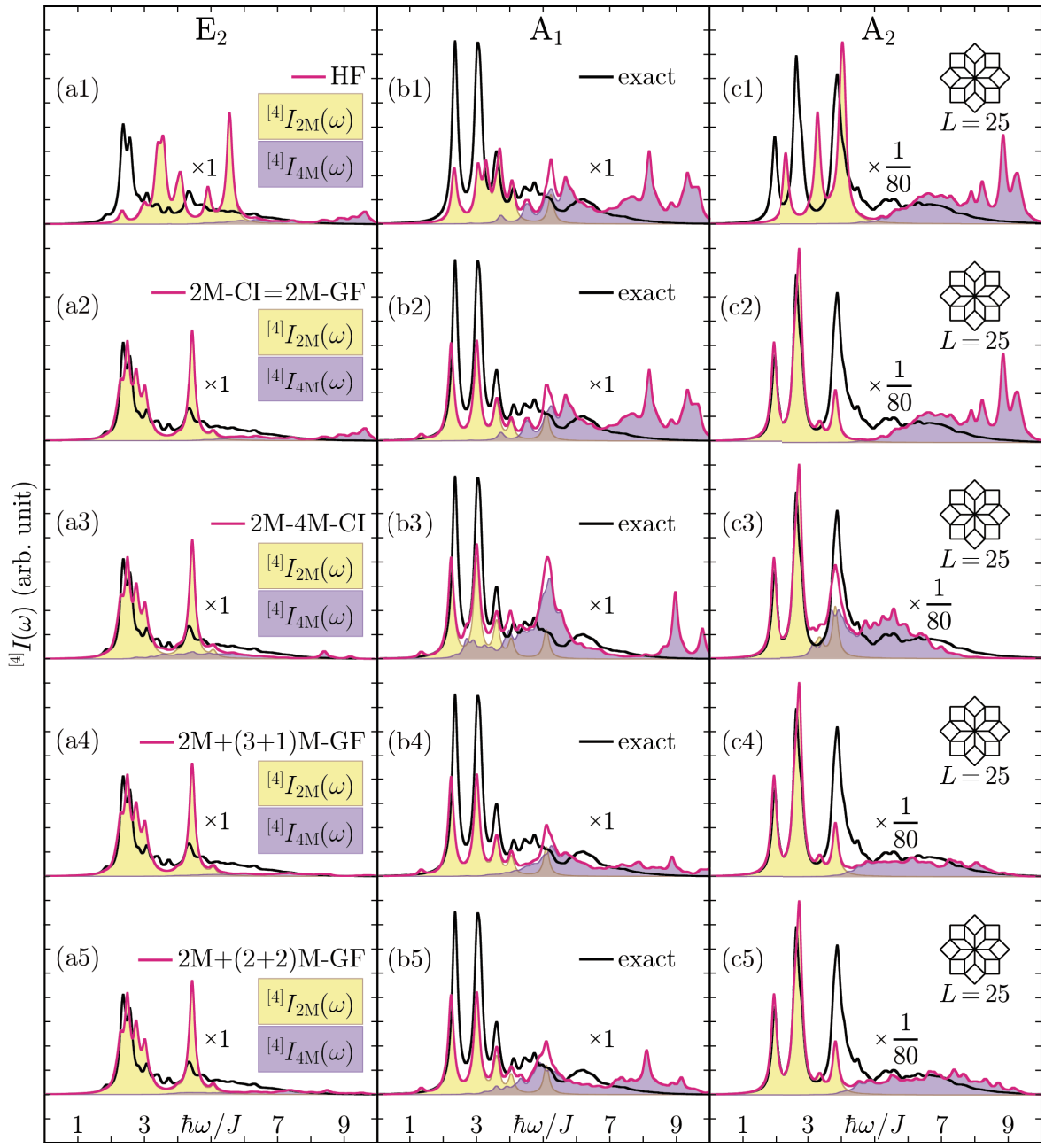

Figure 4.9: The same as Fig. 4.4 for the $L = 25$ two-dimensional Ammann-Beenker lattice of $\mathbf{C}_{8v}$ point symmetry.

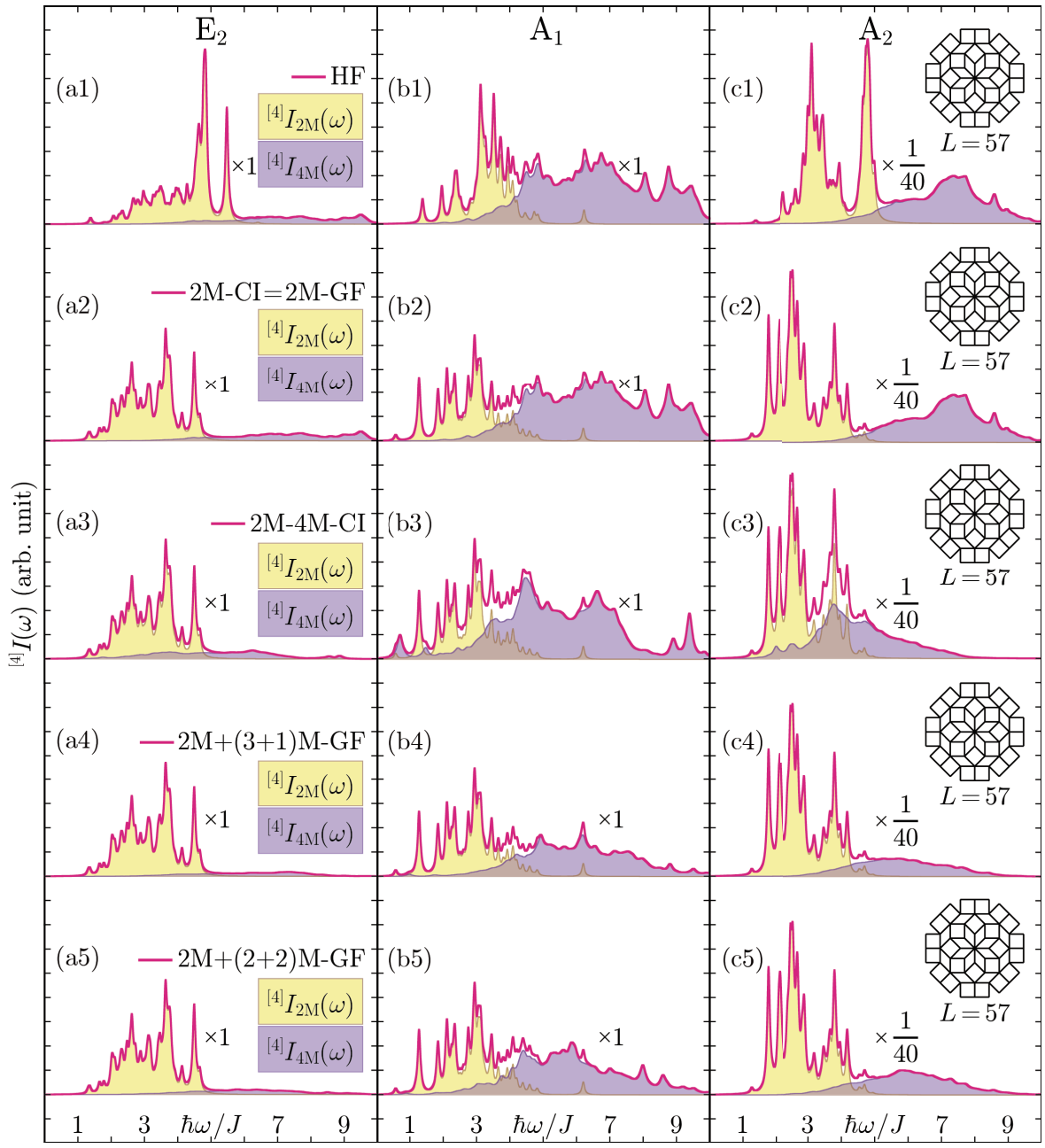

Figure 4.10: The same as Fig. 4.4 for the $L = 25$ two-dimensional Ammann-Beenker lattice of $\mathbf{C}_{8v}$ point symmetry without any exact solution available.

Chapter 5

Inelastic Neutron Scattering

5.1 Dynanic Structure Factor

The dynamic structure factors read [60]

$$S^{\lambda\lambda'}(\boldsymbol{q},\omega) \equiv \frac{1}{2\pi\hbar L}\int_{-\infty}^{\infty} dt e^{i\omega t}\sum_{k,k'=1}^{L} e^{i\boldsymbol{q}\cdot(\boldsymbol{r}_k-\boldsymbol{r}_{k'})}\langle \delta S_k^{\lambda}(t)\delta S_{k'}^{\lambda'}\rangle;$$
$$\delta S_k^{\lambda} \equiv S_k^{\lambda} - \langle S_k^{\lambda}\rangle,\ \delta S_k^{\lambda}(t) \equiv e^{\frac{i}{\hbar}\mathcal{H}t}\delta S_k^{\lambda} e^{-\frac{i}{\hbar}\mathcal{H}t}. \tag{5.1}$$

Having mind that the time-dependent magnon operator in the Heisenberg picture $\alpha(t) \equiv e^{i\mathcal{H}t/\hbar}\alpha e^{-i\mathcal{H}t/\hbar}$, the dynamic structure factors up to $O(S^0)$ read

$$S^{zz}(\boldsymbol{q},\omega) = \sum_{l_-,l_+}\left|c_{-+}^{(0)}(\boldsymbol{q};l_-,l_+)\right|^2\delta(\hbar\omega-\varepsilon_{l_-}^{-}-\varepsilon_{l_+}^{+}),$$
$$S^{\perp}(\boldsymbol{q},\omega) \equiv S^{xx}(\boldsymbol{q},\omega)+S^{yy}(\boldsymbol{q},\omega)$$
$$= \sum_{\sigma=\pm}\sum_{l_\sigma}\left\{\frac{1}{2}\left|c_{\sigma}^{(\frac{1}{2})}(\boldsymbol{q};l_\sigma)\right|^2 + \mathrm{Re}\left[c_{\sigma}^{(\frac{1}{2})}(\boldsymbol{q};l_\sigma)c_{\sigma}^{(-\frac{1}{2})}(\boldsymbol{q};l_\sigma)^*\right]\right\}\delta(\hbar\omega-\varepsilon_{l_\sigma}^{\sigma}). \tag{5.2}$$

The coefficients read

$$c_{-+}^{(0)}(\boldsymbol{q};l_-,l_+) = \frac{1}{\sqrt{L}}\left(-\sum_{i\in\mathrm{A}}e^{i\boldsymbol{q}\cdot\boldsymbol{r}_i}s_{i,l_-}u_{i,l_+}^{*}+\sum_{j\in\mathrm{B}}e^{i\boldsymbol{q}\cdot\boldsymbol{r}_j}v_{j,l_-}t_{j,l_+}^{*}\right),$$
$$c_{-}^{(\frac{1}{2})}(\boldsymbol{q};l_-) = \frac{\sqrt{2S}}{\sqrt{L}}\left(\sum_{i\in\mathrm{A}}e^{i\boldsymbol{q}\cdot\boldsymbol{r}_i}s_{i,l_-}+\sum_{j\in\mathrm{B}}e^{i\boldsymbol{q}\cdot\boldsymbol{r}_j}v_{j,l_-}\right),$$
$$c_{+}^{(\frac{1}{2})}(\boldsymbol{q};l_+) = \frac{\sqrt{2S}}{\sqrt{L}}\left(\sum_{i\in\mathrm{A}}e^{-i\boldsymbol{q}\cdot\boldsymbol{r}_i}u_{i,l_+}+\sum_{j\in\mathrm{B}}e^{-i\boldsymbol{q}\cdot\boldsymbol{r}_j}t_{j,l_+}\right),$$
$$c_{-}^{(-\frac{1}{2})}(\boldsymbol{q};l_-) = -\frac{\sqrt{2S}}{2S\sqrt{L}}\left(\sum_{i\in\mathrm{A}}e^{i\boldsymbol{q}\cdot\boldsymbol{r}_i}\sum_{l'_+}|u_{i,l'_+}|^2 s_{i,l_-}+\sum_{j\in\mathrm{B}}e^{i\boldsymbol{q}\cdot\boldsymbol{r}_j}\sum_{l'_-}|v_{j,l'_-}|^2 v_{j,l_-}\right),$$
$$c_{+}^{(-\frac{1}{2})}(\boldsymbol{q};l_+) = -\frac{\sqrt{2S}}{2S\sqrt{L}}\left(\sum_{i\in\mathrm{A}}e^{-i\boldsymbol{q}\cdot\boldsymbol{r}_i}\sum_{l'_+}|u_{i,l'_+}|^2 u_{i,l_+}+\sum_{j\in\mathrm{B}}e^{-i\boldsymbol{q}\cdot\boldsymbol{r}_j}\sum_{l'_-}|v_{j,l'_-}|^2 t_{j,l_+}\right). \tag{5.3}$$

The static structure factors are available from them,

$$S^{\lambda\lambda'}(\omega) \equiv \frac{1}{L}\sum_{k,k'=1}^{L} e^{i\boldsymbol{q}\cdot(\boldsymbol{r}_k-\boldsymbol{r}_{k'})}\langle \delta S_k^{\lambda}\delta S_{k'}^{\lambda'}\rangle = \int_{-\infty}^{\infty} S^{\lambda\lambda'}(\boldsymbol{q},\omega)\hbar d\omega. \tag{5.4}$$

In spin-wave picture up to $O(S^0)$, the longitudinal dynamic structure factor $S^{zz}(\boldsymbol{q},\omega)$ is described by two-magnon scattering and the transverse dynamic structure factor $S^{\perp}(\boldsymbol{q},\omega) = S^{xx}(\boldsymbol{q},\omega) + S^{yy}(\boldsymbol{q},\omega)$ by one-magnon scattering. We compare the linear-spin-wave (LSW) Hamiltonian $\mathcal{H}_{\rm LSW} \equiv \mathcal{H}^{(2)}+\mathcal{H}^{(1)}$ and interacting-spin-wave (ISW) Hamiltonian $\mathcal{H}_{\rm BL} \equiv \mathcal{H}^{(2)}+\mathcal{H}^{(1)}+\mathcal{H}^{(0)}_{\rm BL}$ calculations of the dynamic structure factor $S(\boldsymbol{q},\omega) \equiv \sum_{\lambda=x,y,z} S^{\lambda\lambda}(\boldsymbol{q},\omega)$ and the static structure factor $S(\boldsymbol{q}) \equiv \sum_{\lambda=x,y,z} S^{\lambda\lambda}(\boldsymbol{q})$.

Figure 5.1(a) shows the static structure factor $S(\boldsymbol{q})$. The intensity of the ten-fold symmetry (five-fold rotational symmetry of the Penrose lattice and $\boldsymbol{q}$ and $-\boldsymbol{q}$ symmetry) static structure factor reflects quasiperiodicity. The coincidence of the peak momenta of $S(\boldsymbol{q})$ with the antiferromagnetic structure factor

$$I(\boldsymbol{q}) = \left|\sum_{k=1}^{L}\sigma_k e^{i\boldsymbol{q}\cdot\boldsymbol{r}_k}\right|^2 ;\ \sigma_k = \begin{cases} +1 & (\boldsymbol{r}_k \in \mathrm{A}) \\ -1 & (\boldsymbol{r}_k \in \mathrm{B}) \end{cases} \tag{5.5}$$

in Fig. 5.1(b) indicates an antiferromagnetic long-range order.

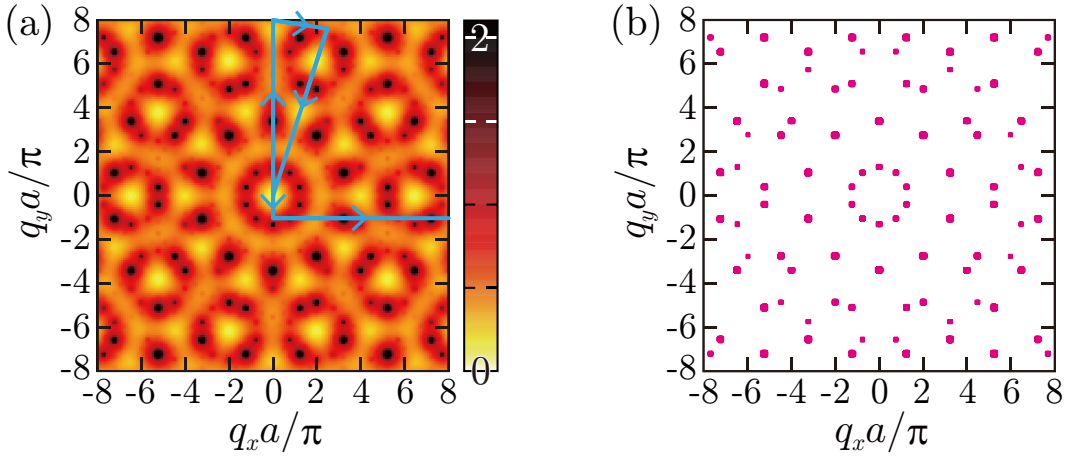

Figure 5.1: (a) Static structure factor $S(\boldsymbol{q})$ for the ISW Hamiltonian $\mathcal{H}_{\rm BL}$. In the LSW Hamiltonian $\mathcal{H}_{\rm LSW}$, the intensity varies but the momentum dependence is the same. Arrowed line represents the momentum space path in Figs. 5.2, 5.4 and 5.5. (b) Antiferromagnetic structure factor $I(\boldsymbol{q})$ with $I(\boldsymbol{q})_{\rm max}/4$ as threshold. Lattice constant $a = \sqrt{2/5}$.

Next, we examine the dynamic structure factor $S(\boldsymbol{q},\omega)$. We first compare the Lanczos exact diagonalization and spin-wave results in a small number site system. From the dynamic structure factor $S(\boldsymbol{q},\omega)$ by the Lanczos exact diagonalization [Fig. 5.2(a)], LSW [Fig. 5.2(b)], and ISW [Fig. 5.2(c)] results of the $L = 16$ site Penrose lattice on the momentum space path shown in Fig. 5.1(a), the momentum dependence is consistent with the exact solution. To examine the energy dependence in detail, the dynamic structure factor at $(q_x/\pi, q_y/\pi) = (3.2, -1.05)$ is shown in Fig. 5.3. Comparing the Lanczos exact solution with the LSW and ISW results in Fig. 5.3(a), the energy dependence of the dynamical structure factor improves

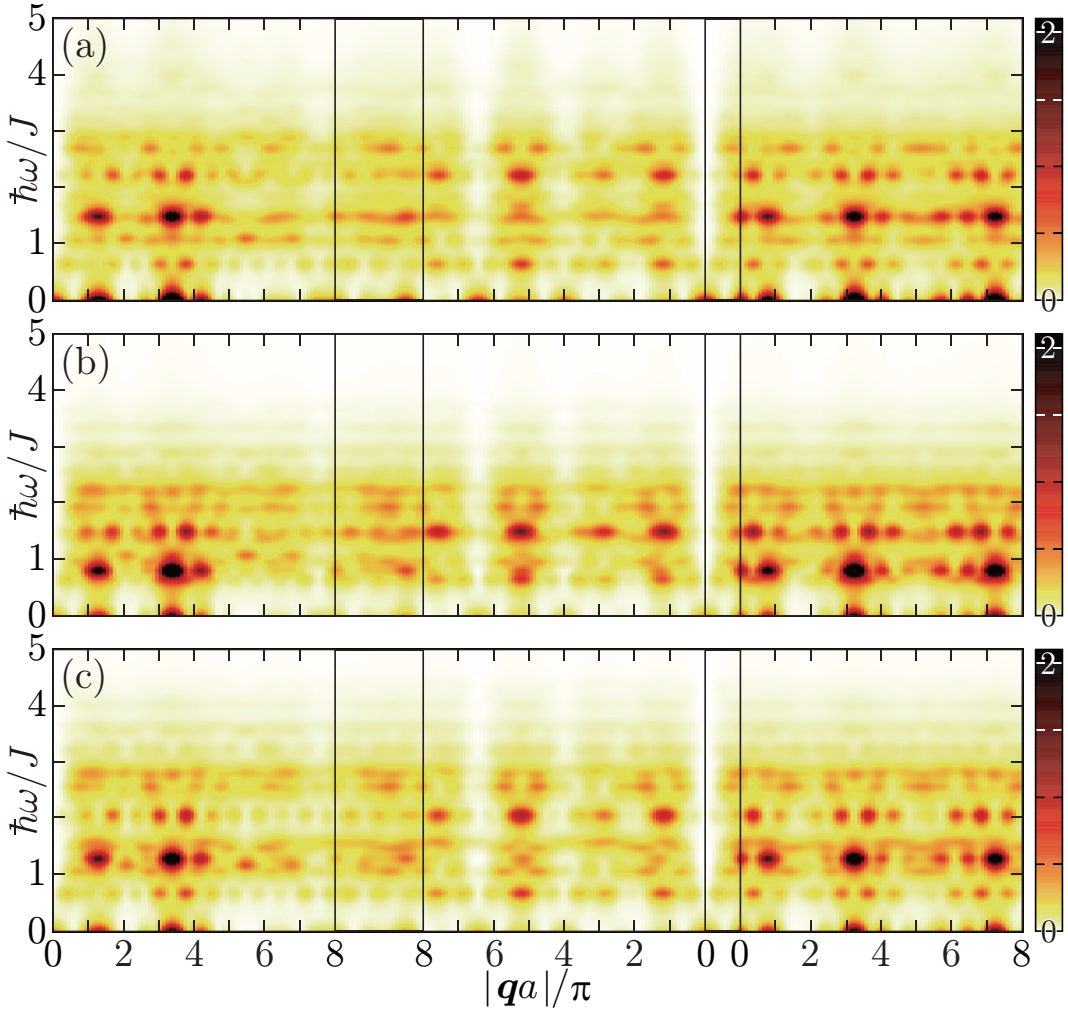

Figure 5.2: Dynamic structure factors $S(\boldsymbol{q},\omega)$ for (a) exact, (b) LSW, and (c) ISW solutions in the momentum space path defined by the Fig.5.1(a) for the $L = 16$ site Penrose lattice. Every spectral intensity is Lorentzian-broadened by a width of $0.1J$.

significantly with ISW result. For the longitudinal dynamical structure factor $S^{zz}(\boldsymbol{q},\omega)$, which is two-magnon scattering, the 2M-CI method (equivalent to the two-magnon GF ladder approximation Bethe-Salpeter equation) can incorporate magnon-magnon interaction effects, but the effects are limited [Fig. 5.3(b)]. In the range up to $O(S^0)$, the transverse dynamical structure factor $S^{\perp}(\boldsymbol{q},\omega)$ is one-magnon scattering as in (5.2), so there is no effect of magnon-magnon interaction.

Dynamic structure factors for LSW result in the $L = 4181$ site Penrose lattice are shown in Fig. 5.4, and those for ISW result are shown in Fig. 5.5. The frequency dependence changes between LSW and ISW results as the energy eigenvalues are corrected. Of the total $S(\boldsymbol{q},\omega)$ [Fig. 5.5(a)], the transverse $S^{\perp}(\boldsymbol{q},\omega)$ [Fig. 5.5(b)], which is one-magnon scattering, gives the main structure, while the longitudinal $S^{zz}(\boldsymbol{q},\omega)$ [Fig. 5.5(c)], which is two-magnon scattering, is blurred. In the low energy region near $\hbar\omega/J = 0$, linear soft modes exist near the magnetic Bragg peak indicated by $S(\boldsymbol{q})$, and exhibit the antiferromagnetic long-range order in the ground state. In contrast, a flat-like band structure exists at high-energy above

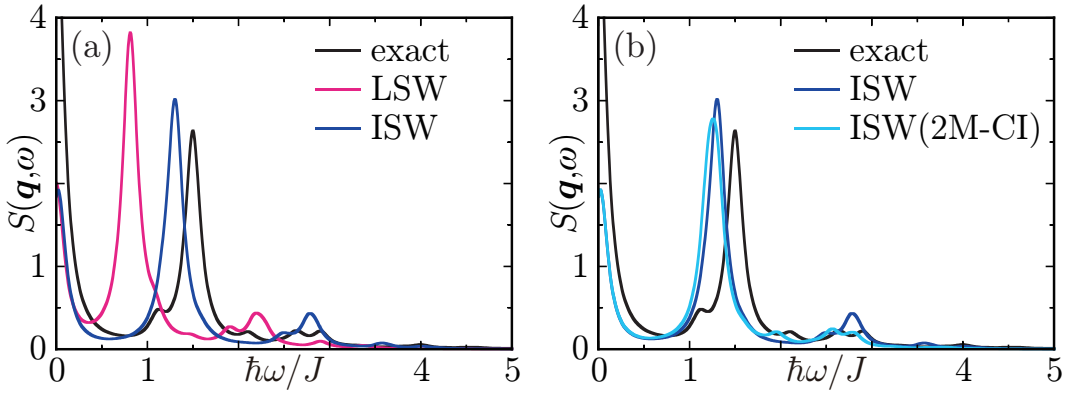

Figure 5.3: Dynamic structure factor $S(\boldsymbol{q},\omega)$ of the $L = 16$ site Penrose lattice at momentum $(q_x/\pi, q_y/\pi) = (3.2, -1.05)$. (a) Comparison of the exact solution with the LSW and ISW results. (b) Comparison of the exact solution with the ISW results from unperturbed and 2M-CI.

$\hbar\omega \gtrsim 3J$, and it exhibits a localized mode. The coexistence of low-energy linear soft modes and high-energy flat band is also know in the Ammann-Beenker lattice [26] and is expected to be a common property of two-dimensional bipartite quasiperiodic antiferromagnets. On the other hand, a very distinct flat band structure appears near $\hbar\omega \simeq 1.5J$ as a feature of the dynamic structure factor of the Penrose lattice antiferromagnet.

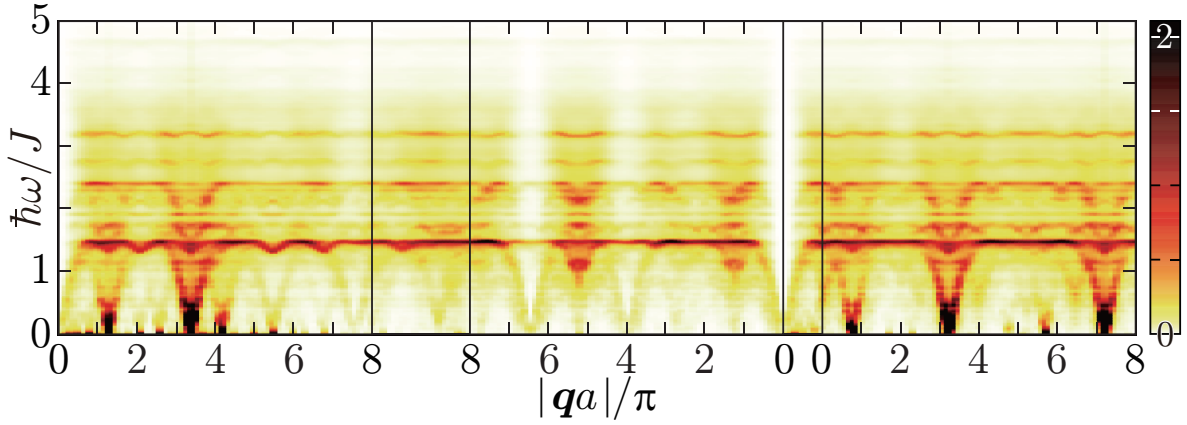

Figure 5.4: Dynamic structure factor $S(\boldsymbol{q},\omega)$ of LSW ($\mathcal{H}_{\rm LSW}$) result in the momentum space path defined in Fig. 5.1(a) for the $L = 4181$ site Penrose lattice. Every spectral intensity is Lorentzian-broadened by a width of $0.01J$.

Figure 5.6 shows the dynamic structure factors for LSW [Fig. 5.6(a)] and ISW [Fig. 5.6(b)] results plotted over the range from $\hbar\omega = 1.0J$ to $\hbar\omega = 2.0J$. Comparing the two results, the flat structure at $\hbar\omega = 1.5J$ in the LSW result splits into two in the ISW result.

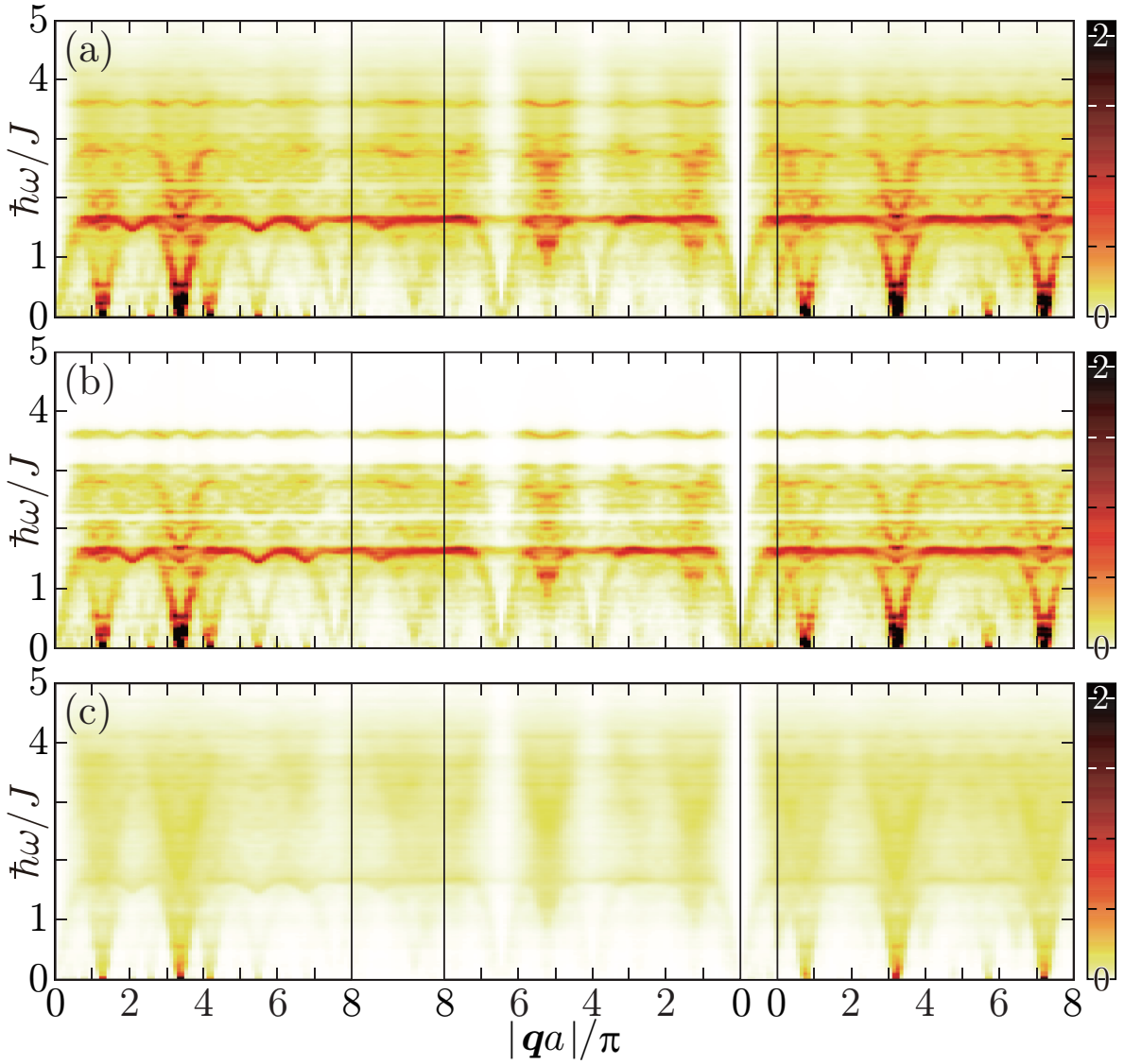

Figure 5.5: Dynamic structure factors for (a) total $[S(\boldsymbol{q},\omega)]$, (b) transverse $[S^{\perp}(\boldsymbol{q},\omega)]$ and (c) longitudinal $[S^{zz}(\boldsymbol{q},\omega)]$ correlations of ISW ($\mathcal{H}_{\mathrm{BL}}$) results in the momentum space path defined in Fig. 5.1(a) for the $L = 4181$ site Penrose lattice. Every spectral intensity is Lorentzian-broadened by a width of $0.01J$.

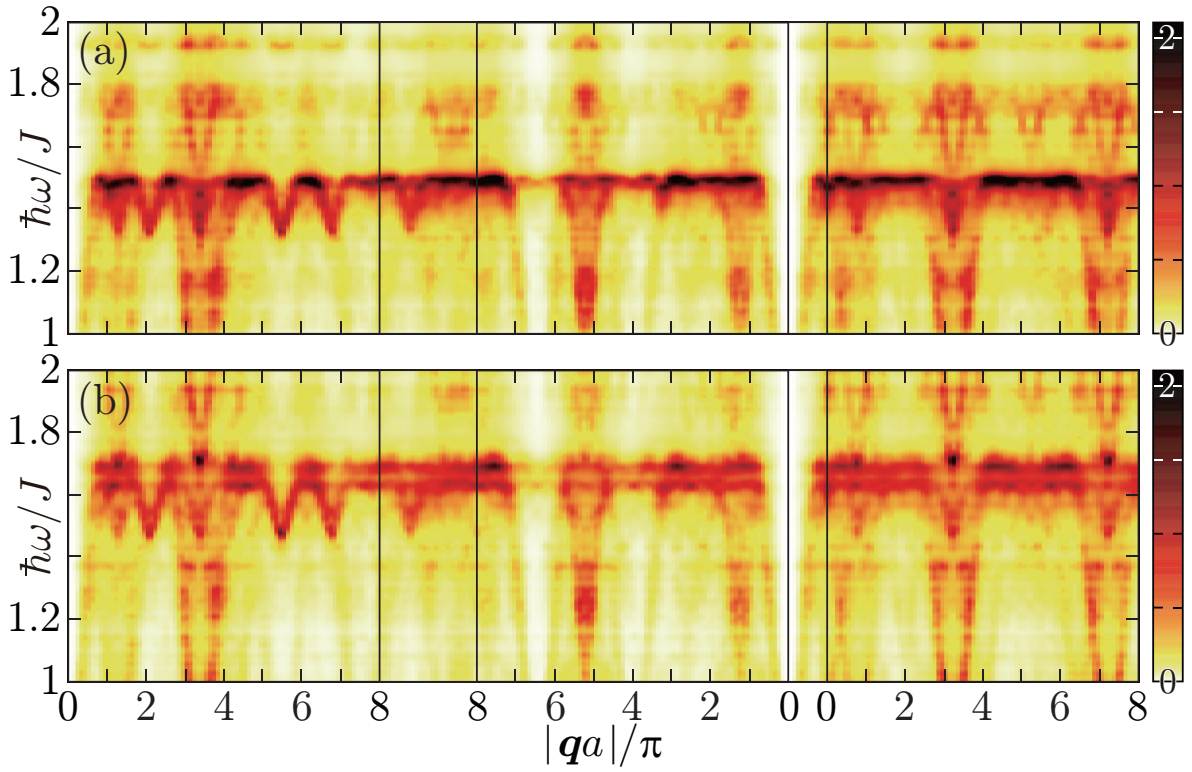

Figure 5.6: Dynamic structure factors $S(\boldsymbol{q}, \omega)$ for (a) LSW ($\mathcal{H}_{\mathrm{LSW}}$) and (b) ISW ($\mathcal{H}_{\mathrm{BL}}$) results of the $L = 4181$ site Penrose lattice plotted as a range from $\hbar\omega = 1.0J$ to $\hbar\omega = 2.0J$.

5.2 Perpendicular Space Mapping

For more detailed $S(\boldsymbol{q},\omega)$ analysis, we introduce a site-resolved dynamic structure factor. We define the site-resolved dynamic structure factor to satisfy $S(\boldsymbol{q},\omega) = \sum_{k=1}^{L} \tilde{S}(k,\boldsymbol{q},\omega) = \sum_{k=1}^{L} \{\tilde{S}^{zz}(k,\boldsymbol{q},\omega) + \tilde{S}^{\perp}(k,\boldsymbol{q},\omega)\}$,

$$\begin{aligned}
\tilde{S}^{zz}(k,\boldsymbol{q},\omega) &= \sum_{l_-,l_+} \mathrm{Re}\left[\tilde{c}^{(0)}_{-+}(k,\boldsymbol{q};l_-,l_+)c^{(0)}_{-+}(\boldsymbol{q};l_-,l_+)^*\right]\delta(\hbar\omega - \varepsilon^-_{l_-} - \varepsilon^+_{l_+}),\\
\tilde{S}^{\perp}(k,\boldsymbol{q},\omega) &= \sum_{\sigma=\pm}\sum_{l_\sigma}\frac{1}{2}\Bigg\{\mathrm{Re}\left[\tilde{c}^{(\frac{1}{2})}_{\sigma}(k,\boldsymbol{q};l_\sigma)c^{(\frac{1}{2})}_{\sigma}(\boldsymbol{q};l_\sigma)^*\right]\\
&\quad + \mathrm{Re}\left[\tilde{c}^{(\frac{1}{2})}_{\sigma}(k,\boldsymbol{q};l_\sigma)c^{(-\frac{1}{2})}_{\sigma}(\boldsymbol{q};l_\sigma)^* + \tilde{c}^{(-\frac{1}{2})}_{\sigma}(k,\boldsymbol{q};l_\sigma)c^{(\frac{1}{2})}_{\sigma}(\boldsymbol{q};l_\sigma)^*\right]\Bigg\}\delta(\hbar\omega - \varepsilon^{\sigma}_{l_\sigma}).
\end{aligned} \tag{5.6}$$

The coefficients read

$$c^{(0)}_{-+}(\boldsymbol{q};l_-,l_+) \equiv \sum_{k=1}^{L}\tilde{c}^{(0)}_{-+}(k,\boldsymbol{q};l_-,l_+), \quad c^{(\pm\frac{1}{2})}_{\sigma}(\boldsymbol{q};l_\sigma) \equiv \sum_{k=1}^{L}\tilde{c}^{(\pm\frac{1}{2})}_{\sigma}(k,\boldsymbol{q};l_\sigma)\ (\sigma=\pm). \tag{5.7}$$

We map the site-resolved dynamic structure factor to the perpendicular space.

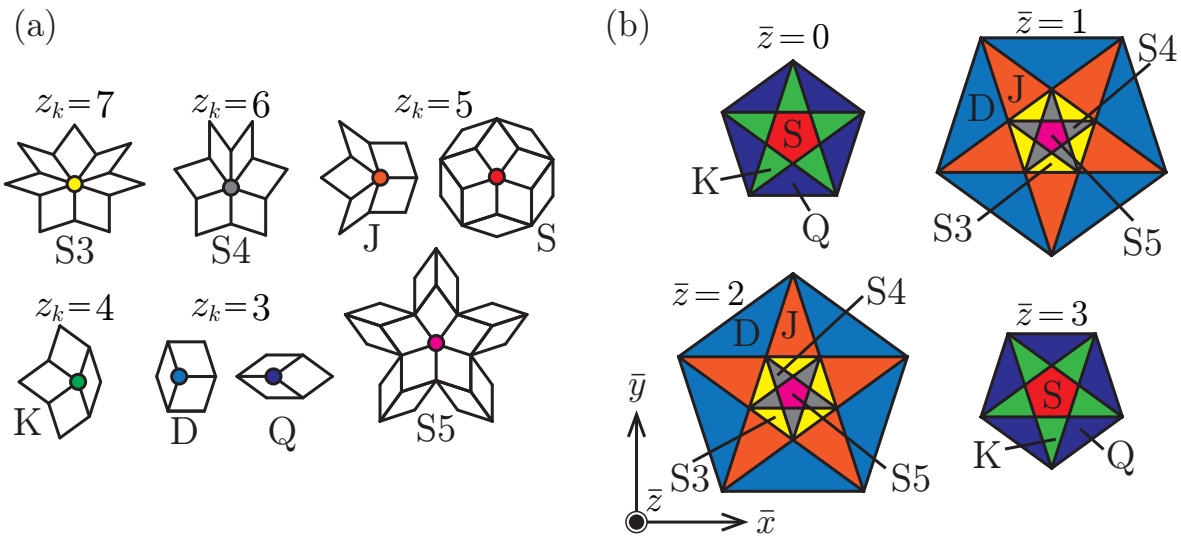

Figure 5.7: (a) Eight local environments of the Penrose lattice with different coordination numbers z_k and geometric structures in the physical space. Notations conform to Refs. [54, 55]. (b) Perpendicular space of the Penrose lattice for $\bar{z} = 0$, 1, 2, and 3. Each colored section corresponds to the eight local environments in (a).

As introduced in Section 1.1, the Penrose lattice is constructed by projecting a five-dimensional hypercubic lattice onto a two-dimensional physical space. Each site of the Penrose lattice is classified by coordination number z_k and local geometry [Fig. 5.7(a)]. The three dimensions left over from the projection are called the perpendicular space, which characterizes the quasiperiodic system. Since one dimension ($\bar{z}$ direction) of the perpendicular space gives the degrees of freedom to form different local isomorphism classes, we consider only four

planes indexed by $\bar{z} = 0, 1, 2$, and 3. The eight local environments of the Penrose lattice are divided into different sections in the perpendicular space [Fig. 5.7(b)]. The sites at $\bar{z} = 0$ and $\bar{z} = 3$ (as well as $\bar{z} = 1$ and $\bar{z} = 2$) correspond to different sublattices from each other.

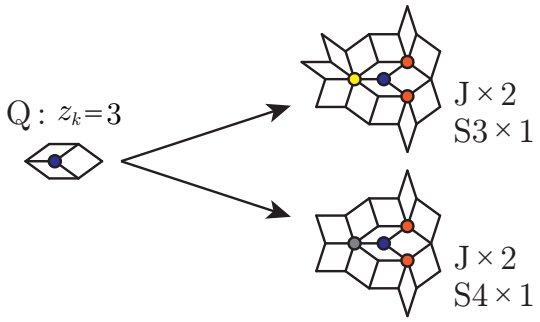

Figure 5.8: Subdivision of Q sites by considering the type of surrounding sites. By setting the site identification distance $R = 1$, the Q sites can be further divided into two types.

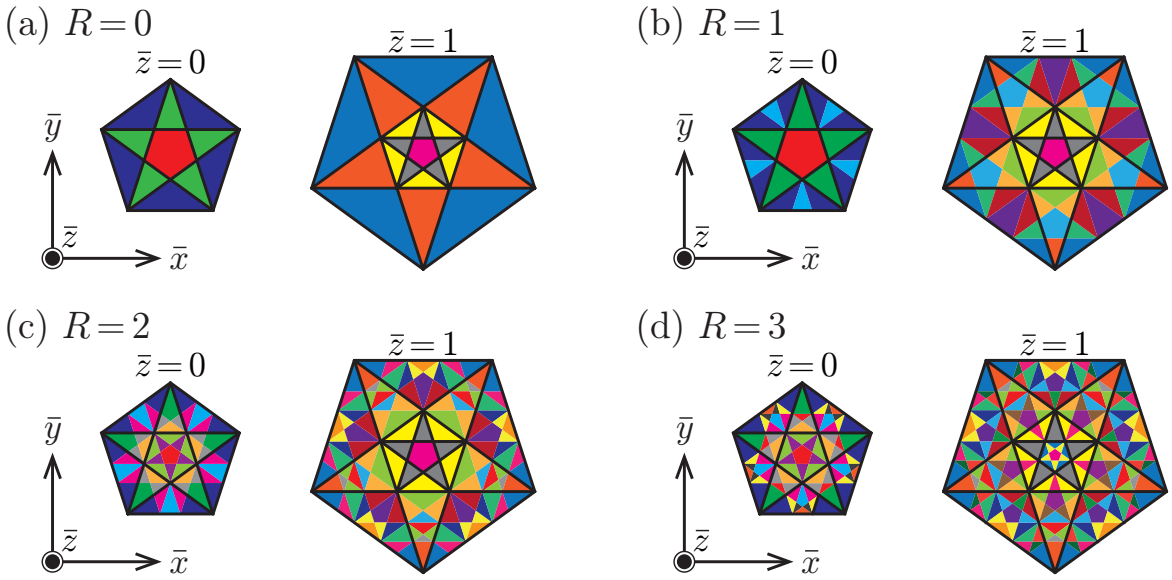

Figure 5.9: Subdivision of the perpendicular space of the Penrose lattice for $\bar{z}_k = 0 and 1$. The site identification distances are (a) $R = 0$, (b) $R = 1$, (c) $R = 2$, and (d) $R = 3$, respectively. Different colors distinguish different sections in the perpendicular space. The numbers of site types are 8 for (a), 15 for (b), 27 for (c), and 40 for (d).

More detailed site identification is performed by considering the local environment of the sites surrounding the focused site [83]. The first step in this classification procedure is to define the distance between sites as the minimum number of links between two given sites. The next step is to find out for each site how many of each type of local environment are present at any distance up to the specified site identification distance R. In this case, we ignore the effects of open boundaries. As an example, for $R = 0$, there are eight classifications as shown in Fig. 5.7(b). Next, for $R = 1$, the Q site (coordination number $z_k = 3$) can be further classified into two types: one with two J sites and one S3 site and one with two J sites and one S4 site (Fig. 5.8). This also subdivides the sections of the perpendicular space more.

We perform detailed site classification at $R = 0$ [Fig. 5.9(a)], $R = 1$ [Fig. 5.9(b)], $R = 2$ [Fig. 5.9(c)], and $R = 3$ [Fig. 5.9(d)], which allows us to subdivide the sites into 8, 15, 27, and 40 types at $R = 0$, $R = 1$, $R = 2$, and $R = 3$, respectively.

With the above in mind, we perform a perpendicular space mapping of site-resolved dynamic structure factors $\tilde{S}(k, \boldsymbol{q}, \omega)$. Figure 5.10 shows the perpendicular space mapping of the site-resolved dynamic structure factor of the LSW Hamiltonian result at $(q_x/\pi, q_y/\pi) = (0.0, 6.0)$ and $\hbar\omega = 1.5J$ for the $L = 11006$ site Penrose lattice. To symmetrize the perpendicular-space mapping, we take the average over the five-fold symmetric momenta. The parameters used in the calculation correspond to the intermediate energy flat band of $S(\boldsymbol{q}, \omega)$, where the intensity is concentrated in the region of the coordination number $z_k = 3$ sites (Q and D sites). The intensity distribution corresponds to the domain subdivision of the perpendicular space with site identification distance $R = 1$ (Fig. 5.10 lower panel). This means that the broadening of the LSW wavefunction at $\hbar\omega = 1.5J$ is estimated to be about $R = 1$.

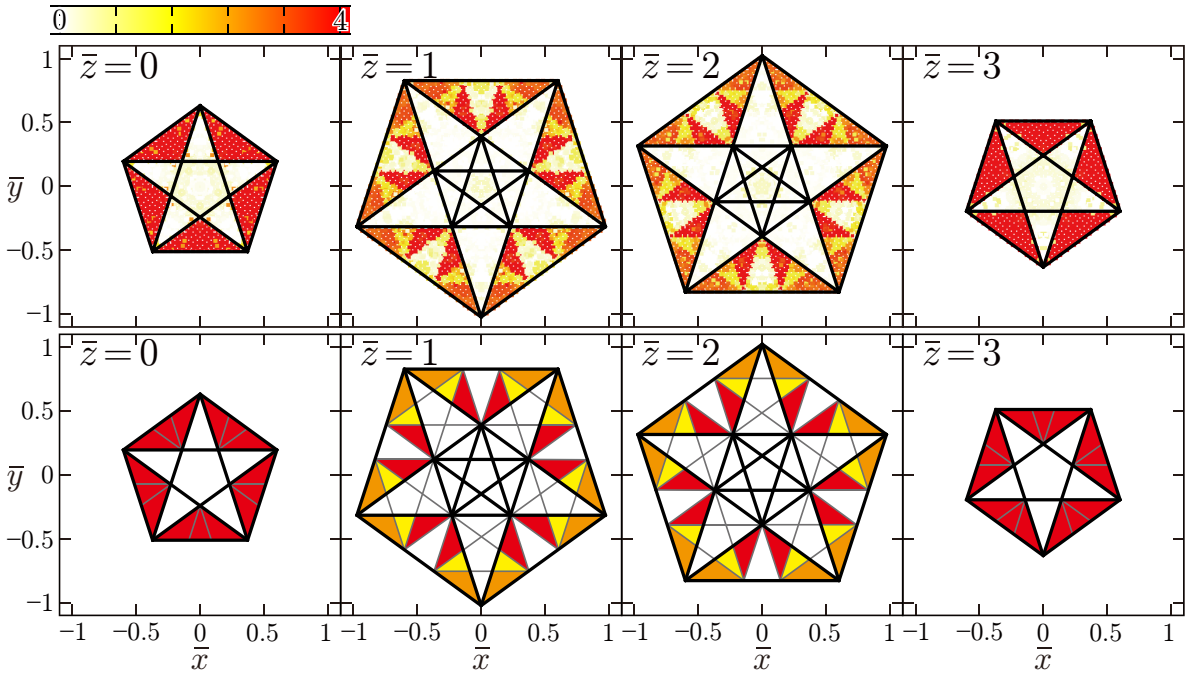

Figure 5.10: Perpendicular-space mapping of the site-resolved dynamic structure factor $L\tilde{S}(k, \boldsymbol{q}, \omega)$ of $L = 11006$ site Penrose lattice for $(q_x a/\pi, q_y a/\pi) = (0.0, 6.0)$ and its five-fold symmetrized momentum at $\hbar\omega = 1.5J$ with the LSW Hamiltonian $\mathcal{H}_{\mathrm{LSW}}$ (upper panels). Section partition of the perpendicular space by discriminations up to site identification distance $R = 1$, painted to correspond to $L\tilde{S}(k, \boldsymbol{q}, \omega)$ (lower panels).

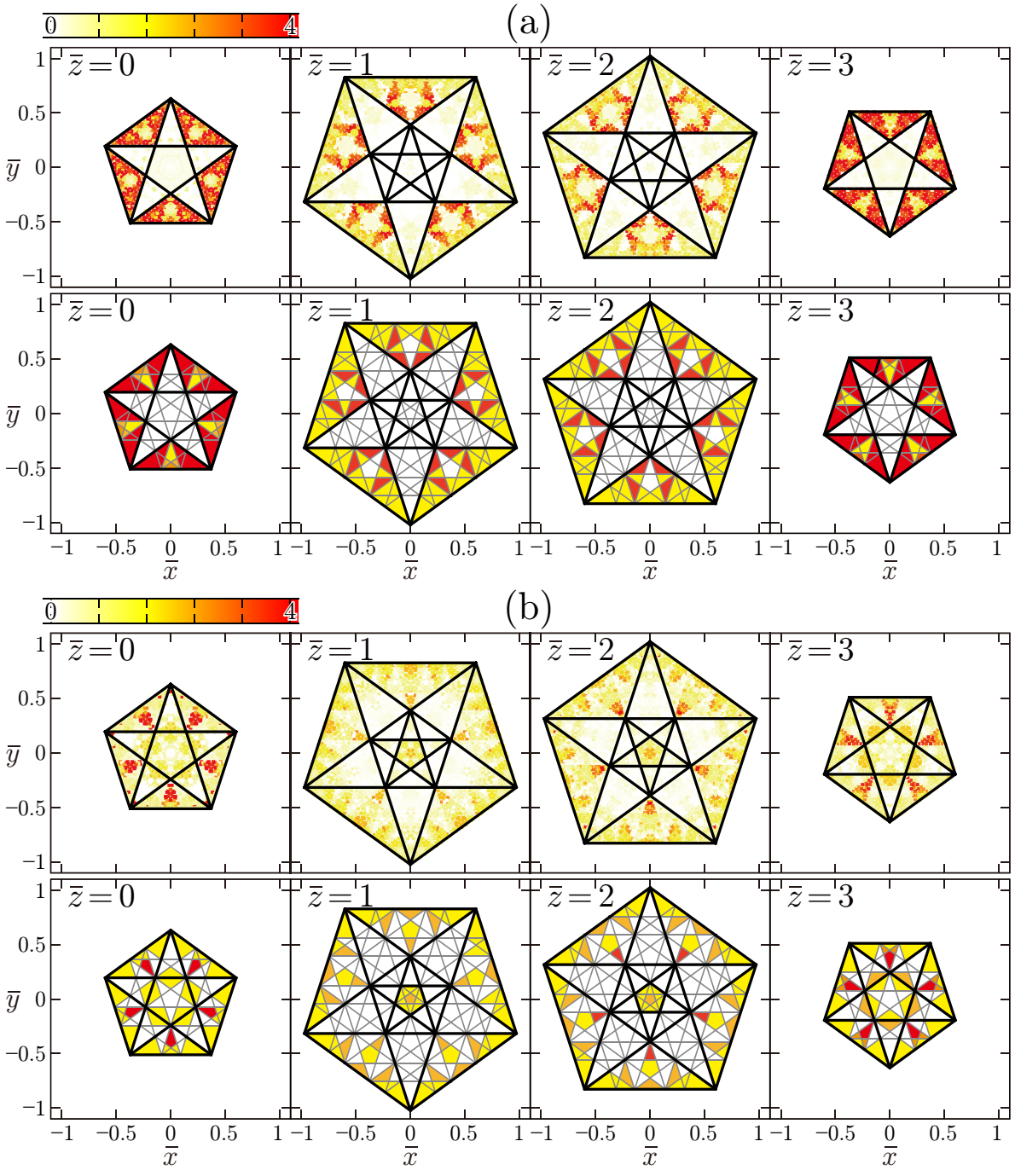

Figure 5.11: The same as Fig. 5.10 for (a) $\hbar\omega = 1.63J$ and (b) $\hbar\omega = 1.7J$ with the ISW Hamiltonian $\mathcal{H}_{\rm BL}$ and site identification distance $R = 3$.

Figure 5.11(a) and 5.11(b) show the perpendicular-space mapping of the site-resolved dynamic structure factor $\tilde{S}(k, \boldsymbol{q}, \omega)$ of the ISW results at $(q_x/\pi, q_y/\pi) = (0.0, 6.0)$ and $\hbar\omega = 1.63J$ and $\hbar\omega = 1.7J$, respectively. In both cases, the intensity is concentrated in the domain with coordination number $z_k = 3$, but the intensity distribution within the domain is different. The intensity distributions correspond to the domain subdivision of the perpendicular space with site identification distance $R = 3$. Therefore, the broadening of the ISW wavefunction in this energy band is estimated to be about $R = 3$. Comparison of Figs. 5.10 and 5.11 shows that the correction from the magnon interaction term $\mathcal{H}_{\mathrm{BL}}^{(0)}$ incorporates the effect of the distant lattice structure and further subdivides the coordination number $z_k = 3$ sites. This causes the intermediate energy flat band structure originating from the $z_k = 3$ site to split. The intensity distributions above and below the split flat structure are complementary to each other, supporting that the corresponding $z_k = 3$ sites are different for each energy.

As an addition, Fig. 5.12(a) shows the perpendicular-space mapping of the site-resolved dynamic structure factor $\tilde{S}(k, \boldsymbol{q}, \omega)$ at $(q_x/\pi, q_y/\pi) = (0.0, 3.4)$ and its five-fold symmetric momentum at $\hbar\omega = 0.1J$. Reflecting the delocalized spin-wave modes at low energies, there is no domain dependence of the perpendicular space, i.e., no local structure dependence of the real space. Fig. 5.12(b) shows the perpendicular space mapping of the site-resolved dynamic structure factor at $(q_x/\pi, q_y/\pi) = (0.0, 3.4)$ and its five-fold symmetric momentum at $\hbar\omega = 3.65J$. The intensity of the site-resolved dynamic structure factor is concentrated in the region corresponding to the S3 site with coordination number $z_k = 7$, consistent with a high-energy localized flat mode.

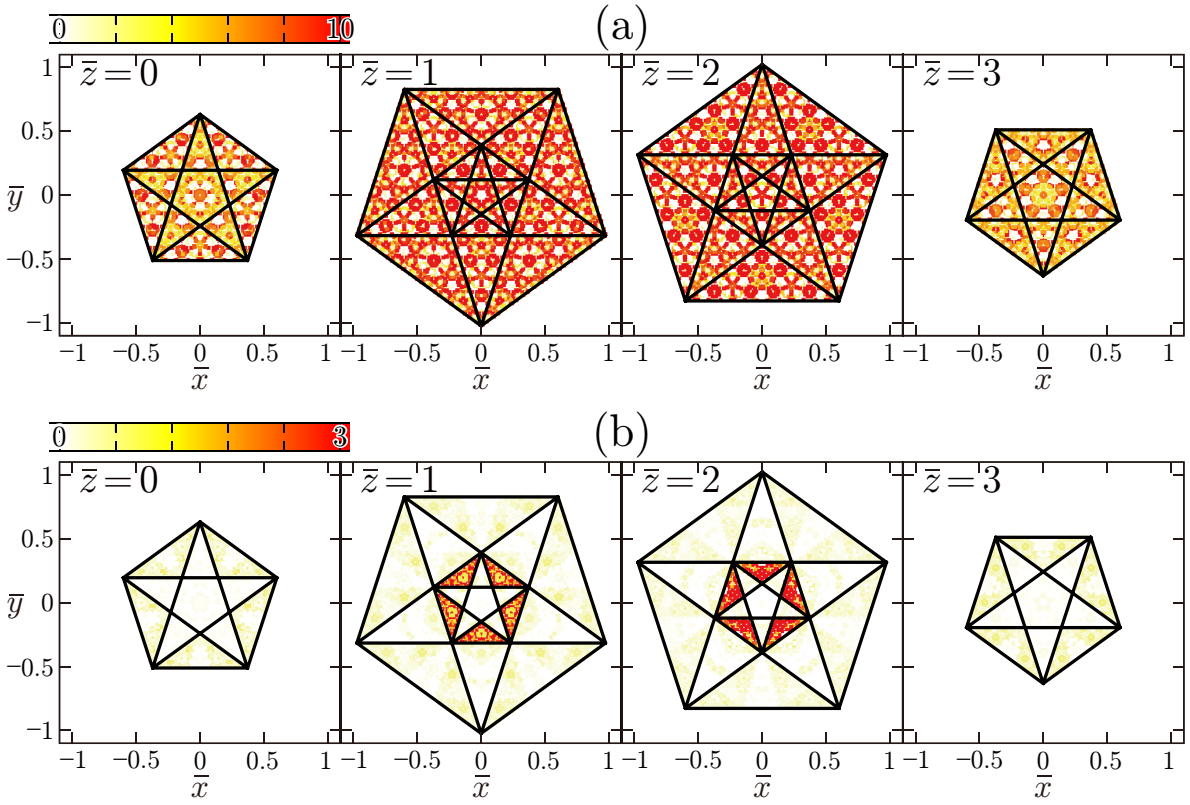

Figure 5.12: The same as Fig. 5.10 for $(q_x/\pi, q_y/\pi) = (0.0, 3.4)$, (a) $\hbar\omega = 0.1J$ and (b)$\hbar\omega = 3.65J$ with the ISW Hamiltonian $\mathcal{H}_{\mathrm{BL}}$.

Chapter 6

Conclusion

We derive the Loudon-Fleury second-order and Shastry-Shraiman fourth-order perturbative magnetic Raman operators in a form applicable to general lattices without any lattice geometry assumption. Using the derived effective Raman operators, we calculate the Raman responses of Heisenberg antiferromagnets on the $\mathbf{C}_{5\mathrm{v}}$ Penrose and $\mathbf{C}_{8\mathrm{v}}$ Ammann-Beenker lattices.

Within the Loudon-Fleury mechanism, we find one and only Raman-active mode of E_2 symmetry without any dependence on linearly incident and scattered photon polarizations. This depolarization occurs because the two polarization-vector basis functions $e^x_{\mathrm{in}}e^{y\,*}_{\mathrm{sc}} + e^y_{\mathrm{in}}e^{x\,*}_{\mathrm{sc}}$ and $e^x_{\mathrm{in}}e^{x\,*}_{\mathrm{sc}} - e^y_{\mathrm{in}}e^{y\,*}_{\mathrm{sc}}$ span such a two-dimensional irreducible representation as to be one and only Raman-active symmetry species. The group theory analysis reveals that this criterion is met by not only for the $\mathbf{C}_{5\mathrm{v}}$ Penrose and $\mathbf{C}_{8\mathrm{v}}$ Ammann-Beenker lattices but also for all two-dimensional quasiperiodic lattices with noncrystallographic rotational symmetry.

Beyond the Loudon-Fleury mechanism, two more symmetry species A_1 and A_2 are activated via dynamic ring-exchange and chiral spin fluctuations. The polarization dependence of each symmetry mode is clarified explicitly with the help of group theory, and the spectrum of each symmetry species can be extracted by considering circularly and linearly polarization together.

In the Shastry-Shraiman fourth-order perturbation Raman response, the contributions of multi-magnon scattering are significant in the high frequency region $\hbar\omega \gtrsim 5J$. To evaluate this, we employ the GF perturbation approach on one hand and the CI variational magnon wave function on the other hand to calculate the mulitimagnon contributions to the inelastic light scatterings. Since the perturbative renormalization of the more-than-three-magnon GFs are hardly tractable in the traditional GF approach, we need to decompose the four-magnon GFs. However, the decomposition is not unique. We decompose the four-magnon GFs into the product of two two-magnon GFs or three- and one-magnon GFs, but the GF results are less reliable due to artificial differences caused by the decomposition. In contrast, we propose an alternative approach utilizing the CI variational wavefunction, which allows us to calculate four-magnon scattering without any decomposition. We further find that there is a contribution to the four-magnon scattering that is missed by the indirect four-magnon scattering evaluation using the conventional GF approach, by comparing the CI calculation with the exact solution obtained by the Lanczos method.

Under such circumstances, our elaborate CI approach can open up a new path of calculating dynamic properties. The CI calculation can be systematically extended to higher-order magnon scatterings.

We have also performed static and dynamic structure factor calculations for antiferromag-

netic Heisenberg models on the $\mathbf{C}_{5\mathrm{v}}$ Penrose lattice. Comparison of the static and antiferromagnetic structure factors suggests the presence of antiferromagnetic long-range order. The dynamic structure factor has linear soft modes near the magnetic Bragg peak at low frequencies and flat localized modes at high frequencies. In the Penrose lattice antiferromagnetic Heisenberg model, there is a distinct flat band structure even at intermediate energies. By introducing a site-resolved dynamic structure factor and performing the analysis in perpendicular space, the intermediate energy flat band structure is shown to be a localized mode with a coordination number of $z_k = 3$ sites. The flat band structure splits by incorporating the effect of the $O(S^0)$ magnon interaction in the spin-wave Hamiltonian.

By extending the correspondence between the domain partitioning of the perpendicular space and the local structure of the real space, the coordination number $z_k = 3$ sites can be classified more finely. The flat band splitting is attributed to the magnon interaction effect that creates a distinction at the $z_k = 3$ site. We estimate the localization length of the wavefunction from the intensity distribution of the site-resolved dynamic structure factor in the perpendicular space and the site identification distance R required to partition the perpendicular space into subdomains. The localized length of the wavefunction is extended due to the effect of the $O(S^0)$ magnon interaction.

Acknowledgement

I would like to express my sincere gratitude to Professor Shoji Yamamoto for his numerous ideas, critical discussions, helpful suggestions, and enthusiastic guidance in writing the paper. I would like to sincerely acknowledge Dr. Jun Ohara for his discussion of the details of the calculations and his precise comments on the coding. I would like to acknowledge Professor Koji Nemoto and Professor Atsushi Kawamoto for their helpful comments during the review process of this paper. I would also like to thank the members of the Mathematical Physics Laboratory for various discussions. Finally, I would like to express my deepest gratitude to my family for their support during my doctoral days.

Bibliography

[1] D. Schehtman, I. Blech, D. Gratias, and J. W. Cahn, Phys. Rev. Lett. **53**, 1951 (1984).

[2] D. Levine and P. J. Steinhardt, Phys. Rev. Lett. **53**, 2477 (1984).

[3] D. Levine and P. J. Steinhardt, Phys. Rev. B **34**, 596 (1986).

[4] S. Van Smaalen, Cryst. Rev. **4**, 79 (1995).

[5] M. Kohmoto and B. Sutherland, Phys. Rev. Lett. **56**, 2740 (1986).

[6] M. Arai, T. Tokihiro, T. Fujiwara, and M. Kohmoto, Phys. Rev. B **38**, 1621 (1988).

[7] N. Macé, A. Jagannathan, P. Kalugin, R. Mosseri, and F. Piéchon, Phys. Rev. B **96**, 045138 (2017).

[8] K. Deguchi, S. Matsukawa, N. K. Sato, T. Hattori, K. Ishida, H. Takakura, and T. Ishimasa, Nat. Mater. **11**, 1013 (2012).

[9] K. Kamiya, T. Takeuchi, N. Kabeya, N. Wada, T. Ishimasa, A. Ochiai, K. Deguchi, K. Imura, and N. K. Sato, Nat. Commun. **9**, 154 (2018).

[10] S. Sakai, N. Takemori, A. Koga, and R. Arita, Phys. Rev. B **95**, 024509 (2017).

[11] R. N. Araújo and E. C. Andrade, Phys. Rev. B **100**, 014510 (2019).

[12] S. Sakai and R. Arita, Phys. Rev. Res. **1**, 022002(R) (2019).

[13] B. Charrier and D. Schmitt, J. Magn. Magn. Mater. **171**, 106 (1997).

[14] I. R. Fisher, K. O. Cheon, A. F. Panchula, P. C. Canfield, M. Chernikov, H. R. Ott, and K. Dennis, Phys. Rev. B **59**, 308 (1999).

[15] T. J. Sato, H. Takakura, A. P. Tsai, K. Shibata, K. Ohoyama, and K. H. Andersen, Phys. Rev. B **61**, 476 (2000).

[16] T. J. Sato, H. Takakura, A. P. Tsai, and K. Shibata, Phys. Rev. B **73**, 054417 (2006).

[17] T. J. Sato, S. Kashimoto, C. Masuda, T. Onimaru, I. Nakanowatari, K. Iida, R. Morinaga, and T. Ishimasa, Phys. Rev. B **77**, 014437 (2008).

[18] R. Tamura, Y. Muro, T. Hiroto, K. Nishimoto, and T. Takabatake, Phys. Rev. B **82**, 220201(R) (2010).

[19] S. Yoshida, S. Suzuki, T. Yamada, T. Fujii, A. Ishikawa, and R. Tamura, Phys. Rev. B **100**, 180409(R) (2019).

[20] Y. Okabe and K. Niizeki, J. Phys. Soc. Jpn. **57**, 16 (1988).

[21] Y. Komura and Y. Okabe, J. Phys. Soc. Jpn. **85**, 044004 (2016).

[22] E. Y. Vedmedenko, H. P. Oepen, and J. Kirschner, Phys. Rev. Lett. **90**, 137203 (2003).

[23] E. Y. Vedmedenko, U. Grimm, and R. Wiesendanger, Phys. Rev. Lett. **93**, 076407 (2004).

[24] A. Koga and H. Tsunetsugu, Phys. Rev. B **96**, 214402 (2017).

[25] A. Koga, Phys. Rev. B **102**, 115125 (2020).

[26] S. Wessel and I. Milat, Phys. Rev. B **71**, 104427 (2005).

[27] A. Szallas and A. Jagannathan, Phys. Rev. B **77**, 104427 (2008).

[28] S. Wessel, A. Jagannathan, and S. Haas, Phys. Rev. Lett. **90**, 177205 (2003).

[29] A. Jagannathan, A. Szallas, S. Wessel, and M. Duneau, Phys. Rev. B **75**, 212407 (2007).

[30] P. A. Fleury and R. Loudon, Phys. Rev. **166**, 514 (1968).

[31] R. W. Davis, S. R. Chinn, and H. J. Zeiger, Phys. Rev. B **4**, 992 (1971).

[32] T. Suzuki and Y. Natsume, J. Phys. Soc. Jpn. **61**, 998 (1992).

[33] P. E. Sulewski, P. A. Fleury, K. B. Lyons, and S-W. Cheong, Phys. Rev. Lett. **67**, 3864 (1991).

[34] C. M. Canali and S. M. Girvin, Phys. Rev. B **45**, 7127 (1992).

[35] A. V. Chubukov and D. M. Frenkel, Phys. Rev. B **52**, 9760 (1995).

[36] A. W. Sandvik, S. Capponi, D. Poilblanc, and E. Dagotto, Phys. Rev. B **57**, 8478 (1998).

[37] N. Perkins and W. Brenig, Phys. Rev. B **77**, 174412 (2008).

[38] O. Cépas, J. O. Haerter, and C. Lhuillier, Phys. Rev. B **77**, 172406 (2008).

[39] B. S. Shastry and B. I. Shraiman, Phys. Rev. Lett. **65**, 1068 (1990).

[40] B. S. Shastry and B. I. Shraiman, Int. J. Mod. Phys. B **5**, 365 (1991).

[41] W.-H. Ko, Z.-X. Liu, T.-K. Ng, and P. A. Lee, Phys. Rev. B **81**, 024414 (2010).

[42] F. Michaud, F. Vernay, and F. Mila, Phys. Rev. B **84**, 184424 (2011).

[43] T. Inoue and S. Yamamoto, Phys. Status Solidi B **257**, 2000118 (2020).

[44] L. Guidoni, C. Triché, P. Verkerk, and G. Grynberg, Phys. Rev. Lett. **79**, 3363 (1997).

[45] K. Viebahn, M. Sbroscia, E. Carter, J.-C. Yu, and U. Schneider, Phys. Rev. Lett. **122**, 110404 (2019).

[46] M. Sbroscia, K. Viebahn, E. Carter, J.-C. Yu, A. Gaunt, and U. Schneider, Phys. Rev. Lett. **125**, 200604 (2020).

[47] L. Sanchez-Palencia and L. Santos, Phys. Rev. A **72**, 053607 (2005).

[48] A. Jagannathan and M. Duneau, Europhys. Lett. **104**, 66003 (2013).

[49] A. Jagannathan and M. Duneau, Eur. Phys. J. B **87**, 149 (2014).

[50] L.-M. Duan, E. Demler, and M. D. Lukin, Phys. Rev. Lett. **91**, 090402 (2003).

[51] D. Johnstone, P. Öhberg, and C. W. Duncan, Phys. Rev. A **100**, 053609 (2019).

[52] R. Lifshitz, Z. Kristallogr. **222**, 313 (2007).

[53] M. Duneau and A. Katz, Phys. Rev. Lett. **54**, 2688 (1985).

[54] N. G. de Bruijn, Indag. Math. Proc. Ser. A **84**, 39 (1981).

[55] N. G. de Bruijn, Indag. Math. Proc. Ser. A **84**, 53 (1981).

[56] J. E. S. Socolar, Phys. Rev. B **39**, 10519 (1989).

[57] M. Baake and D. Joseph, Phys. Rev. B **42**, 8091 (1990).

[58] T. Holstein and H. Primakoff, Phys. Rev. **58**, 1098 (1940).

[59] Y. Noriki and S. Yamamoto, J. Phys. Soc. Jpn. **86**, 034714 (2017).

[60] S. Yamamoto and Y. Noriki, Phys. Rev. B **99**, 094412 (2019).

[61] R. M. White, M. Sparks, and I. Ortenburger, Phys. Rev. **139**, A450 (1965).

[62] S. Yamamoto, T. Fukui, K. Maisinger, and U. Schollwöck, J. Phys.: Condens. Matter **10**, 11033 (1998).

[63] S. Yamamoto, Phys. Rev. B **69**, 064426 (2004).

[64] F. Lema, J. Eroles, C. D. Batista, and E. R. Gagliano, Phys. Rev. B **55**, 15295 (1997).

[65] J. Eroles, C. D. Batista, S. B. Bacci, and E. R. Gagliano, Phys. Rev. B **59**, 1468 (1999).

[66] F. Nori, R. Merlin, S. Haas, A. W. Sandvik, and E. Dagotto, Phys. Rev. Lett. **75**, 553 (1995).

[67] S. Yamamoto, J. Phys. Soc. Jpn. **81**, 063705 (2012).

[68] V. S. Viswanath and G. Müller, *The Recursion Method* (Springer, Berlin, 1994).

[69] S. Yamamoto, Physica B **481**, 224 (2016).

[70] B. Perreault, J. Knolle, N. B. Perkins, and F. J. Burnell, Phys. Rev. B **92**, 094439 (2015).

[71] T. Kimura and S. Yamamoto, Phys. Rev. B **101**, 214411 (2020).

[72] S. Yamamoto and T. Kimura, J. Phys. Soc. Jpn. **89**, 063701 (2020).

[73] T. P. Devereaux and R. Hackl, Rev. Mod. Phys. **79**, 175 (2007).

[74] A. Carbone, A. Cipollone, C. Barbieri, A. Rios, and A. Polls, Phys. Rev. C **88**, 054326 (2013).

[75] A. L. Fetter and J. D. Walecka, *Quantum Theory of Many-Particle Systems* (McGraw-Hill, New York, 1971).

[76] C. Barbieri and W. H. Dickhoff, Phys. Rev. C **63**, 034313 (2001).

[77] C. Barbieri, D. Van Neck, W. H. Dickhoff, Phys. Rev. A **76**, 052503 (2007).

[78] J. Ohara and S. Yamamoto, J. Phys. Soc. Jpn. **74**, 250 (2005).

[79] J. Ohara and S. Yamamoto, Phys. Rev. B **73**, 045122 (2006).

[80] S. Yamamoto, Phys. Rev. B **78**, 235205 (2008).

[81] J. Knolle, G.-W. Chern, D. L. Kovrizhin, R. Moessner, and N. B. Perkins, Phys. Rev. Lett. **113**, 187201 (2014).

[82] R. H. Lehmberg, M. F. Wolford, J. L. Weaver, D. Kehne, S. P. Obenschain, D. Eimerl, and J. P. Palastro, Phys. Rev. A **102**, 063530 (2020).

[83] R. Ghadimi, T. Sugimoto, T. Tohyama, Phys. Rev. B **102**, 224201 (2020).